2009

Effects of mechanical and metallurgical variables on creep, fracture toughness and crack growth behavior of Alloy 617

Muhammad Hasibul Hasan
University of Nevada Las Vegas

EFFECTS OF MECHANICAL AND METALLURGICAL VARIABLES ON CREEP, FRACTURE TOUGHNESS AND CRACK GROWTH BEHAVIOR OF ALLOY 617

by

Muhammad Hasibul Hasan

Bachelor of Science in Mechanical Engineering
Bangladesh University of Engineering & Technology, Dhaka
June 2000

Master of Science in Mechanical Engineering
Wayne State University, Detroit
December 2002

A dissertation submitted in partial fulfillment
of the requirements for the

Doctor of Philosophy Degree in Mechanical Engineering
Department of Mechanical Engineering
Howard R. Hughes College of Engineering

Graduate College
University of Nevada, Las Vegas
December 2009

UNIVERSITY OF NEVADA LAS VEGAS

THE GRADUATE COLLEGE

We recommend that the dissertation prepared under our supervision by

Muhammad Hasibul Hasan

entitled

Effects of Mechanical and Metallurgical Variables on Creep, Fracture Toughness and Crack Growth Behavior of Alloy 617

be accepted in partial fulfillment of the requirements for the degree of

Doctor of Philosophy
Mechanical Engineering

Brendan O'Toole, Committee Chair

Ajit K. Roy, Committee Co-Chair

Woosoon Yim, Committee Member

Anthony E. Hechanova, Committee Member

Daniel Cook, Committee Member

Edward S. Neumann, Graduate Faculty Representative

Ronald Smith, Ph. D., Vice President for Research and Graduate Studies
and Dean of the Graduate College

December 2009

ABSTRACT

Effects of Mechanical and Metallurgical Variables on Creep, Fracture Toughness and Crack Growth Behavior of Alloy 617

by

Muhammad Hasibul Hasan

Dr. Brendan O'Toole, Examination Committee Chair
Associate Professor of Mechanical Engineering
University of Nevada, Las Vegas

Dr. Ajit K. Roy, Examination Committee Co-Chair
Professor of Mechanical Engineering
University of Nevada, Las Vegas

Nickel base Alloy 617 has been identified to be a suitable structural material for heat exchanger applications in both hydrogen and electricity generation using nuclear heat. A maximum operating temperature of 950ºC has been specified by department of energy (DOE) for both applications to achieve a maximum possible efficiency. Therefore, an extensive investigation has been pursued to evaluate time-dependent-deformation (Creep) of this alloy as functions of temperature and applied load. The results indicate that this alloy exhibited severe creep deformation, characterized by development of an instantaneous tertiary creep region at 850 and 950ºC under applied stresses corresponding to its 35% yield strength (YS) values at these temperatures. However, this alloy satisfied the deformation acceptance criteria at 5, 10, 25 and 35 percent of its YS values when loaded at 750ºC. The results of crack growth studies indicate that this alloy showed an enhanced cracking susceptibility when tested within a temperature range of 100 to 200ºC at the lowest loading ratio of 0.1. The fracture toughness of this alloy in terms of J_{IC} was not significantly influenced by variation in temperature. The results of stress-corrosion-cracking study suggest that the rate of crack

growth was gradually reduced with longer testing duration due to a relaxation of load with time. Microscopic evaluations of tested specimens were performed using numerous conventional techniques.

TABLE OF CONTENTS

LIST OF TABLES

LIST OF FIGURES

ACKNOWLEDGMENTS

First and foremost, I am thankful to Almighty Allah for allowing me writing my dissertation acknowledgement. Words fail to express my profound regards from the inmost recess of my heart to my advisors Dr. Ajit K. Roy and Dr. Brendan O'Toole for the invaluable help, constant guidance and wide counseling extended by them right from the selection of topic to the successful completion of my research work.

I would like to extend my sincere thanks and appreciation to the other members of dissertation committee: Drs. Anthony E. Hechanova, Woosoon Yim, Daniel P. Cook and Edward S Neumann for their constrictive suggestions that assisted me to finalize my dissertation contents. I would like to thank to my colleagues at Material Performance Laboratory for their consistent help and encouragement. Special thanks to Joydeep Pal, who helped me in experimental setups throughout the course of my doctoral research.

Many people on the faculty and staff of the college of engineering and Harry Reid Center assisted and encouraged me in various ways during my course of studies. I am especially grateful to Dr. Thomas Hartmann who is the master in XRD analysis, Dr. Longzhou Ma – seems like he can enter into the nano structure of any material with the help of his TEM tool, Kevin for machining several of my samples. I was also greatly inspired pedagogically by Dr. Tom Tan, for whom I was a Research Assistant for my first semester at UNLV and I thank the students whom I was privileged to teach and from whom I also learned a lot.

The most important people are and have to be my lovely parents. Since the dawn of my boyhood, I remember my parents passed me the message "We will not be able to give

you everything for your education, but we will give everything whatever we have". I am blessed with their parenting skills and bear in mind their innumerable sacrifices.

Natasha: my gorgeous wife; she has been my enduring source of strength and because of her my social life has been so attractive and meaningful. Ayaz: our Eid Boy; the center of our all attentions - helped me by tearing off my research papers and sketching A B C 's on my draft dissertation!

Some thank you's to non work related people: grand-ma Jobaida khatun, mother-in - law Amina Akhter, my beautiful sister Dr. Hasina Habib, my visionary brother Hafizul Hasan, Beacon, Shahid bhai and Enam bhai, in general, you are all great!!! The fabulous city of Las Vegas herself left a huge impression during my course of study and will peep in my mind for many days to come.

I would like to express my gratitude and thanks to the United States Department of Energy for the financial support under grant # DE-FC07-04ID14566.

Of course, despite all the assistance provided by Prof. Roy and others, I alone remain responsible for the content of the following, including any errors or omissions which may unwittingly remain.

CHAPTER 1

INTRODUCTION

The cost of energy, in particular, conventional fossil fuels, such as oil and gas, has been increasing rapidly during this past decade. Among all other reasons, the increased cost is primarily due to the imbalance in supply and demand. Further, the extensive use of fossil fuels has been receiving negative publicity in industrialized nations all over the world due to the generation of excessive pollutant. The evidence of human-caused climatic change is overwhelming. Scientists from all around the globe have recently come to a conclusion that the use of hydrocarbons contained in oil and gas can pollute the atmosphere with thick ozone layers due to the greenhouse effect resulting from the emission of carbon dioxide (CO_2). Increase in greenhouse gases has now been blamed for global warming that may eventually cause numerous natural disasters.

A combination of escalating cost and environmental concern associated with the fossil fuel usage has, therefore, prompted many nations to develop alternate sources of energy. To circumvent these underlying problems, the United States Department of Energy (USDOE) has been exploring many alternate cost-effective and environment-friendly sources of fuel [1, 2]. One such fuel is hydrogen, which is known to be generated by many different techniques [3]. While Hydrogen generation by electrolysis [4, 5] of water has been adopted by many nations including USDOE, the energy needed to produce hydrogen by this technique does not provide any economic incentive due to the added cost of power needed to electrolyze water and thus, can lead to reduced efficiency. Besides economic incentives, environmental issues and domestic supply are also some other concerns. Therefore, during these past several years, USDOE has been

concentrating on a novel approach of hydrogen generation using heat from the nation's nuclear power plants that would involve chemical reactions at elevated temperatures. Hydrogen generation using nuclear heat and chemical reactions can be accomplished by two major thermochemical processes. They are sulfur-iodine (S-I) [6, 7] and calcium-bromine (Ca-Br) [8] cycles, respectively. However, the S-I process has been selected by NHI to the Ca-Br cycle due to a relatively higher efficiency in hydrogen generation.

The S-I cycle was invented by the General Atomics Corporation (GA) in the mid 1970's [9] The net reaction in this process is the decomposition of water into hydrogen and oxygen. A complete laboratory scale S-I test loop has been operated successfully in Japan [10]. The necessary heat for the thermochemical reactions in the S-I process has been proposed to be provided by a nuclear reactor, transmitted through an intermediate heat exchanger (IHE) into the hydrogen generation plant consisting of different reaction chambers, as illustrated in Figure 1-1.

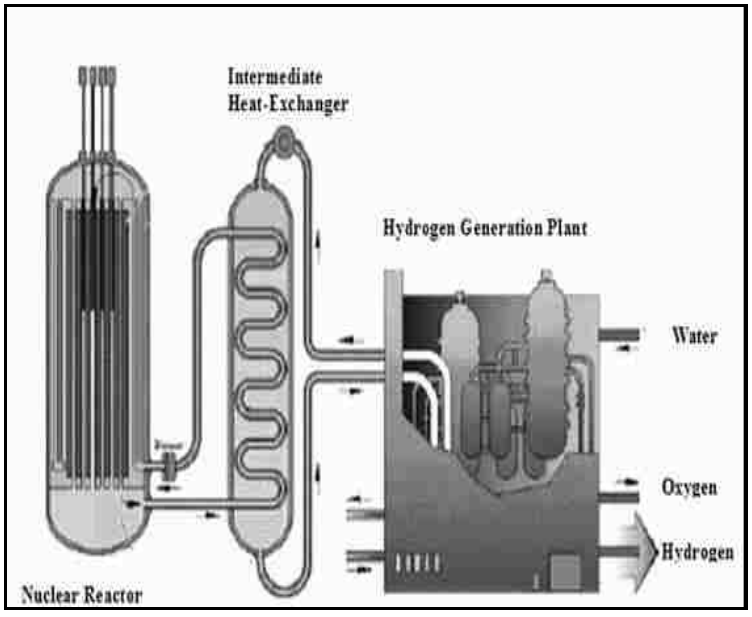

Figure 1-1 Nuclear Hydrogen Generation Concept

Conceptually, the generation of hydrogen by the S-I process consists of a series of chemical reactions involving different species at elevated temperatures. These reactions would occur within closed loops, where water could be fed to the process, oxygen and hydrogen gas could be collected, and all other reactants would be recycled, as illustrated in Figure 1-2. The first step to generate hydrogen using this process is the formation of hydrogen iodide (HI) and sulfuric acid (H_2SO_4) through chemical reactions involving iodine (I_2), sulfur dioxide (SO_2), and water (H_2O) at an approximate temperature of 120°C, as given by Reaction 1.1. Subsequently, both H_2SO_4 and HI would undergo decomposition according to the chemical Reactions 1.2 and 1.3, respectively. A maximum temperature of 950°C has been proposed to achieve the highest possible efficiency (~40%) in H_2SO_4 decomposition reaction [7, 10]. On the other hand, a maximum operating temperature of 400°C has been recommended for the HI decomposition process. The generated hydrogen and oxygen would subsequently be separated and transferred to different storage containers. I_2 and SO_2, which are the byproducts of the overall chemical reactions, would then be recycled to have further reaction with H_2O to regenerate H_2SO_4 and HI. Thus, I_2 and SO_2 will act as catalysts.

$$I_2 + SO_2 + 2H_2O \Rightarrow 2HI + H_2SO_4 \text{ (Temperatures ~ 120°C)} \qquad \text{(Reaction 1.1)}$$

$$H_2SO_4 \Rightarrow H_2O + SO_2 + \tfrac{1}{2}\, O_2 \text{ (Temperatures ~ 950°C)} \qquad \text{(Reaction 1.2)}$$

$$2HI \Rightarrow H_2 + I_2 \text{ (Temperatures ~ 400°C)} \qquad \text{(Reaction 1.3)}$$

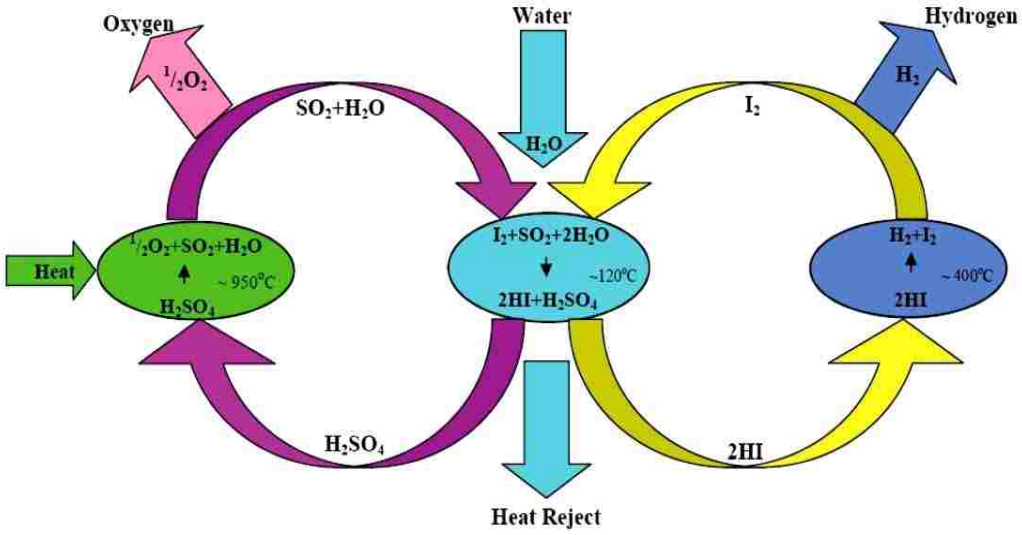

Figure 1-2 S-I Cycle

The concept of Next Generation Nuclear Plant (NGNP) program had been introduced in parallel within the charter of USDOE and Generation IV International Forum (GEN IV) [11] to foster more efficient utilization of nuclear heat to generate electricity in the twenty-first century. NGNP program has been focused on the utilization of a very high-temperature gas-cooled reactor (VHTR) concept involving a modular high-temperature gas-cooled reactor, using helium as a coolant and a closed-cycle gas turbine to generate power, in contrast to steam-based turbine used during the 1970s and 1980s. In the VHTR concept, the helium from a reactor core was planned to drive the turbine directly or indirectly by heating air or nitrogen that would drive the turbines. The reactor core outlet temperature or the turbine inlet temperature had been recommended to be in the vicinity of 950^{o}C at pressures up to 7 MPa for a design life of 60 years. Approximately 90% of

the heat generated from VHTR was proposed to be used for generating electricity while the remaining 10% would be employed in hydrogen generation.

At the inception of the Materials Research Program on nuclear hydrogen initiative (NHI) using the S-I process, several nickel - base superalloys were identified by UNLV researchers as candidate structural materials, based on an extensive literature search [12-14]. Austenitic Ni-based Alloy 617 was one of them. Later, Alloy 617 was also identified to be a suitable heat-exchanger material for application in the NGNP program [10, 19-21]. Therefore, an extensive metallurgical characterization, including the evaluation of tensile properties, fracture toughness, crack propagation rate, corrosion behavior and creep deformation of this alloy at elevated temperatures was thought to be essential to determine the suitability of this alloy for prospective applications in both NHI and NGNP programs. A schematic view of the proposed NGNP concept is illustrated in Figure 1-3.

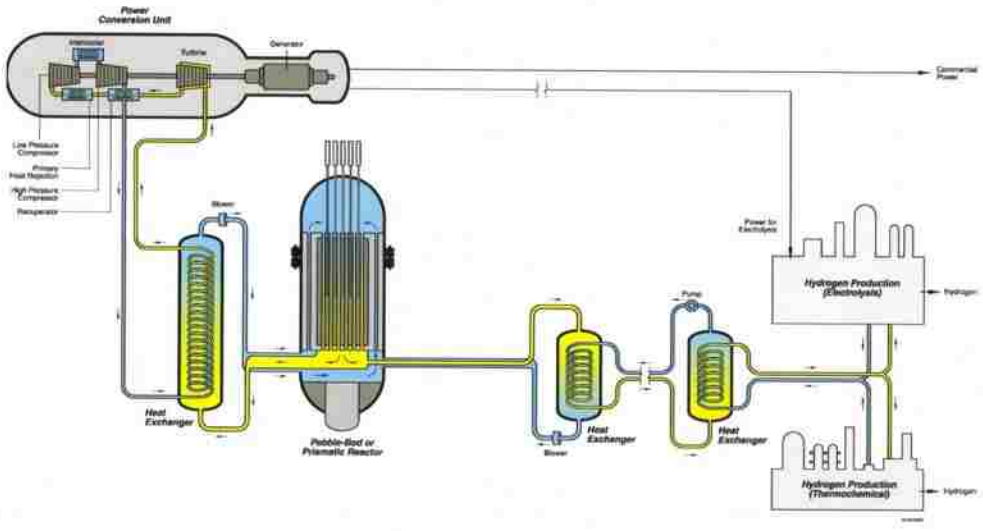

Figure 1-3 NGNP Concept

Alloy 617 was developed during 1970's as an advanced sheet material for aerospace application. This material is known to possess excellent tensile properties at elevated temperatures, and superior corrosion resistance in the presence of many hostile chemical species [15-19]. A combination of high strength and oxidation resistance at temperatures up to 1800°F (980°C) makes Alloy 617 a suitable material for ducting, combustion cans, and transition liners in both aircraft and land-based gas turbines. This alloy has been used in catalyst-grid support for production of nitric acid, heat-treating baskets and reduction boats in the refining of molybdenum due to its high temperature corrosion resistance [15, 23]. The literature data [24] indicate that this alloy has also been used in the fabrication of thermal energy storage capsules to contain eutectic fluoride mixtures of sodium, magnesium, lithium and potassium at temperatures up to 723ºC. Further, this alloy has been used in the manufacture of retort furnaces for the tritium extraction facility [25], and high temperature gas cooled reactors [26, 27].

Alloy 617 is known to possess excellent resistance to creep deformation and rupture at temperatures up to 850ºC. Further, it can maintain excellent metallurgical stability even after its prolonged exposure at elevated temperatures. Relatively lower coefficient of thermal expansion of this alloy, compared to that of most austenitic stainless steels, justifies Alloy 617 to be used in conjunction with other ferritic steels. Also, its low density provides a high strength-to-weight ratio [28]. Researchers [29] have identified Alloy 617 as a promising current-conducting material in solid oxide fuel cells since it can comply with the thermodynamic considerations required for such application. Alloy 617 has also been considered by NASA as a candidate material for heat-shields in space transportation systems [30]. This material is strengthened by the precipitation of metal

carbonitrides M(C, N) and homogeneously distributed $M_{23}C_6$ carbides resulting from a solution annealing treatment [31].

A mechanistic understanding of tensile deformation of Alloy 617 at temperatures ranging from ambient to 1000°C had earlier been developed by an UNLV investigator [32]. The structural integrity of metallic engineering components is known to be influenced by the presence of surface irregularities such as cracks. In addition, these components could be subjected to variable loading during NHI and NGNP applications by virtue of fluctuations in the operating temperatures and maintenance activities. Therefore, efforts have been made in this investigation to evaluate the crack-growth behavior of Alloy 617 at ambient and elevated temperatures using fracture-mechanics-based compact-tension specimens. The roles of temperature and load ratio (R) on crack-growth-rate of this alloy have been studied under both variable and constant stress intensity factor (K) values.

The fracture toughness of metallic materials, in terms of J-integral value, is routinely used in alloy design, material processing, material selection and specification, as well as in quality assurance. Therefore, an estimation of fracture toughness (J_{IC}) of Alloy 617 at ambient and elevated temperatures has been performed using elastic-plastic-fracture-mechanics (EPFM) concept [33].

Three temperature regimes have been identified to differentiate the types of temperature-induced degradation that may be encountered by structural materials to be used in the NGNP application. They are the high-temperature range (800-950^{o}C), the intermediate to high-temperature range (750C-850^{o}C), and the intermediate-temperature range (600-750^{o}C). In the high-temperature range, creep and creep-fatigue interaction

would be the dominant degradation modes due to quick relaxation of stresses. While the temperature would still be high enough to allow for some stress relaxation within the intermediate to high-temperature range, the resultant cracks would be able to sustain considerable amount of stresses at the crack tips. Thus, the most likely degradation modes in this temperature range would also be creep and creep-fatigue failures. Finally, in the intermediate-temperature range, the crack-tip stresses would not relax so easily, thus, leading to stress-assisted grain-boundary-oxidation (SAGBO). SAGBO is a form of stress-corrosion-cracking that could have a detrimental effect on the performance of structural materials due to oxygen transport through protective oxide films near their boundaries, thereby initiating cracks.

In view of the preceding discussion, significant efforts have been made in this study to evaluate time-dependent deformation (creep) of Alloy 617 at 750, 850 and 950 ^{o}C at applied stresses equivalent to 5, 10, 25 and 35 percent of its yield strength values. A limited number of stress-rupture testing has also been performed involving this alloy at elevated temperatures to determine the Larson-Miller parameter [34] as a function of temperature. Further, the susceptibility of this alloy to stress corrosion cracking (SCC) has been determined in an acidic solution at 100 ^{o}C for different exposure periods. SCC testing was performed to simulate an acidic condition similar to that of the H_2SO_4 decomposition process. However, testing could not be performed at higher temperatures due to the leakage of the autoclave that contained the acidic solution.

The utilization of microscopic techniques to characterize degradations is very common with all metallurgical investigations. Therefore, in-depth characterization of metallurgical microstructures, and fractographic evaluations of the tested specimens have

been performed in this study. State-of-the-art analytical tools including optical microscopy, scanning electron microscopy (SEM) and transmission electron microscopy (TEM) have been employed to achieve these goals. It is anticipated that the overall data generated from this investigation will provide a basic understanding of both mechanical and environmental degradations of Alloy 617 as functions of different parameters related to NHI and NGNP applications.

1.1 Test Matrix

As the maximum operating temperature was stipulated by the USDOE NGNP program to be 950 °C and for a long design life time dependent deformation known as creep evaluation was performed covering high temperature regime to intermediate temperature regime .Simultaneously, a consideration was also made to apply very high temperatures to evaluate the crack growth behavior (da/dN), fracture toughness (J_{IC}) and creep deformation of Alloy 617. However, at the time of the evaluation of da/dN and J_{IC}, the Instron testing equipment could not be utilized using the furnace due to its malfunctioning. Therefore, both da/dN and J_{IC} studies were performed only up to temperatures of 300 and 500 °C, respectively (the point before equipment malfunction). Further, even though the autoclave was thought to be used up to a maximum temperature of 600 °C, stress-corrosion-cracking (SCC) testing using DCB specimens could not be accommodated beyond 100 °C due to unexpected leakage. In view of all these rationales, the following test matrix (Table 1-1) was pursued.

Table 1-1 Test Matrix for Alloy 617

Type of Testing	Temperature (°C)	Test Conditions
Creep	750, 850 and 950	Air; Initial stresses = 0.05, 0.10, 0.25 and 0.35YS
Stress Rupture	750, 800 and 850	Air, Constant stress = 172 MPa
Crack-growth-rate	Ambient, 100, 300, 500, 750, 850 and 950[1]	Air, Frequency =1 Hz; Load ratios = 0.1, 0.2 and 0.3
Fracture Toughness	Ambient, 100, 200, 500, 750, 850 and 950[2]	Air; Single specimen technique
Stress-corrosion-cracking	100, 200 and 300[3] (boiling point of H_2SO_4 is 327-340 °C at 100 kPa)	H_2SO_4; pH = 1; Test durations = 1, 2, 4 and 8 months

[1] Due to equipment failure and funding constraints, testing could not be performed beyond 300 °C for CGR studies.
[2] The Instron furnace failed after 500 °C and due to funding constraints testing was stopped at that point.
[3] The autoclave could only be operated up to a temperature of 100 °C.

CHAPTER 2

TEST MATERIAL, SPECIMENS AND ENVIRONMENT

2.1 Test Material

As mentioned in the previous chapter, Ni-base Alloy 617 has been identified to be a candidate structural material, which may satisfy the performance requirements for both NHI and NGNP programs. Alloy 617 is an austenitic precipitation-hardened and face-centered-cubic (FCC) nickel-chromium-cobalt-molybdenum (Ni-Cr-Co-Mo) alloy having a combination of excellent tensile strength at elevated temperatures, better creep properties and superior corrosion resistance in many hostile environments [16-21]. The presence of high Ni content in this alloy enables significant plastic deformation in multiple slip planes and, thus, can provide enhanced ductility under the influence of tensile loading [35]. The high Ni and Cr contents make this alloy resistant to degradations while exposed to both oxidizing and reducing environments [36]. A superior oxidation resistance of this alloy may be attributed to the presence of both Cr and Al. Additionally, Co and Mo can induce significant strengthening resulting from solid-solution treatment. This alloy is easily weldable and can be readily cold-formed using conventional forming operations. However, sufficiently high forces are needed to cause plastic deformation due to its relatively high tensile strength even at elevated temperatures. The physical properties of this alloy are given in Table 2.1 [15].

Table 2-1 Physical Properties of Alloy 617

Density	0.302 lb/in^3 8.36 Mg/m^3
Melting Temperature Range	2430-2510°F 1332-1380°C
Specific Heat at 78°F (26°C)	0.1 Btu/lb-°F 419 J/kg-°C
Electrical Resistivity at 78°F (26°C)	736 ohm-circ mil/ft 1.22 μΩ-m

The experimental heat of Alloy 617 was custom-melted at the Huntington Alloys Corporation, West Virginia using a vacuum-induction-melting (VIM) practice. This VIM heat was subsequently processed into rectangular and round bars of different dimensions using forging and hot-rolling. The hot-rolled rectangular bars were subsequently subjected to cold-rolling operation to reduce their thickness. Since both round and rectangular bars had substantial residual stresses resulting from cold and hot-rolling operations, these processed materials were thermally treated to relieve these internal stresses. This thermal treatment consisted of solution-annealing at 2150°F (1175°C) for variable time periods depending on the thickness of the processed bars. Such thermal treatment is known to produce large-sized austenitic grains with annealing twins in Ni-based alloys. The strengthening of Alloy 617 is known to be the result of precipitation of metal carbonitrides M(C, N) and $M_{23}C_6$ carbides within the matrix of this alloy [37]. The chemical compositions and room temperature tensile properties of the experimental heat of Alloy 617 are given in Table 2.2 and Table 2.3 respectively.

Table 2-2 Chemical Composition of Alloy 617 (wt %)

Heat No.	C	Mn	Fe	S	Si	Cu	Cr	Ni	Al	Ti	Co	Mo	Ta
HV1160	0.06	0.121	0.002	0.009	0.004	0.001	22.10	54.80	0.87	0.29	12.17	9.52	0.001

Table 2-3 Ambient-Temperature Tensile Properties

Heat No.	Yield strength, ksi(MPa)	Ultimate tensile strength, Ksi(MPa)	%El	%RA	Hardness (R_B)
HV 1160	53.863 (371.385)	124.093 (855.621)	78.35	61.98	86.8

2.2 Test Specimens

As discussed in the earlier chapter, Alloy 617 is being considered for both NHI and NGNP applications, requiring excellent metallurgical properties and superior corrosion resistance. Metallurgical properties such as high creep and fracture rupture resistance, better plane strain fracture toughness (J_{1C}), and reduced crack propagation rates under different loading conditions are vital for Alloy 617 to be suitable for high temperature applications. Therefore, significant efforts have been made in this investigation to evaluate these properties using conventional and state-of-the-art techniques prescribed by the scientific and engineering communities. Smooth cylindrical specimens have been used for creep properties evaluation at temperatures ranging from 750 to 950°C. Double

notched cylindrical specimens were used to find the rupture time at a constant stress level. For J_{1C} measurements, pre-cracked compact-tension (CT) specimens have been used to comply with the conventional fracture mechanics principles. CT specimens have also been used for determination of crack-growth-rate (CGR) at ambient and elevated temperatures. Wedge-loaded double-cantilever-beam (DCB) specimens, based on constant displacement theory of fracture mechanics, have been used to characterize the cracking susceptibility of Alloy 617 exposed to an acidic solution at an elevated temperature for variable time periods. An in-situ crack monitoring device, known as the direct-current-potential-drop (DCPD), has been utilized to determine CGR in CT specimens. The configuration and the dimensions of each type of specimen used in metallurgical and corrosion testing are described next in the following sub-sections.

2.2.1 Compact-Tension Specimen

2.2.1.1 Crack-Growth-Rate Evaluation

Pre-cracked CT specimens having 1.25-inches (31.75 mm) length, 1.2-inches (30.48 mm) width and 0.25-inch (6.35 mm) thickness (Figure 2-1) were used to determine the crack-growth-rate (CGR) of Alloy 617. The machining of these specimens was done in compliance with the size requirements prescribed by the ASTM designation E 647-2000 [38]. The intersection of the crack starter notch tips with the two specimen surfaces were made equidistant from the top and bottom edges of the specimen within 0.005W, where W is the width of the specimen. A root radius of 0.003-inch (0.25 mm) was provided for the straight-through slot terminating in the V-notch of the specimen to facilitate fatigue pre-cracking at low stress intensity levels. A W/B ratio of 4 was maintained while machining the CT specimens [38], where B is the thickness of the specimen.

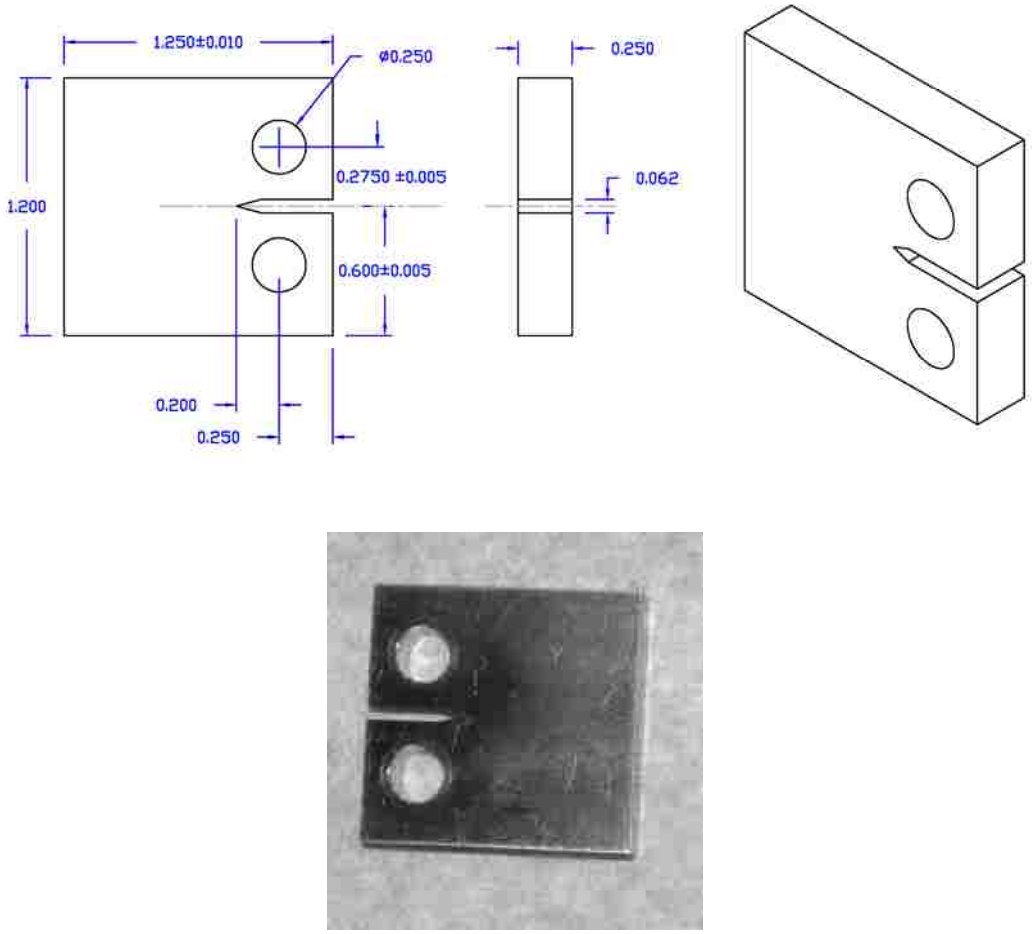

Figure 2-1 CT Specimen used in CGR Testing (inch)

2.2.1.2 Fracture Toughness Evaluation

For fracture toughness (J_{IC}) evaluation, pre-cracked CT specimens having 2.5-inches (63.5 mm) length, 2.4-inches (60.96 mm) width and 1-inch (25.4 mm) thickness, shown in Figure 2-2, were used. These specimens were machined in compliance with the size requirements prescribed by the ASTM designation E 813-1989 [39]. A root radius of 0.003-inch (0.25 mm) was provided for the straight-through slot terminating in the V-notch of the specimen to facilitate fatigue pre-cracking at low stress intensity levels. A

W/B ratio of 2 was maintained in machining these CT specimens [39], where B is the thickness of the specimen.

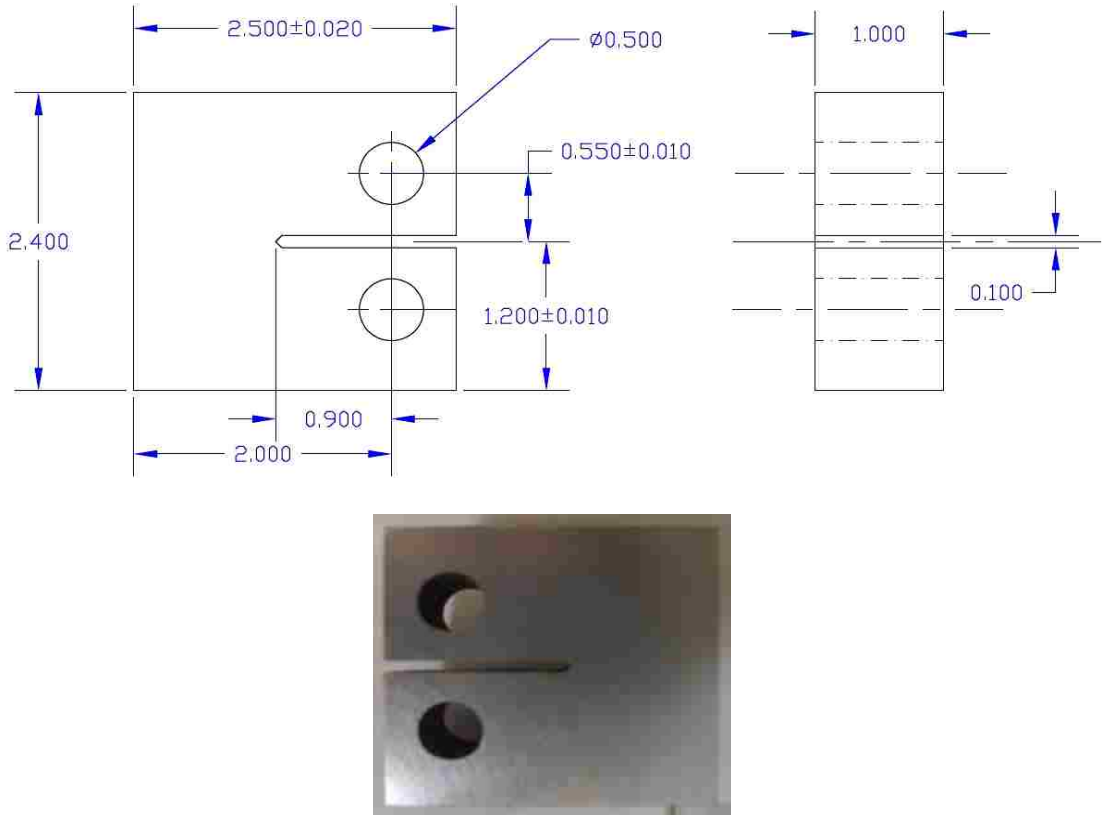

Figure 2-2 CT Specimen used in J_{IC} Testing (inch)

2.2.2 Double-Cantilever-Beam Specimen

Rectangular double-cantilever-beam (DCB) specimens, 4-inches (101.6 mm) long, 1-inch (25.4 mm) wide and 0.375-inch (9.525 mm) thick with one end slotted for wedge-loading and V-shaped side grooves extended from the slot to the opposite end, were used for the SCC study. These specimens were machined according to the NACE Standard TM0177-1990 [40]. The side grooves were machined as 20% of the wall thickness, thus maintaining a web thickness (B_n) equal to 60% of the wall thickness (i.e.

0.225-inch or 5.715 mm in this case). The fabrication of the DCB specimens was done in such a way that the crack plane was perpendicular to the short transverse direction, thus ensuring that crack propagation would occur in the longitudinal rolling direction. Machining of the side grooves was done carefully to avoid overheating and cold working. The final two passes in machine operations removed a total of 0.002-inches (0.05 mm) of the metal.

The pre-cracked DCB specimens were loaded by inserting double taper wedges, made of Alloy 617, into the specimen slots. Wedges of different thickness were inserted into the DCB slot to apply the desired load. Thus, the arm-displacement due to the insertion of the wedge resulted in different initial stress intensity factor values. The thickness of the wedge was varied from 0.11-inch (3.00 mm) to 0.126-inch (3.21 mm), as shown in Table 2-4. The dimensions of the DCB specimen, and a pictorial view of the wedge-loaded DCB specimen are illustrated in Figure 2-3 (a and b). Both dimension and pictorial view of the wedge is shown in Figure 2-4 (a and b).

Table 2-4 DCB Wedge Thickness

Test Duration ,Months	Specimen Number (Load level)	Wedge Thickness ,mm (±0.01mm)
2	1 (Low Load)	3.00
2	2 (High Load)	3.18
4	3 (Low Load)	3.01
4	4 (High Load)	3.17
8	5 (Low Load)	3.06
8	6 (High Load)	3.21

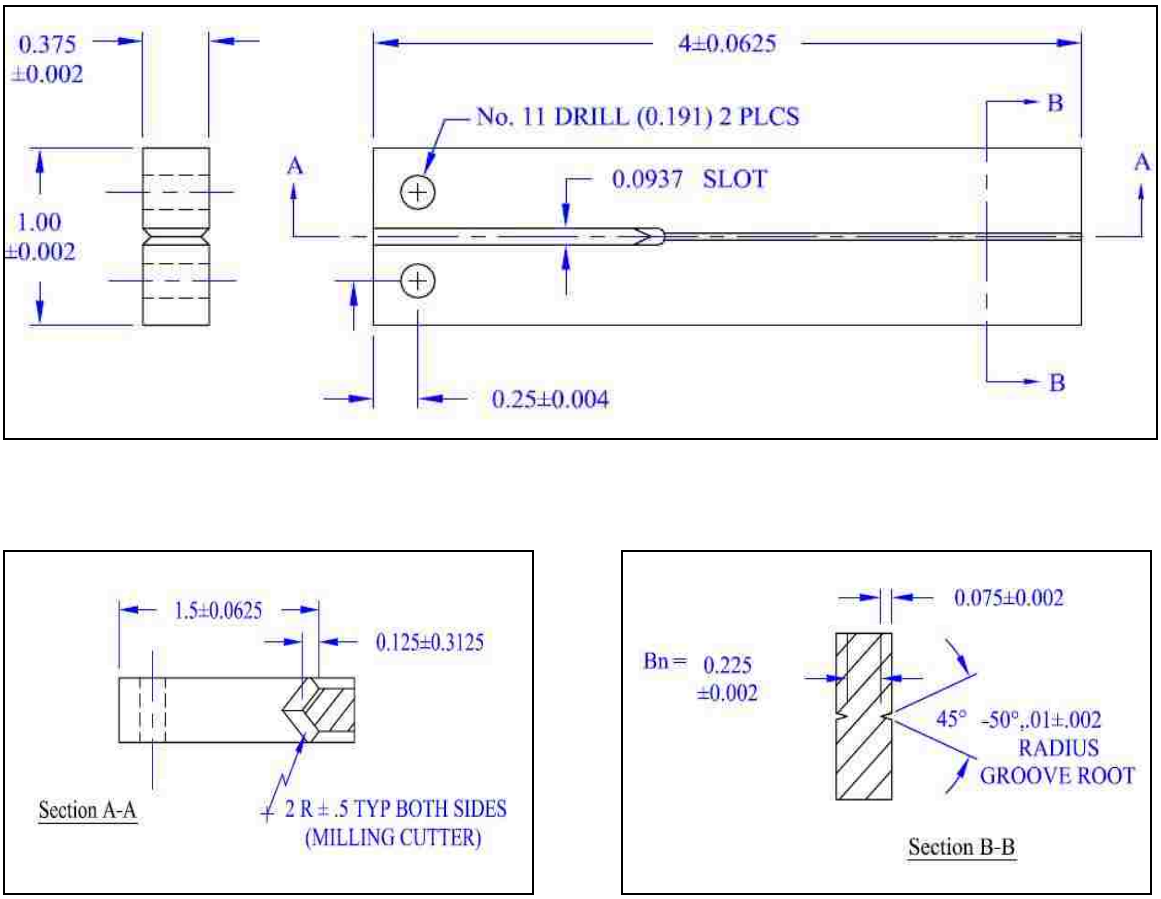

(a) Dimension

(b) Pictorial view

Figure 2-3 Wedge-Loaded DCB Specimen

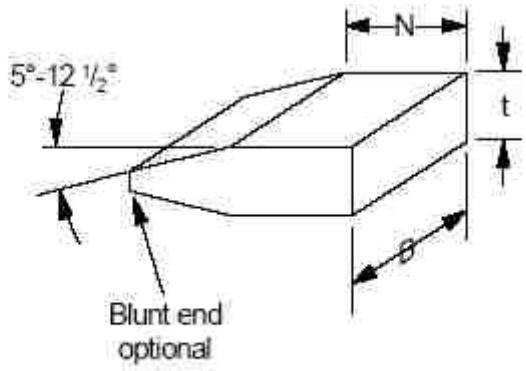

(a) Configuration

(b) Pictorial view

Figure 2-4 Double Taper Wedge

2.2.3 Creep Test Specimens

For creep testing, smooth cylindrical specimens having an overall length of 4-inches (101.6 mm) and a gage length of 1.48-inches (37.59 mm) were used. A ratio of 6:1 was maintained between the gage length and diameter. The test specimens were fabricated in such a way that the gage section was parallel to the longitudinal rolling direction. Specimens were machined according to the size requirements prescribed by the ASTM Designation E 139-2000 [41]. Circular grooves were machined at both ends

beyond the shoulder region of the specimens to attach dual extensometers for monitoring elongation during creep testing. The dimensions and a pictorial view of the creep specimen is illustrated in Figure 2-5 (a and b).

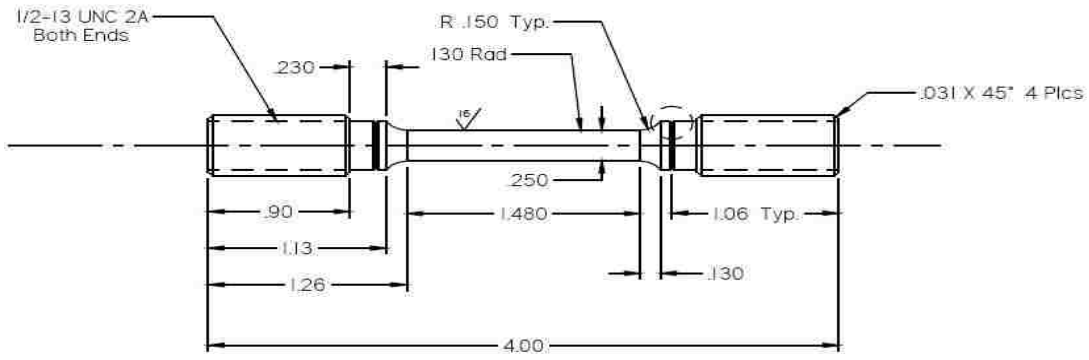

(a) Specimen Dimensions in Inches

(b)

Figure 2-5 Creep Specimen

2.2.4 Stress rupture specimens

Double grooved 3.6 inch long cylindrical specimens with a gage length of 1.1 inch were used for the stress rupture testing as shown in the Figure 2-6. These specimens had two notches at a distance of 0.5 inch centered along the gage length. The notch

diameter and root radius were 0.266 inch and 0.0073 inch, respectively as prescribed by the ASTM designation E139-2006 [42].

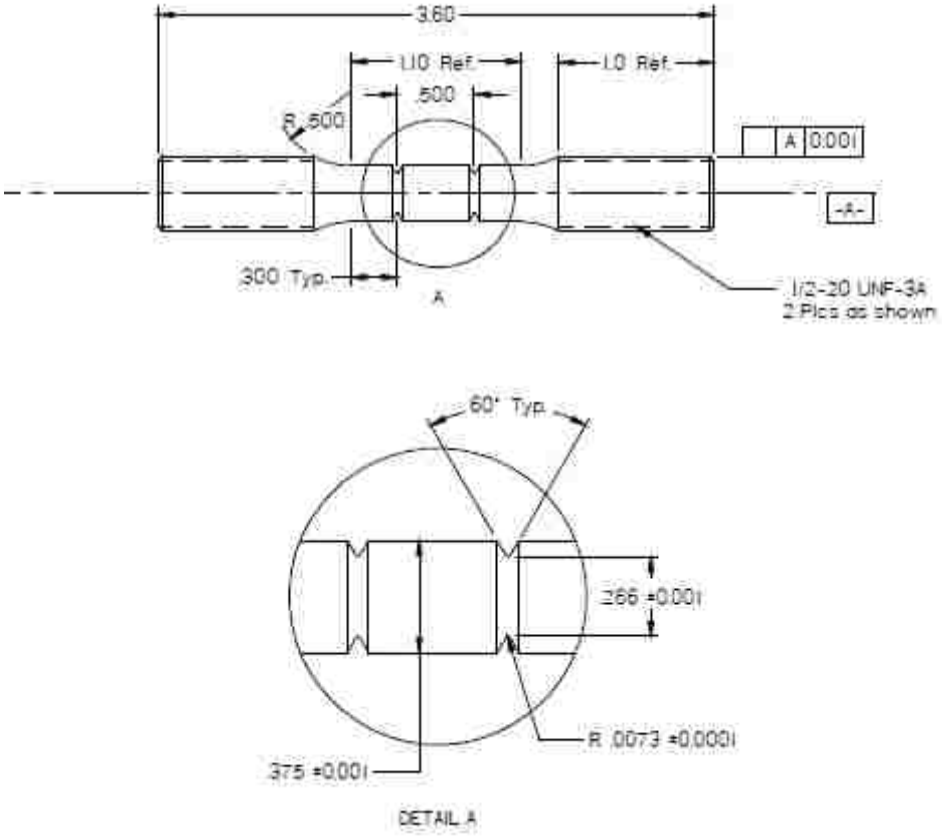

(a) Specimen Dimensions in Inches

(b) Pictorial view

Figure 2-6 Stress rupture Specimen

2.3. Test Environment

Environment can have a profound effect on the performance of structural materials to be used in the heat-exchanger associated with the nuclear hydrogen generation process. As it is mentioned earlier, the S-I process involves the formation and decomposition of H_2SO_4 and HI at different temperatures, a prototypic environmental condition could be accommodated in the corrosion testing up to 600ºC with the existing infrastructure. However, because of the leakage of the gasket in the testing equipment (autoclave), an effort was made to evaluate the corrosion behavior of Alloy 617 in an aqueous solution containing H_2SO_4 at the highest possible temperature (100 ^{o}C) at the Materials Performance Laboratory. The composition of the testing solution is given in Table 2-5.

Table 2-5 Chemical Composition of Test Solution

Solution (pH)	Deionized Water (ml)	H_2SO_4
Acidic (1.0)	4000	Added to adjust the desired pH

CHAPTER 3

EXPERIMENTAL PROCEDURES

As the title of this dissertation implies, this investigation is focused on the evaluation of the mechanical and metallurgical properties of Alloy 617 at temperatures relevant to the intermediate heat exchanger for the next generation nuclear plant and for generation of hydrogen using nuclear heat. Since the design life for NGNP application is significantly high, time dependent degradation and rupture life determination are necessary for this investigation in addition to fulfill the requirements of Section III (Class 1 at least in part for some designs) and Sections XI (inspection and repair) of the ASME code. The presence of minute flaws can influence the toughness of a metallic material under service condition, plane-strain fracture toughness (J_{1C}) of Alloy 617 has been determined at ambient and elevated temperatures using pre-cracked CT specimens. CT specimens of different dimensions were also used to evaluate the crack-growth behavior of this alloy using the DCPD in-situ crack monitoring device at different temperatures and load conditions.

The structural material to be used in the H_2SO_4 decomposition process must also have adequate resistance to environment-induced degradation, such as SCC. Therefore, an extensive effort has been made to evaluate the susceptibility of Alloy 617 to SCC using pre-cracked and wedge-loaded DCB specimens immersed in an aqueous solution containing sulfuric acid for three different durations.

The extent and morphology of failure of all tested specimens have been determined using SEM. Further, TEM has been employed to characterize linear defects known as dislocations. Simultaneously, XRD has been utilized to verify phase changes, if any,

resulting from metallurgical transformations at elevated temperatures. The use of TEM and XRD enabled a development of a deformation mechanism as functions of temperature and other metallurgical variables, which will be presented in a later section. Optical microscopy was used to determine the metallurgical microstructures and grain size calculations of Alloy 617. The different experimental procedures used in this investigation are described in the following subsections.

3.1 Creep Testing

Creep is a time-dependent enelastic deformation of a material at a constant load / stress [43, 44]. To generate a creep curve, a constant load is applied to a cylindrical specimen at a constant temperature, and the resultant strain is recorded as a function of time. Creep testing of Alloy 617 was performed at temperatures of 750, 850 and 950°C according to ASTM Designation E 139-2000 [41]. The selection of the testing temperatures was based on an understanding that meaningful creep data could be generated at a homologous temperature (ratio of test temperature, T to melting temperature, T_m) of greater than or equal to 0.5 [41, 43]. Testing was performed in an ATS Series 2330 loading frame, having a lever arm ratio of 20:1. These loading frames had a 'master' and a 'slave' component in each unit. A split-furnace (model 3210) having three heating zones was attached to each load frame to achieve the desired testing temperature. A maximum temperature of 1100 ^{o}C could be accommodated using these furnaces. Kanthal A1 was used as a heating element in these furnaces. A pictorial view of the creep testing setup including the attached furnace is illustrated in Figure 3-1.

Figure 3-1 Creep Testing Setup

Four K-type thermocouples were used to monitor the testing temperature inside the furnace. Three thermocouples were firmly attached to the test specimen at the top, middle and bottom portion, respectively. A 'Windows Computer Creep System' (WINCCS) software was used to simultaneously monitor and record the instantaneous temperature at the top, middle and bottom location of the test specimen. The elongation at the gage section of the test specimen was measured by using two extensometers, as shown in Figure 3-2. The average elongation measured by the left and right extensometer was used to analyze the creep data. Creep testing was performed for a maximum period of 1000 hours at constant applied loads equivalent to 5, 10, 25 and 35% of the yield strength (YS) values of Alloy 617 at the testing temperature. The magnitudes of the initial stress values used in creep testing are given in Table 3-1.

Figure 3-2 Extensometers used in Creep Testing

Table 3-1 Initial Stress Values used in Creep Testing

Temperature, °C	Applied Initial Stress (MPa)			
	0.05YS	0.10YS	0.25YS	0.35YS
750	11	22	54	78
850	12	24	59	83
950	9	18	46	64

At the end of each test, a three-stage creep curve was generated. The three regions of this curve are known as, primary, secondary and tertiary creep, respectively. A classical creep curve, showing three regions [45], is illustrated in Figure 3-3. At the onset of each creep test, there is an instantaneous elastic plus plastic strain (ε_0) resulting from the initial applied stress. The creep rate then decreases with time in the primary creep region,

followed by a steady-state creep region. The slope of the secondary or steady-state creep curve ($d\varepsilon/dt$, or $\dot{\varepsilon}$) is known as creep rate of the tested material. Finally the creep rate increases rapidly, showing a steeper tertiary curve until failure.

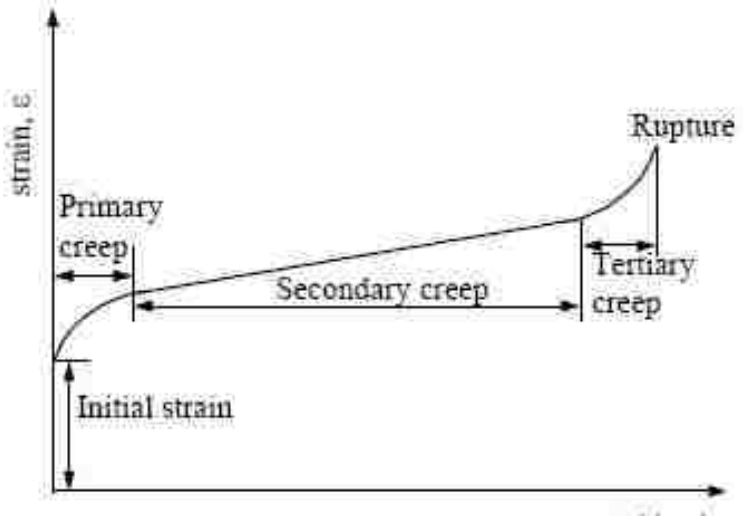

Figure 3-3 Three-Stage Creep Curve

3.1.1 Determination of Activation Energy

The steady-state creep rate of metals and alloys is a function of temperature. The driving force for deformation in the secondary stage is expressed in terms of an activation energy (Q). The magnitude of Q can be determined by three different techniques. One method of determination of Q is to consider Equation 3-1 [43], showing a temperature dependency of $\dot{\varepsilon}_s$.

$$\dot{\varepsilon}_s = A \exp(-Q/RT) \qquad \text{Equation 3-1}$$

where

$\dot{\varepsilon}_s$ = Steady-state creep rate, sec^{-1}

A = A pre-exponential complex constant containing the frequency of vibration of the flow unit, the entropy change, and a factor that depends on the structure of the material

T = Absolute temperature, K

Taking natural logarithms on both sides of Equation 3-1,

$$\ln (\dot{\varepsilon}_s) = [-Q/R] (1/T) + \ln (A) \qquad \text{Equation 3-2}$$

Equation 3-2 represents a straight line with an equation in the form of y = mx + c, when $\ln (\dot{\varepsilon}_s)$ is plotted against (1/T). The magnitude of Q can be calculated from the negative slope (-Q/R) by substituting the known value of R (gas constant).

The second method for determining the Q value is based on the consideration of Equation 3-3, which can be rearranged as Equation 3-4 for two testing temperatures of T_1 and T_2.

$$A = \dot{\varepsilon}_1 \exp (Q/RT_1) = \dot{\varepsilon}_2 \exp (Q/RT_2) \qquad \text{Equation 3-3}$$

$$Q = \frac{R \ln (\dot{\varepsilon}_1 / \dot{\varepsilon}_2)}{(1/T_2 - 1/T_1)} \qquad \text{Equation 3-4}$$

where

$\dot{\varepsilon}_1$ and $\dot{\varepsilon}_2$ = Steady-state creep rates at temperatures T_1 and T_2, respectively

The third method of Q calculation takes both temperature and stress dependency of steady-state creep rate into consideration, as given by Equation 3-5 [46]. The Q value can

be computed from this equation by using three sets of $\dot{\varepsilon}$, σ and T values, and a related process of elimination.

$$\dot{\varepsilon} = A\sigma^{n}\exp\left(-Q/RT\right) \qquad \text{Equation 3-5}$$

where

$\dot{\varepsilon}$ = Minimum or steady-state creep rate, sec^{-1}

σ = Applied stress, MPa

n = Stress exponent

Q = Apparent activation energy for creep deformation, kJ/mole

A = A constant

3.2 Stress Rupture Testing

Stress rupture test is similar to creep test, except that the specimen is normally loaded at higher stresses as compared to creep test and is continued until failure. Stress rupture tests was performed on Alloy 617 in this study in accordance with the ASTM Designation E 139-06 [42]. Two ATS loading frames series 2330, shown in Figure 3-1, with an arm ratio of 20:1 have been used in stress rupture testing. The load frames were the same as that used for creep test. The only difference was that stress rupture testing was carried out using auto load mode. The load was applied automatically by the frames and maintained at a constant level till rupture of the specimen. The test did not require any elongation measurement, therefore, none of the extensometers were used as in the creep test. Four K-type thermocouples, three firmly attached with the specimen and one for the ambient reference temperature measurement, was used to monitor the testing

temperature. WINCCS software can monitor top/middle/bottom thermocouple instantaneous temperatures and time to rupture of the specimen simultaneously.

Larson-Miller parameter was calculated based on the equation 3-6 [34], which could be further used to construction of master plot for long time creep life prediction.

$$LMP = T(\log t + C) \qquad \text{Equation 3.6}$$

Where

T = test temperature° R = ° F + 460

t = time to rupture, hour

C = Larson –Miller constant, varies from 15 to 25 depending on material

3.3 Crack-Growth-Rate Testing

Crack-growth-rate (CGR) testing involving compact-tension (CT) specimens of Alloy 617 was performed in accordance with the ASTM Designation E 647-2000 [47]. Testing was performed at temperatures ranging from ambient to 300 ^{o}C under three different load ratios (R = Minimum load/Maximum load) of 0.1, 0.2 and 0.3, keeping the frequency of loading at 1 Hz. Prior to CGR testing, the CT specimens were pre-cracked up to a length of 2 mm under cyclic loading. Testing was performed using a constant maximum load P_{max} of 5 kN, and the magnitude of minimum load P_{min} was varied to maintain R values of 0.1, 0.2, and 0.3, respectively. The magnitudes of maximum and minimum stresses σ_{max} and σ_{min} were determined from P_{max} and P_{min}, which were used to calculate the maximum and minimum stress intensity factor values K_{max} and K_{min}.

3.3.1 Instron Testing Machine

The Instron testing machine, shown in Figure 3-4, had an axial load transducer capacity of 22.5 kip (100 kN). It had a single screw electromechanical top actuator that was developed for static and quasi-dynamic cyclic testing at slow speed. This equipment consisted of a large heavy-duty load frame with an adjustable crosshead attached to the top grip, and a movable actuator with another grip at the bottom to enable loading and unloading of the test specimen. The axial motion was controlled by force, displacement, or an external signal from the strain gage. The specimen was mounted between the two grips and pulled by the movable actuator. The load cell measured the applied force on the CT specimen. The movement of the upper crosshead relative to the lower one measured the strain within the specimen and consequently, the applied load. The key specifications of the Instron equipment are given in Table 3-2 [48].

Table 3-2 Specifications of Instron Model 8862 System

Load Capacity	Total Actuator Stroke	Maximum Ramp Rate	Actuator Attachment Threads	Load Cell Attachment Threads
100 kN	100 mm	350 mm/min	M30 × 2	M30 × 2

A split furnace (model MDS1735A) was attached to the testing system for elevated temperature testing. This furnace was capable of sustaining a maximum temperature of 1500°C, and consisted of two water-cooled stainless steel jackets that provided a safe ergonomic outer surface for operation. This furnace had two layers of micro-pores and

ceramic fibers over them. Six U-shaped molybdenum disilicide heating elements were used for attaining the desired testing temperature. The specimen temperature during testing was monitored by three B-type thermocouples contained inside the test chamber. A separate control panel (model CU666F) was used to perform the overall monitoring of temperature during testing. By design, a maximum heating rate of 10 °C per minute could be achieved by this control panel. However, a slow heating rate of 4 °C per minute was used during CGR and fracture toughness testing to prevent any thermal shock of the pull rods and the fixtures inside the furnace. Since the grip material could undergo phase transformation and plastic deformation at elevated temperatures during straining of the specimen, a pair of custom-made grips of high strength and temperature resistant MarM 246 alloy was used to hold the specimen in an aligned position.

Figure 3-4 Instron Testing Machine

3.3.2 DCPD In-situ Crack Monitoring Device

The CGR was measured using an in-situ crack monitoring technique, known as direct-current-potential-drop (DCPD). In this process, the changes in crack length were measured from the potential or voltage drop between the two arms of the specimen as crack propagates [49-52]. Two wires (current probes) were attached (spot-welded) to the top and bottom faces of the specimen, as shown in Figure 3-5, which allowed the flow of constant current (3 milliamps) into the specimen. Two additional wires (voltage/potential probes) were welded to the arms of the specimen that measured the resultant potential drop due to an increase in resistance resulting from the extension of the crack length under the influence of cyclic loading. The applied current was provided by a PD-501 Amplifier (Figure 3-6), and the resultant voltage drop was recorded and analyzed by an ADwin-GOLD controller, shown in Figure 3-7. As the crack length increases, the gap between the two loaded arms of the specimen increases, thus, the electrical resistance increases. This increase in electrical resistance gives rise to an increase in potential difference or voltage drop between the two arms of the specimen spanning the crack length, which was recorded by use of a software program [53] provided by Fracture Technology Associates (FTA). The potential drop was converted to crack extension using Johnson's Formula [54-57], given by Equation 3-7.

$$a = \frac{W}{\pi}\cos^{-1}\left[\frac{\cosh\left(\frac{\pi}{W}\times Y_o\right)}{\cosh\left[\frac{V}{V_r}\times\cosh^{-1}\left[\frac{\cosh\left(\frac{\pi}{W}\times Y_o\right)}{\cos\left(\frac{\pi}{W}\times a_r\right)}\right]\right]}\right] \qquad \text{Equation 3-7}$$

where

a = Crack size, mm

a_r = Reference crack size from some other method, mm

W = Specimen width, mm

V = Measured potential drop, volt

V_r = Measured voltage corresponding to a_r

Y_o = Voltage measurement lead spacing from the crack plane

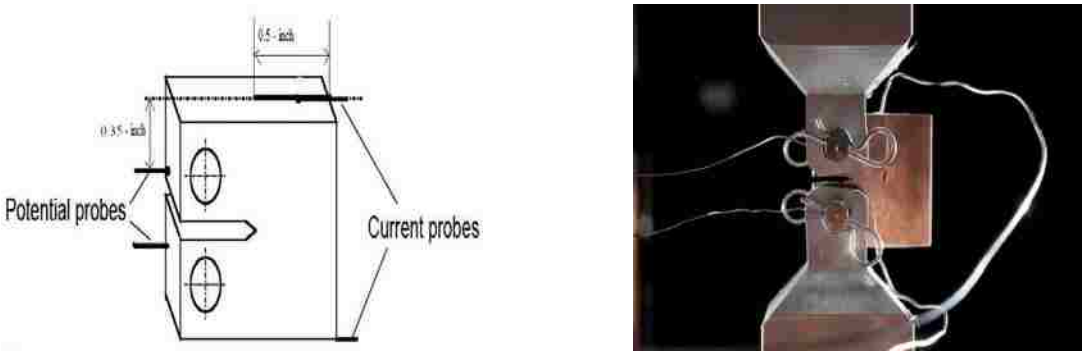

Figure 3-5 DCPD Test Setup

Figure 3-6 PD-501 Amplifier

Figure 3-7 ADwin-GOLD Controller

At the end of each test, the FTA software program enabled the analyses of the recorded data, and subsequently generated plots of da/dN versus ΔK, showing a three-stage curve

including a threshold crack-growth, steady-state crack-growth, and an unstable crack-growth regions. The steady-state crack-growth region is generally governed by the Paris Law [58-60], given by Equation 3-8, also known as the Paris regime. A classical da/dN versus ΔK plot, showing these three regions is illustrated in Figure 3-8 [32].

$$da/dN = A\,(\Delta K)^m \qquad \text{Equation 3-8}$$

where

da/dN = Crack-growth-rate, mm/cycle

ΔK = Stress intensity factor range ($K_{max} - K_{min}$), MPa√m

K_{max} = Maximum stress intensity factor (MPa√m)

K_{min} = Minimum stress intensity factor (MPa√m)

A = Crack-growth coefficient, MPa√m

m = Slope of the linear portion of log da/dN versus log ΔK plot

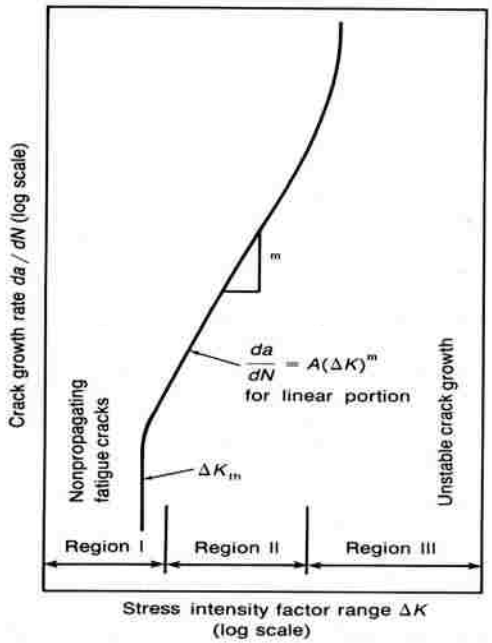

Figure 3-8 da/dN vs. ΔK Plot

The overall data generated from CGR testing, and the resultant plots include the magnitudes of m and A, and the number of cycles to failure N_f. Further, the magnitude of threshold stress intensity factor range (ΔK_{th}) can also be determined that represent a ΔK value below which no crack-growth of the tested material occurs even under cyclic loading [38]. However, for all tested conditions, the magnitude of ΔK_{th} was taken to be equivalent to a ΔK value that corresponds to a da/dN value of 10^{-7} mm/cycle [38]. The magnitude of N_f was calculated by using Equation 3-9, given below [61].

$$N_f = \left[\frac{a_f^{\left(1-\frac{m}{2}\right)} - a_i^{\left(1-\frac{m}{2}\right)}}{A(\sigma_r)^m \alpha^m \pi^{\frac{m}{2}}}\right]\left[\frac{1}{1-\frac{m}{2}}\right] \qquad \text{Equation 3-9}$$

where

a_f = Final crack-length, mm

a_i = Initial crack-length, mm

σ_r = Stress range ($\sigma_{max} - \sigma_{min}$), MPa

σ_{max} = Maximum stress, MPa

σ_{min} = Minimum stress, MPa

α = Geometric factor of the specimen (5.317), determined by using Equation 3-10 for a 0.25-inch thick CT specimen

$$\alpha = \frac{\left[2+\frac{a_0}{W}\right]\left[0.886+4.64\left(\frac{a_0}{W}\right)-13.32\left(\frac{a_0}{W}\right)^2+14.72\left(\frac{a_0}{W}\right)^3-5.6\left(\frac{a_0}{W}\right)^4\right]}{\left(1-\frac{a_0}{W}\right)^{\frac{3}{2}}} \qquad \text{Equation 3-10}$$

where

W = Width of the CT specimen, mm

3.3.3 Activation Energy Evaluation

It is well known [62] that crack tip stresses developed under cyclic loading are sufficiently high to cause plastic deformation, leading to instantaneous generation and multiplication of lattice defects such as dislocations, eventually causing dislocation pile-ups near grain boundaries. Thus, no thermal activation is needed. However, the movement of dislocations is a thermally- activated process. Dislocation motion can cause plastic crack-extension, which is also expected to be thermally activated with activation energy (Q) being the same as that for dislocation movement. If m is considered to be independent of the testing temperature, Equation 3-7 can be modified to Equation 3-11, taking Q into consideration for crack-growth [62-65].

$$da/dN = A_o [\exp (-Q/RT)] (\Delta K)^m \qquad \text{Equation 3-11}$$

where

R = Universal gas constant, 8.314 J/mol.K

A_o = A material constant, which is independent of temperature, and can be related to A, as shown in Equation 3-12 [62-65]

$$A = A_0 [\exp (-Q/RT)] \qquad \text{Equation 3-12}$$

Taking natural logarithm on both sides of Equation 3-12 and re-arranging, one can get

$$\ln (A) = [-Q/R]1/T + \ln (A_0) \qquad \text{Equation 3-13}$$

Equation 3-13 represents a straight line with a slope and an intercept of –Q/R and ln (A_0), respectively, when ln (A) is plotted against 1/T. Using the value of R, one can determine the magnitude of Q.

3.3.4 CGR Testing at Constant K_{max}, K_{min} and ΔK

Efforts were also made to determine CGR of Alloy 617 under constant K_{max}, K_{min} and ΔK values at ambient temperature, while maintaining an R value of 0.1. It should be noted that, as crack propagated under constant K values, the maximum and minimum loads P_{max} and P_{min} values were automatically adjusted by the software used to maintain constant values of K_{max} and K_{min} , and thus, a constant ΔK value, too. The magnitudes of K_{max}, K_{min} and ΔK used in constant-K CGR testing are given in Table 3-3.

Table 3-3 K_{max}, K_{min} and ΔK Values used in Constant-K Testing

Specimen No.	K_{max} (MPa$\sqrt{m}$)	K_{min} (MPa$\sqrt{m}$)	ΔK (MPa$\sqrt{m}$)
1	26.25	2.625	23.63
2	27.65	2.765	24.88
3	29.07	2.907	26.17

3.4 Fracture Toughness Evaluation

At first, attempts were made to evaluate the fracture toughness of Alloy 617 in terms of plane strain fracture toughness (K_{IC}), based on the linear-elastic-fracture-mechanics (LEFM) concept [61]. However, the determination of K_{IC} was not feasible from a practical standpoint since significantly thicker CT specimens (approximately 20" thick for Ni based super alloys) were needed to comply with the LEFM criterion. Therefore, elastic-plastic-fracture-mechanics (EPFM) concept was used to evaluate the fracture toughness of this alloy in terms of J_{IC} involving 1-inch thick CT specimens. The

determination of J_{IC} was based on a procedure prescribed by the ASTM Designation E 813-1989 [39].

In essence, two types of J_{IC} testing methods exist, namely single-specimen technique and multiple-specimen technique. The multiple-specimen technique [39] requires at least five specimens to be tested at a particular temperature to determine the J_{IC} value. Therefore, the single-specimen technique was used to determine the J_{IC} value of Alloy 617 in this study using the Instron testing machine. Testing was conducted at temperatures ranging from ambient to 500°C. A 'J_{IC} Fracture Toughness Software' [66], provided by the Instron Corporation, was used to calculate and validate the J_{IC} value. The detailed procedure associated with such evaluation is described next.

The CT specimen was pre-cracked to an approximate length of 3 mm using an R value of 0.1 and a frequency of 1 Hz. The maximum load used in pre-cracking was based on Equation 3-14 [39], which was maintained at 20 kN. The overall variables used during pre-cracking are shown in Table 3-4.

Table3-4 Pre cracking of 1" CT specimen

Serial No	Pre cracking Temp (^{o}C)	Max. load (kN)	Load Ratio	Frequency (Hz)	No. of cycle	Pre- crack length (mm)
1	RT	20	0.1	1	70,000	4.03
2	RT	20	0.1	1	65,000	5.3
3	RT	20	0.1	1	55,000	3.28
4	RT	20	0.1	1	58,000	3.73

Following pre-cracking, the specimen was subjected to thirty loading and unloading cycles. Due to these loading/unloading cycles, the load-line-displacement (LLD) or, the crack-opening-displacement (COD), i.e., the gap between the two arms of the CT specimen was enhanced. The LLD was measured by a high-temperature knife-edge extensometer, which was attached to the specimen arms at the onset of testing. The maximum travel distance of the extensometer was kept at +/- 2 mm. The J_{IC} test setup used in this investigation is shown in Figure 3-9. A typical load versus LLD plot is shown in Figure 3-10 (a).

$$P_L = \frac{Bb_0^2\sigma_Y}{(2W+a_0)} \qquad \text{Equation 3-14}$$

where

P_L = Maximum load during pre-cracking, N

B = Thickness of the specimen, mm

b_0 = Uncracked ligament, mm

σ_Y = Effective yield strength of the material, MPa

W = Width of the specimen, mm

a_0 = Pre-crack length, mm

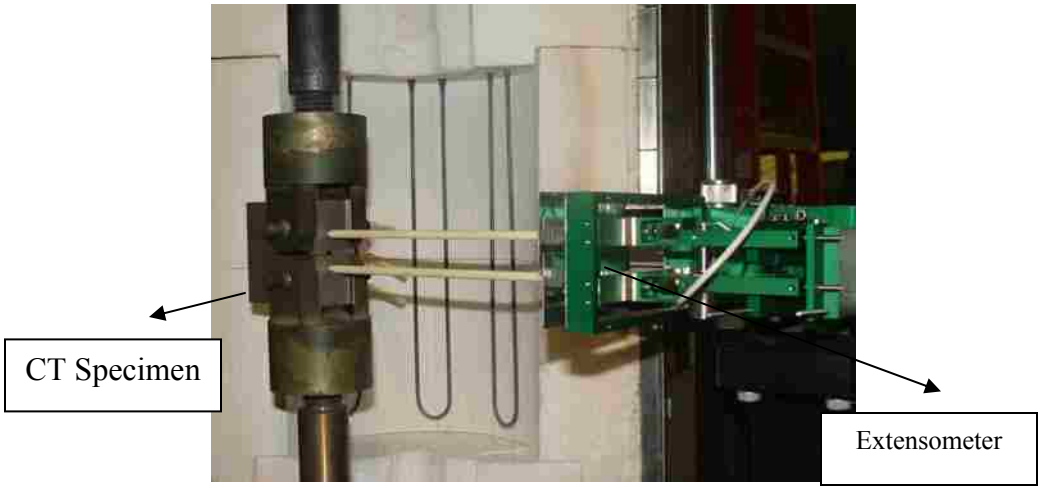

Figure 3-9 J_{IC} Test Setup

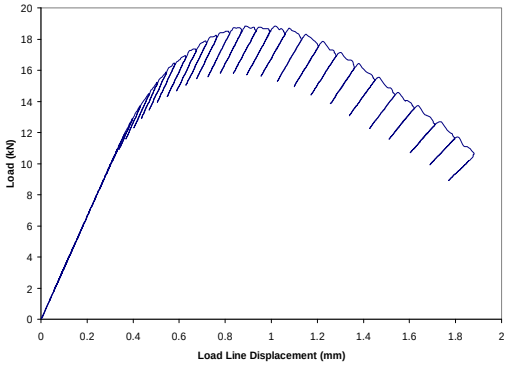

Figure 3-10 (a) Load versus LLD Plot

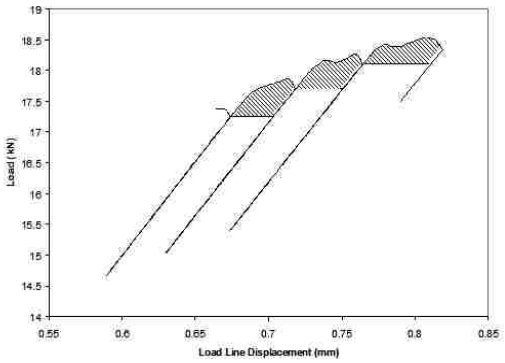

Figure 3-10 (b) Areas Representing J-Integral

The shaded area corresponding to each loading/unloading cycle, shown in Figure 3-10 (b), represents the energy (J-Integral) needed to cause an increment in crack length. The crack increases by a certain amount during each loading/unloading sequence. The J-Integral value for each area was calculated using Equation 3-15 [39, 67].

$$J = J_{elastic} + J_{plastic} \qquad \text{Equation 3-15}$$

where

$$J_{elastic} = \frac{K^2}{E}\left[1 - \nu^2\right], \text{ and} \qquad \text{Equation 3-16}$$

$$J_{plastic} = \frac{\eta_{pl}}{Bb}\int_0^{v_{pl}} Pdv_{pl} = \frac{\eta_{pl}}{Bb} \times A_{pl} \qquad \text{Equation 3-17}$$

$$K = \text{Stress intensity factor} \left[\frac{P}{\left(BB_N W\right)^{0.5}}\right] \times \alpha, \text{ MPa}\sqrt{\text{m}}$$

P = Load, N

B = Specimen thickness, mm

B_N = Net specimen thickness = B (in present study), mm

W = Width of the specimen, mm

α = Geometric factor of the specimen

E = Elastic modulus of the material

ν = Poisson's ratio of the material (0.3)

b = Uncracked ligament, mm

$\eta_{pl} = 2 + 0.522b/W$

ν_{pl} = LLD / COD

A_{pl} = Area corresponding to each loading / unloading sequence, mm^2

The calculated J value was then plotted against the corresponding crack extension, as shown in Figure 3-11. The crack extension (a_i) for each sequence was measured by the unloading compliance principle, given by Equation 3-18 [39].

$$a_i/W = 1.000196 - 4.06319u_{LL} + 11.242u_{LL}^2 - 106.043u_{LL}^3 + 464.335u_{LL}^4 - 650.677u_{LL}^5 \qquad \text{Equation 3-18}$$

where

$$u_{LL} = \frac{1}{\left[B_e E C_i\right]^{0.5} + 1}$$

B_e = Effective thickness of the CT specimen = $[B - (B - B_N)^2/B] = B$ (since $B = B_N$ in the current study), mm

C_i = Specimen load line elastic compliance on an unloading/reloading sequence ($\Delta v/\Delta P$), mm/N

Δv = Increment in LLD/COD, mm

ΔP = Change in load, N

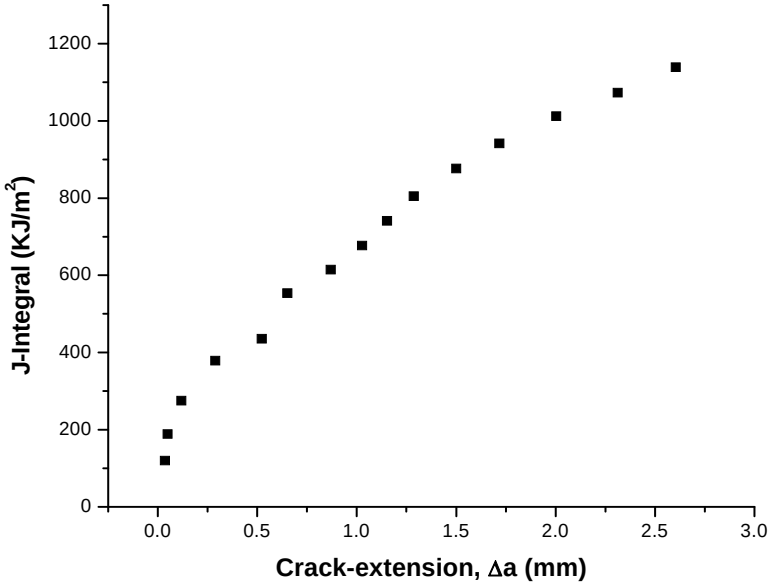

Figure 3-11 J-Integral vs. Crack-Extension

The data shown in Figure 3-11 were fitted to a power law regression curve, and four parallel lines were then drawn, as shown in Figure 3-12. These lines are referred to as the blunting line, 0.15-mm exclusion line, 0.2-mm exclusion line, and 1.5-mm exclusion line. The blunting line was drawn using Equation 3-19, and all other lines were drawn parallel

to it. The J - Δa data are considered to be valid if at least one J - Δa point lies between the 0.15-mm exclusion line and a line parallel to the blunting line at an offset of 0.5-mm from the blunting line.

$$J = 2\sigma_Y \Delta a \qquad \text{Equation 3-19}$$

The point of intersection of the regression curve and the 0.2-mm exclusion line (as shown in Figure 3-12) is usually taken as J_Q, or the conditional J_{IC} value. J_Q is considered to be the J_{IC} value if the following two criteria are met.

i. Thickness (B) of the specimen > [25 J_Q / σ_Y], where σ_Y = effective yield strength of the material = average of the yield and ultimate tensile strength (σ_{YS} and σ_{UTS}, respectively) of the material = [σ_{YS} + σ_{UTS}] / 2, and

ii. Initial uncracked ligament (b_0) > [25 J_Q / σ_Y]

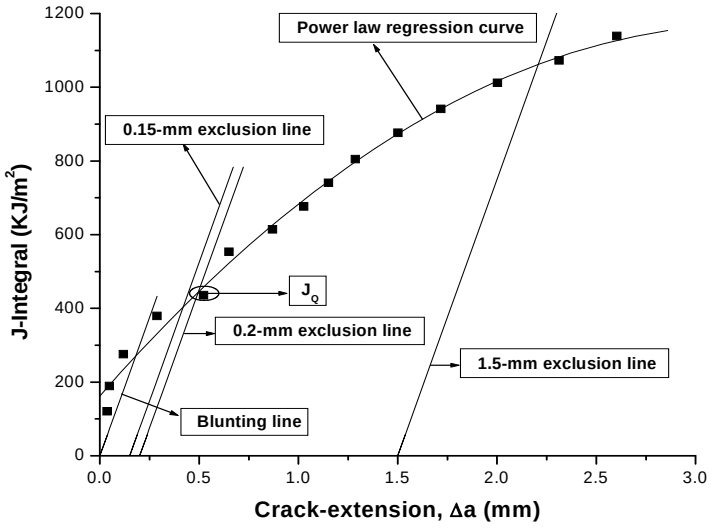

Figure 3-12 Determination of J_Q from J-Integral vs. Δa Plot

Efforts were also made to correlate J_{IC} to K_{IC}. Literature [61, 68, 69] suggests that K_{IC} can be calculated from the J_{IC} value according to Equation 3-20, as given below.

$$K_{IC} = \sqrt{J_{IC} \times E / \left(1 - \nu^2\right)} \qquad \text{Equation 3-20}$$

Fracture toughness can also be measured using the crack-tip-opening-displacement (CTOD) method, which is based on Equation 3-21, given below [61, 70].

$$\delta = \frac{K_1^2}{mE\sigma_{YS}} \qquad \text{Equation 3-21}$$

where

δ = CTOD, mm

$K_1 = K_{IC}$ value of the material, MPa$\sqrt{m}$

m = Constant = 2 for plane-strain condition

3.4.1 Determination of Tearing Modulus

During fracture toughness testing, or loading in tension, an instability arises that can cause continuous crack extension by a so-called 'tearing' mechanism. A dimensionless parameter, tearing modulus (T), of a material is defined as the material's resistance to such instability, and can be given by Equation 3-22 [71-73].

$$T = \frac{E}{\sigma_f} * \frac{dJ}{da} \qquad \text{Equation 3-22}$$

where

$\frac{dJ}{da}$ = Slope of the J-Δa curve

σ_f = flow strength = $\frac{1}{2}\left(\sigma_y + \sigma_{UTS}\right)$

The materials resistance to tearing instability, identified here as tearing modulus (T), depends only on the slope of the J-integral R-curve and other well known properties, the flow stress (σ_f), in simple tension and modulus of elasticity (E).

3.5 SCC Testing

Stress-corrosion-cracking (SCC) testing using DCB specimens of Alloy 617 was performed in a 100 °C acidic solution for exposure periods of 2, 4 and 8 months. The DCB specimens were loaded by inserting double-taper wedges of similar material with different thickness into their slots [40, 74, 75]. Prior to their loading, they were pre-cracked in the Instron equipment according to ASTM Designation E 399–1990 [76]. A cyclic loading with an R value of 0.1 and a frequency of 1 Hz was used in pre-cracking the DCB specimens. The wedge thickness was determined based on the linear portion (within the elastic region) of the load versus displacement curve of this alloy. A typical load versus displacement plot for a DCB specimen of Alloy 617 is shown in Figure 3-13. Two sets of load and displacement were selected to load the DCB specimens by inserting wedges of different thickness. The wedge thickness was calculated using Equation 3-23.

$$W = (t + \delta) \qquad \text{Equation 3-23}$$

where

W = Wedge thickness

t = Initial gap between the two arms of the DCB specimen

δ = Displacement corresponding to a desired load (from the load-displacement plot)

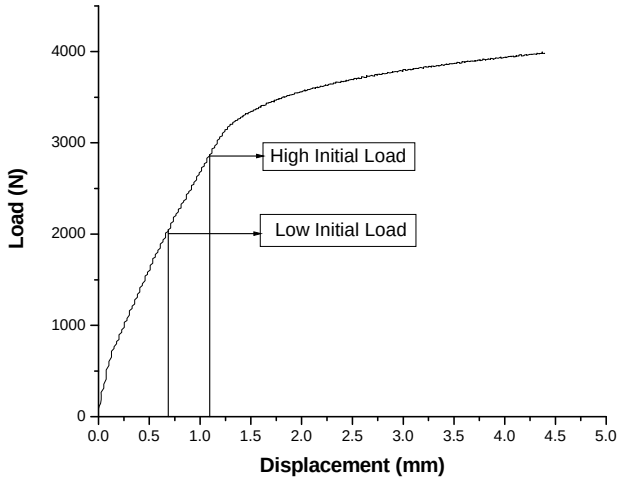

Figure 3-13 Load vs. Displacement Plot

The initial and the final stress intensity factor (K_I and K_f) values were computed using Equation 3-24, prescribed by the Nace Standard TM0177-1990 [40]. The pre-cracked and wedge-loaded DCB specimens were then immersed into an acidic solution contained in an autoclave (Figure 3-14).

$$K=\frac{Pa\left(2\sqrt{3}+2.38h/a\right)\left(B/B_n\right)^{1/\sqrt{3}}}{Bh^{3/2}} \qquad \text{Equation 3-24}$$

where

P = Wedge load (before or after exposure to the environment), measured in the loading plane

a = Initial or final crack length, measured from the load line

h = Height of each arm

B = Specimen thickness

B_n = Web thickness

Figure 3-14 DCB Test Setup

Upon completion of testing, the specimens were broken apart in the Instron machine, and the final crack length was measured on the broken faces [75, 76]. The final load and the crack length were used to calculate the final stress intensity factor (K_f) value due to SCC. Fractographic studies were subsequently conducted on the broken specimens to determine the extent and mode of cracking.

3.6 Metallographic Evaluations

The metallographic technique, using an optical microscope, enables the characterization of phases present, their distributions within grains and their sizes that depend on both the chemical composition and the thermal treatment of the test material. The principle of an optical microscope is based on the impingement of a light source perpendicular to the test specimen. The light rays pass through the system of condensing lenses and the shutters up to the half-penetrating mirror. This brings the light rays through the objective to the surface of the specimen. Light rays are reflected off the surface of the sample, which then return to the objective, where they are gathered and

focused to form the primary image. This image is then projected to the magnifying system of the eyepiece. The contrast observed under the microscope results from either an inherent difference in intensity or wavelength of the light absorption characteristics of the phases present. It may also be induced by preferential staining or attack of the surface by etching with a chemical reagent.

The test specimens were sectioned, and mounted using the standard metallographic technique, followed by polishing and etching to reveal their metallurgical microstructures. Etching of the polished surface was done using Kalling's reagent. This etchant contained 2 grams of cupric chloride ($CuCl_2$), 40 ml of hydrochloric acid (HCl) and 80ml of methanol (CH_3OH) [77]. The polished and etched specimens were then evaluated for determination of their microstructures in a Leica optical microscope, shown in Figure 3-15. This microscope was capable of resolution of up to 1000X. A digital camera with a resolution of 1 Mega pixel enabled the image capture on a computer screen, utilizing the Leica software.

Figure 3-15 Leica Optical Microscope

3.6.1 Grain Size Evaluation

Efforts were made to determine the grain size of the tested materials from their optical micrographs. The ASTM grain number (G) as well as the grain size (diameter D) were determined using the 'mean linear intercept method,' prescribed by the ASTM Designation E 112-1996 [78]. The following steps were used to determine the G and D values.

- First, a template (Figure 3-16) consisting of three concentric circles with a total length of 500 mm was placed over the resultant optical micrograph, and the total number of grain boundary intersections with these test lines was determined.

- Then, the mean lineal intercept length ($\bar{L}_L$) was determined by using Equation 3-25.

$$\bar{L}_L = \frac{L_T}{PM} \qquad \text{Equation 3-25}$$

where

L_T = Total length of test lines

P = Total number of grain boundary intersections

M = Magnification of the micrograph

- Next, the value of G was calculated using Equation 3-26.

$$G = -3.2877 - 6.438 \log \bar{L}_L \qquad \text{Equation 3-26}$$

- Finally, the grain diameter (D) was determined using Equations 3-27 and 3-28, shown below.

$$N = 2^{G-1} \qquad \text{Equation 3-27}$$

$$D = \frac{1}{\sqrt{N}} \qquad \text{Equation 3-28}$$

where

N = Number of grains/sq. mm at a magnification of 1X

D = Grain diameter, mm

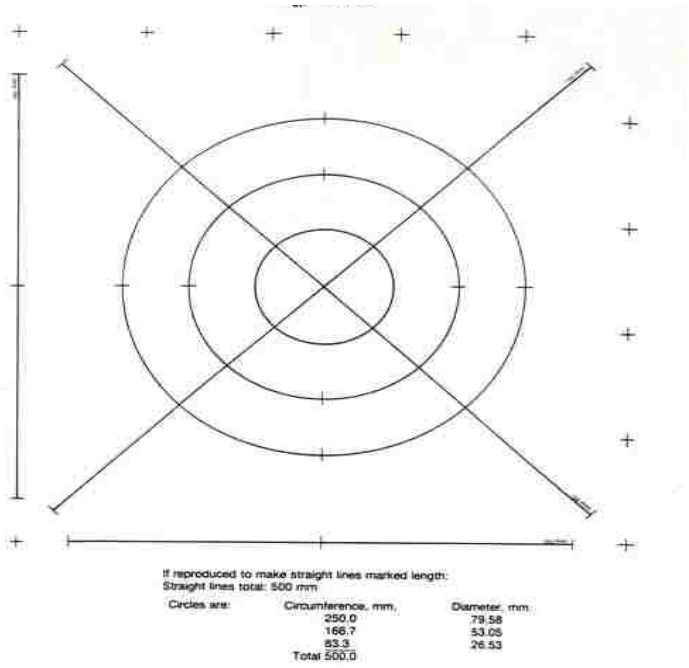

Figure 3-16 Template used in Grain Size Determination

3.7 Fractographic Evaluations

The extent and morphology of failure of the tested specimens were determined by a scanning electron microscope (SEM). Analysis of failure in metals and alloys involves identification of the type of failure. The test specimens were sectioned into 1/2 to 3/4 of an inch in length to accommodate them in the vacuum chamber of the SEM. Failures can usually be classified into two common types including ductile and brittle. Dimpled

microstructure is a characteristic of ductile failure. Brittle failure can be of two types; intergranular and transgranular. An intergranular brittle failure is characterized by crack propagation along the grain boundaries while a transgranular failure is characterized by crack propagation across the grains.

In SEM evaluations, electrons from a metal filament are collected and focused, just like light waves, into a narrow beam. The beam scans across the subject, synchronized with a spot on a computer screen. Electrons scattered from the subject are detected and can create a current, the strength of which makes the spot on the computer brighter or darker. This current can create a photograph-like image with an exceptional depth of field. Magnifications of several thousands are possible to achieve. A JEOL-5600 scanning electron microscope, shown in Figure 3-17, capable of resolution of up to 50 nm at magnifications of up to 100,000 times, was used in this study. The manual stage of this SEM unit can accommodate four 1 cm diameter samples or one sample with up to 3.2 cm diameter.

Figure 3-17 Scanning Electron Microscope

3.8 Transmission Electron Microscopy

TEM studies were conducted to characterize dislocations and precipitates of the tested creep specimens using a Tecnai G² F30 S-TWIN transmission electron microscope (Figure 3-18). This equipment operates at 300kV acceleration voltage that allows a point-to-point resolution of 0.2 nanometer. Magnifications up to 1,000,000 times can be achieved with this TEM. This system is fully loaded including HAADF (high angle annular dark field) detector, EDX (X-ray energy disperse spectrometry), and GIF (Gatan Image Filter). Multiple samples were prepared from each tested specimen to obtain valid TEM micrographs. The sample preparation technique is described in details in the next subsection.

Figure 3-18 Transmission Electron Microscope

3.8.1 TEM Sample Preparation

Sample preparation for the TEM study involves a state-of-art technique. To ensure electron transparency of the sample by the TEM method, the specimen thickness was maintained between 50-100 nanometers. This was achieved through a series of operations, as described below [79, 80].

- Initially, multiple circular disc-shaped samples were cut from the gage length of the tested creep specimens up to a thickness of 500–700μm, using a precision cutter in the Materials Performance Laboratory (MPL).
- Samples were then mechanically ground (Figure 3-19) to about 100–150 μm using a grinder in the TEM Sample Preparation Laboratory. This process involved two steps; rough-grinding and fine-polishing. Specimen thickness was monitored periodically during this process.
- The samples were then punched into 3mm diameter discs, using a disc puncher (Figure 3-20).
- Finally, electro-polishing was done to achieve the desired specimen thickness. A twin-jet TenuPol-5 electro polisher (Figure 3-21) was used for this purpose. This process involved removal of material from the sample surface as well as surface finish prior to TEM observation. The thinnest area was obtained around the perforation area. The composition of the electrolyte used for the process was 5% perchloric acid ($HClO_4$) in methanol (CH_3OH) with an applied potential of 50V, a pump flow rate of 12 and a temperature of -3°C [81]. Care was taken to control the flow of electrolyte to prevent the formation of anodic film that could cause etching of the specimen rather than polishing [80, 82].

Figure 3-19 Grinding Accessories

Figure 3-20 Disc Puncher

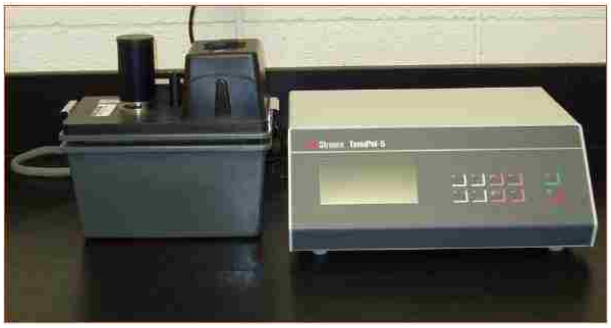

Figure 3-21 TenuPol-5 Electro-polisher

3.9 Phase Characterization

X-ray diffractometry (XRD) was used to characterize phase changes, if any, in tested creep specimens at ambient temperature and 950°C.The aim of this task was to provide a quality XRD pattern from polished alloy specimen to allow Rietveld Analysis without ball-milling of the metallic specimen. The XRD samples were harvested from creep test specimens and were ground and polished to a 3 micron finish. XRD pattern were taken using a PANalytical X'Pert Pro X-ray diffractometer with multiple silicon strip detector

(X'Celerator) and a Bruker-AXS Vario with primary Johansson Ge-monochromator and scintillation counting (Figure 3-22).

Figure 3-22 Panalytical X'PERT Pro XRD Spectrometer

CHAPTER 4

RESULTS

This chapter presents the overall data generated from different types of experimental work performed on Alloy 617. These data include the results of microstructural evaluation, crack-growth studies under both variable and constant load ratios (R), fracture toughness (J_{IC}) evaluation, stress-corrosion-cracking (SCC) evaluation in terms of stress-intensity-factor (K_{SCC}) under wedge-loaded conditions for variable exposure periods, characterization of time-dependent plastic deformation under sustained loading (creep) at different temperatures, determination of time to failure in stress rupture test under constant stress, characterization of defects (dislocations and voids) and precipitates by TEM, and finally, analyses of fracture morphology by SEM. These results are presented next in different sub-sections in a systematic manner.

4.1 Metallographic Evaluation

The metallurgical microstructure of the solution-annealed Alloy 617 is illustrated in Figure 4.1 in an etched condition. An evaluation of this optical micrograph revealed austenitic grains with annealing twins, which represent common microstructural characteristics of a Ni-based alloy. The annealing twins resulted from thermal treatment imparted to these materials. Carbide precipitates were also seen within the austenitic grains. The average grain diameter of this alloy, determined by the mean lineal intercept method [78, 83], was found to be 0.097 mm that corresponds to an ASTM grain size of 4 [84].

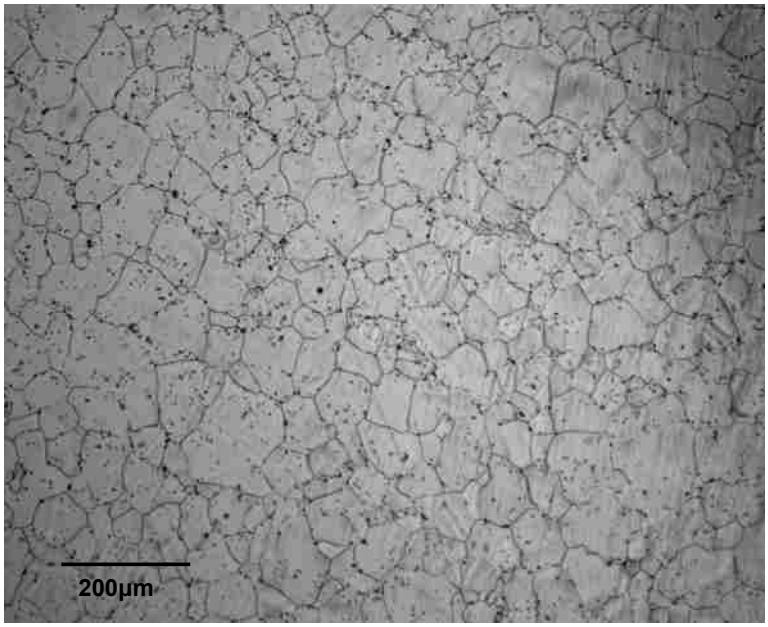

Figure 4-1 Optical Micrograph of Alloy 617, Kalling's Reagent

4.2 Results of Creep Testing

The tensile properties of Alloy 617 have previously been evaluated by another investigator [34] at MPL. Their properties include the yield strength (YS), ultimate tensile strength (UTS), percent elongation (%El) and percent reduction in area, which are given in Table 4-1.These date indicate that the magnitude of YS was gradually reduced within a temperature range of ambient to 700ºC. However, its value was enhanced at 800 and 900ºC to some extent, which has been attributed to the occurrence of yield strength anomaly [85]. The reduced ductility in terms of % El at 100ºC, as shown in Table 4-1, is associated with dynamic strain aging (DSA) that has been analyzed in detail by a previous investigator [86]. Creep testing was performed at 750, 850 and 950 ºC under applied stresses equivalent to 5, 10, 25 and 35% of the material's YS values at these temperatures.

Table 4-1 Average Tensile Properties versus Temperature

Temperature (°C)	YS ksi (MPa)	UTS Ksi (MPa)	%El	%RA
30	54 (371)	124 (856)	78.35	61.98
100	44 (306)	112 (774)	74.40	56.88
200	41 (283)	110 (761)	78.41	60.17
300	38 (265)	109 (752)	77.71	56.20
400	37 (254)	106 (728)	79.90	57.41
500	35 (244)	101 (697)	78.68	53.74
600	32 (221)	100 (688)	79.05	48.56
700	31 (211)	87 (598)	80.83	48.44
800	34 (234)	57 (392)	100.23	73.02
900	34 (237)	35 (240)	84.49	78.53
1000	19 (131)	19 (131)	88.23	72.07

The results of creep testing involving Alloy 617 are shown in Figure 4-2 to 4-5 in the form of % creep versus time as a function of temperature at applied stresses equivalent to 0.05YS (11,12 and 9MPa), 0.10YS (22, 24 and 18 MPa), 0.25YS (54, 59 and 46 MPa) and 0.35YS (78, 83 and 64 MPa). It is interesting to note that the magnitude of instantaneous elastic plus plastic strain resulting from the initial applied stress was enhanced at higher temperatures. The modulus of elasticity is known to decrease with increasing temperature, which could possibly account for the enhanced anelastic strain at higher temperatures. Further, the primary creep curve was relatively shorter at higher initial applied stresses, irrespective of the testing temperature. No creep deformation was observed in this alloy under an initial applied stress level of 11MPa at 750 ºC even after 1000 hours of loading, as shown in Figure 4-1. At 18 MPa-950 ºC [Figure. 4-2], this alloy exhibited a very short steady-state region, followed by an extended third stage. On the contrary, substantially longer secondary creep regions were observed in this alloy at 750 and 850 ^{o}C under initial applied stresses of 22 and 24 MPa, respectively [Figure. 4-3].

With increasing applied stress levels (0.25YS and 0.35YS) and temperature; Figures. [4-4, 4-5], the steady-state region became shorter and finally disappeared at 950 ^{o}C, showing only a steeper tertiary creep curve. Effect of applied stress [0.05-0.10YS] on anelastic strain was less significant. But at higher applied stresses and temperatures, the extent of elastic plus plastic strain was significantly higher.

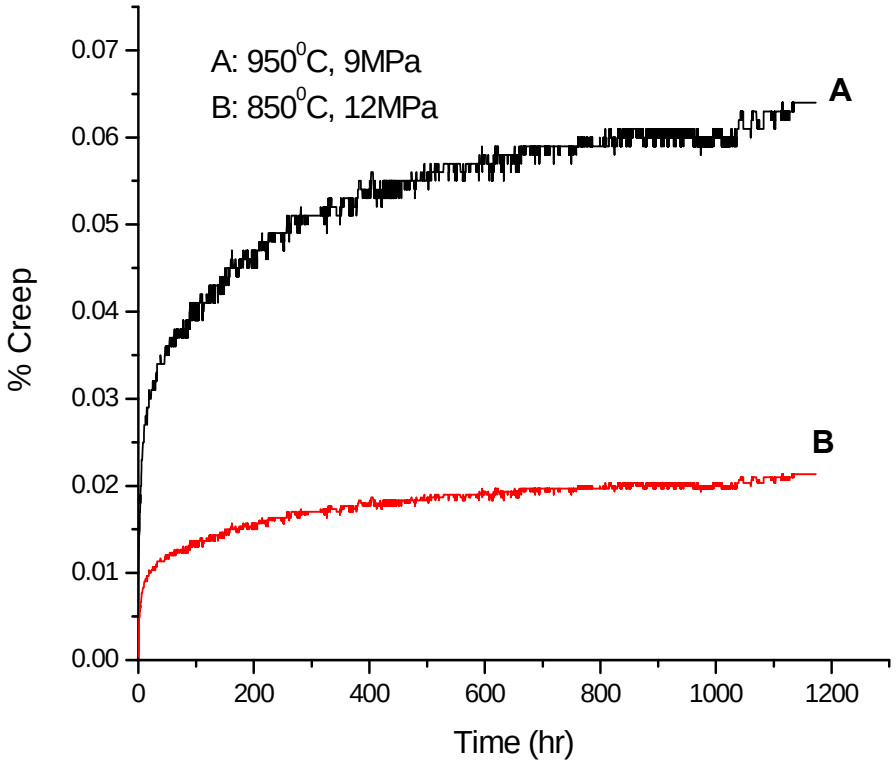

Figure 4-2 Creep Curves of Alloy 617 vs. Temp. and Applied Stress = 0.05YS

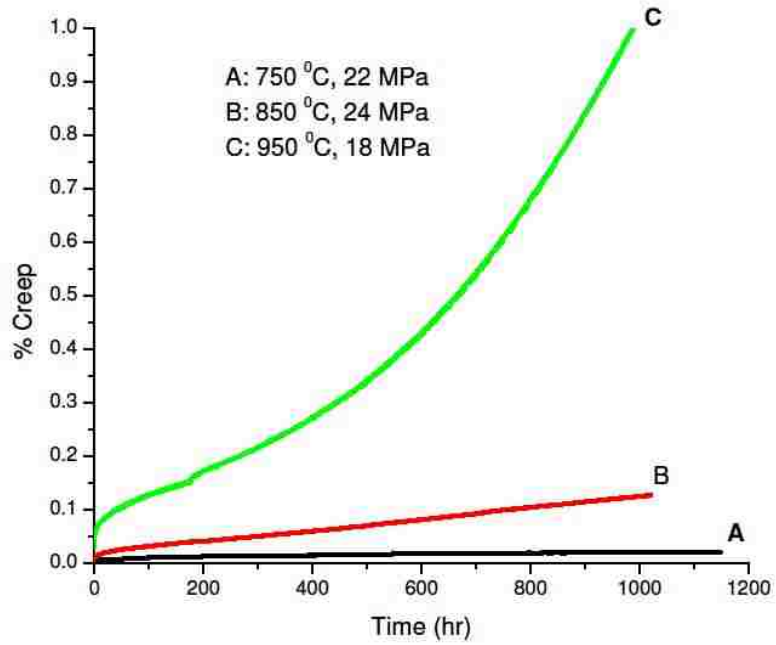

Figure 4-3 Creep Curves of Alloy 617 vs. Temp. and Applied Stress = 0.10YS

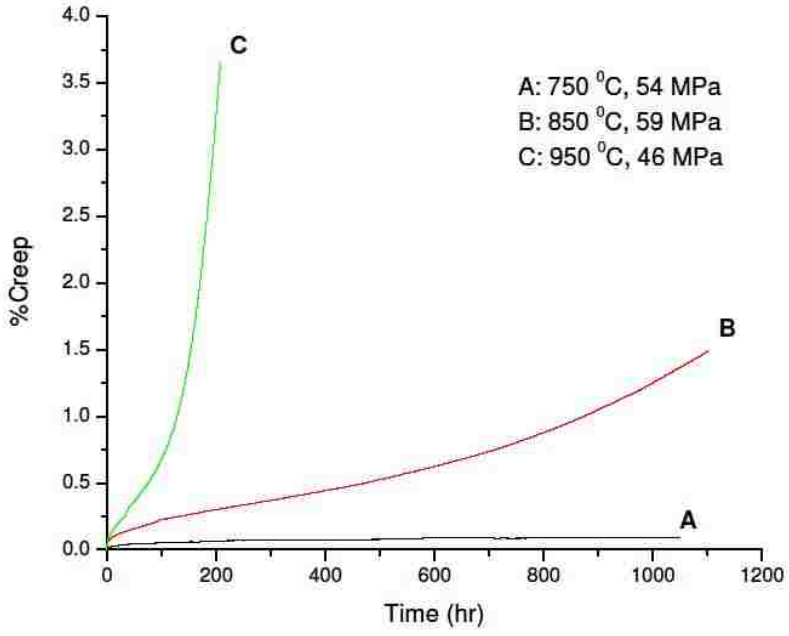

Figure 4-4 Creep Curves of Alloy 617 vs. Temp. and Applied Stress = 0.25YS

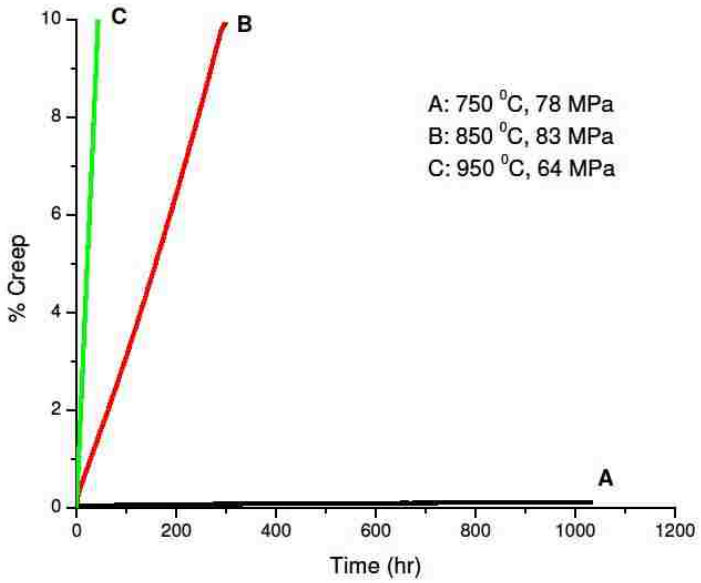

Figure 4-5 Creep Curves of Alloy 617 vs. Temp. and Applied Stress = 0.35YS

Assuming that a structural material must not undergo creep deformation exceeding 1% strain following 1000 hours of loading at different stress levels, it could be stated that Alloy 617 may not be capable of withstanding an operating temperature of 950 ^{o}C at applied stresses above 10% of its YS value. Data shown in Figure 4-4 indicate that Alloy 617 may not be able to sustain an operating temperature of 850 ^{o}C up to 1000 hours, when loaded to an applied stress of 59 MPa. Further, this alloy reached a tertiary stage almost immediately, when loaded to a higher stress level of 83 MPa at a similar temperature, as shown in Figure 4-5. Thus, the inference is strong that Alloy 617 may not be suitable for application under sustained loading both at 0.25YS and 0.35YS stress levels at 850 ^{o}C or higher. It is, however, interesting to note that this alloy was capable to sustain all three levels of stress (0.10YS, 0.25YS and 0.35YS) at 750 ^{o}C by virtue of its

prolonged and stable steady-state creep rates even beyond 1000 hours of testing [Figure 4-3, 4-4, 4-5].

The variation of creep rate with total strain, observed in a specimen tested under an applied stress of 6.67 ksi that represents a stress level equivalent to its 0.25YS value at 950ºC, is illustrated in Figure 4-6. These data indicate that extent of steady-state or secondary creep deformation was substantially lower than the deformation experienced in the tertiary region. Further, the magnitude of anelastic elongation was significantly higher at 850 and 950ºC, when Alloy 617 was loaded at 0.35YS values, as shown in Figure 4-7.

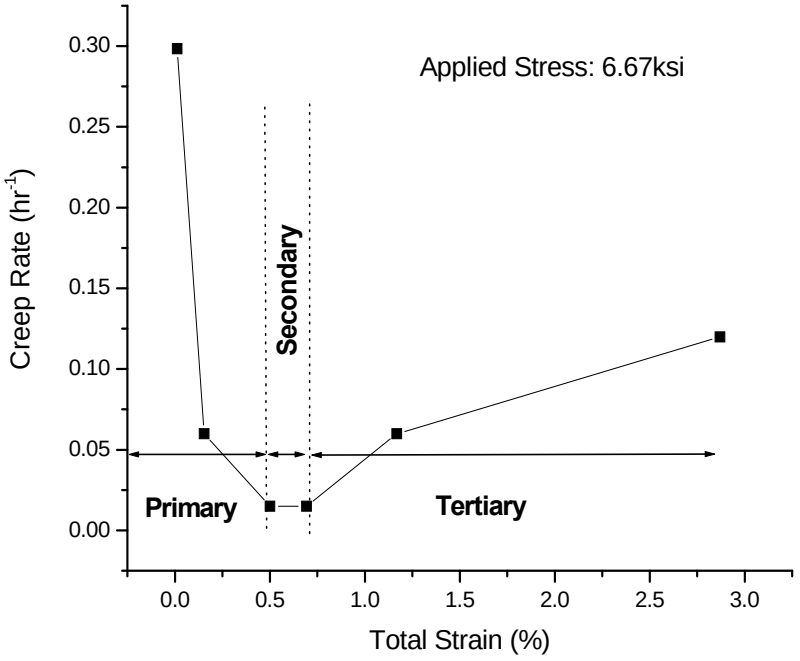

Figure 4-6 Creep Rate vs. Total Strain at 950 °C at 0.25YS

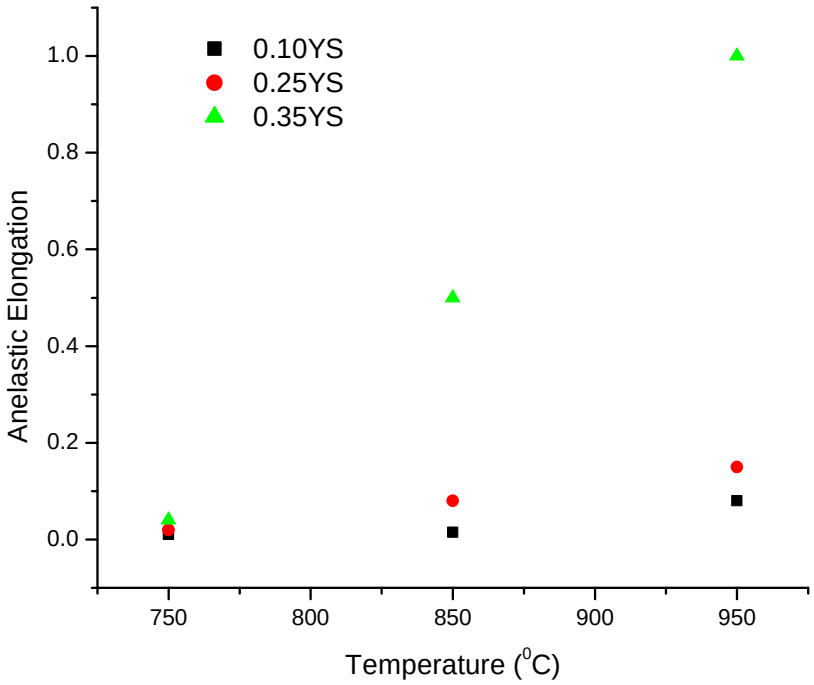

Figure 4-7 Anelastic Elongation vs. Temperature

The variation of total creep rate with the reciprocal of the testing temperature is illustrated in Figure 4-8, as a function of the applied stress level. A synergistic effect of temperature and stress is clearly evident, showing a significantly higher creep deformation under 0.25YS and 0.35YS stress levels at 850 and 950ºC. The variation of steady-state creep rate (ϵ_s^o) with applied stress level at three tested temperatures is shown in Fig. 4-9. It is obvious that the normal temperature-compensated power law did not apply to Alloy 617, since the slope of the straight line, obtained at 750ºC, did not match with that seen for this alloy at 850 and 950 ºC. Such difference could be attributed to the changes in metallurgical microstructure and the occurrence of yield strength anomaly (YSA) at elevated temperatures. A combination of precipitates, pinned dislocations, pile-

up of dislocations in and around the grain boundaries, formation of precipitates around subgrains and grain boundaries causing strengthening of the material leading to the YSA phenomenon in these temperature regime.

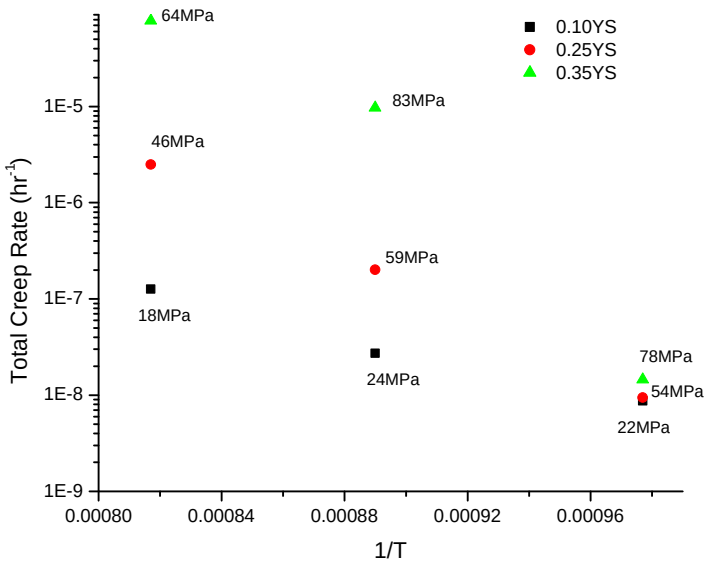

Figure 4-8 Total Creep Rate vs. 1/T

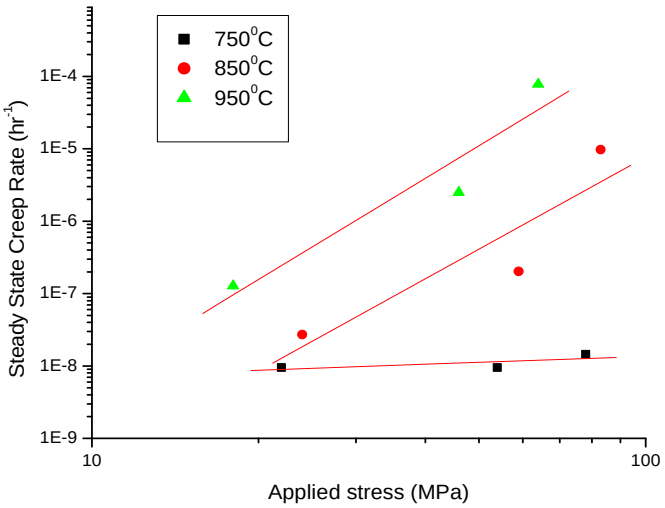

Figure 4-9 Steady-State Creep Rate vs. Applied Stress

4.2.1 Activation Energy Evaluation

Figure 4-10 illustrates a plot of ln ϵ_s^o versus 1/T for specimens tested under applied stress levels of 0.25YS values, showing a linear relationship. A similar relationship was also observed when testing was performed at applied stresses equivalent to 0.10YS and 0.35YS values. The magnitude of activation energy (Q) was determined from the slope of these lines. The calculated values of Q are given in Table 4-2 as functions of applied stress and testing temperature. An average Q value of 351 kJ/mole.K was obtained by this method, which is not too different from the average Q value of 290 kJ/mole.K determined by using equations 3-1 and 3-2. Literature data [87, 88] suggest that the Q value for creep deformation of Ni-base alloy may fall within a wide range of 351 to 3773 kJ/mole.K. Thus, the average Q value, determined in the present investigation, is very close to the lower bound of the literature data.

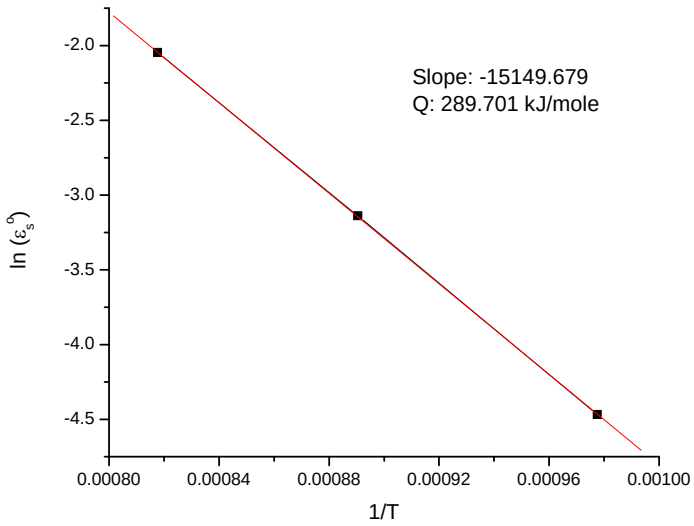

Figure 4-10 ln ($\dot{\varepsilon}_s$) vs. 1/T

Table 4-2 Calculated Values of Q and n

Stress level, MPa	Temperature, K			Q, kJ/mole
	1033	1123	1223	
0.10YS	22	24	18	132
0.25YS	54	59	46	314
0.35YS	78	83	64	606

4.3 Crack-Growth-Rate Evaluation

4.3.1 Crack-Growth-Rate versus Stress Intensity Factor Range

The superimposed crack-growth-rate (CGR~da/dN) versus stress intensity factor range (ΔK) plots for Alloy 617, generated under R values of 0.1, 0.2, and 0.3 within a temperature range of ambient to 300 °C, are shown in Figures 4-11, 4-12, and 4-13. It is obvious from these results that, irrespective of the R value, the CGR in terms of da/dN were appreciably higher at 100 °C, compared to that at ambient temperature. At 300 °C, the magnitude of da/dN was also slightly enhanced, suggesting that the CGR was further increased at a higher temperature for all three R values. However, the rate of increase in crack growth rate was reduced at 300 °C compared to that at 100 °C, suggesting that the crack-tip might have been blunted at temperatures above 100ºC.

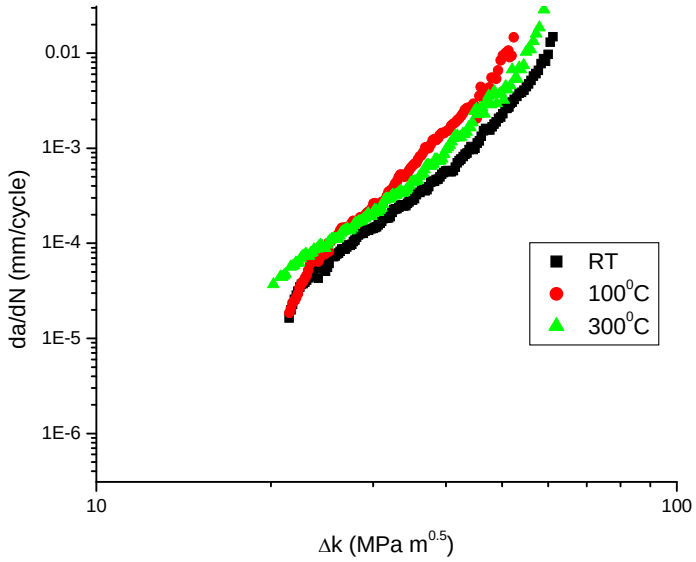

Figure 4-11 da/dN vs. ΔK at R = 0.1

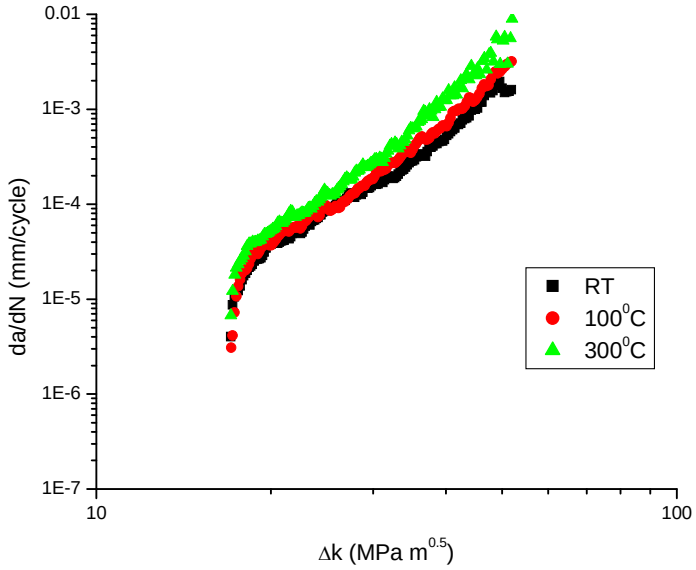

Figure 4-12 da/dN vs. ΔK at R = 0.2

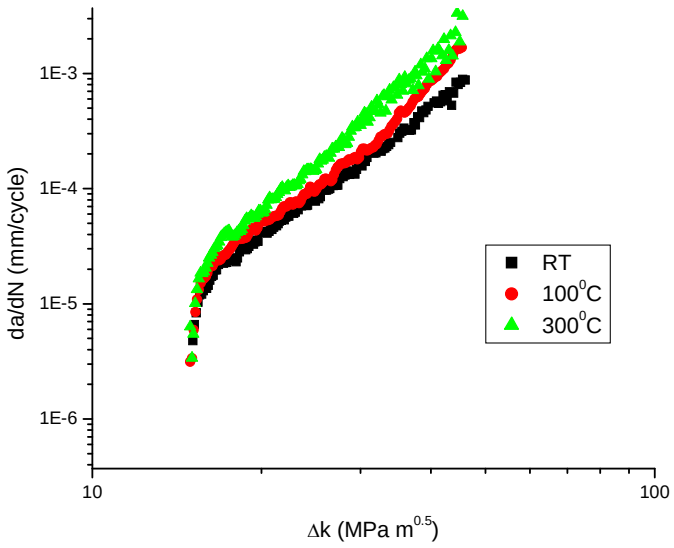

Figure 4-13 da/dN vs. ΔK at R = 0.3

4.3.2 Crack Length versus Number of Cycles

The superimposed plots of crack length (a) versus number of cycles (N), generated under an R value of 0.1 in the temperature range of ambient to 300 °C, are shown in Figure 4-14. These data indicate that the number of cycles (N) needed for comparable crack extension was significantly reduced with increasing temperature. Thus, the magnitude of da/dN was higher at elevated temperatures, when the R value was maintained at 0.1. A similar trend in 'a' versus 'N' plot was observed with this alloy at R values of 0.2 and 0.3, as illustrated in Figures 4-15 and 4-16, respectively. Variations of 'a' with 'N' at room temperature, 100 and 300 °C, at three different R values, are shown in Figures 4-17, 4-18 and 4-19, respectively. These data indicate that the magnitude of N needed to develop a comparable crack length reached a minimum value at an R value of 0.1, irrespective of the testing temperature. However, even at this R value (0.1), the lowest value of N to cause a similar level of cracking resulted at 300 °C, suggesting a

combined detrimental effect of both higher temperature and lower load ratio in enhancing the cracking tendency of Alloy 617. A lowest value of N at an R value of 0.1 could be attributed to a maximum loading constraint resulting from the highest load range (ΔP) of 4.5 kN.

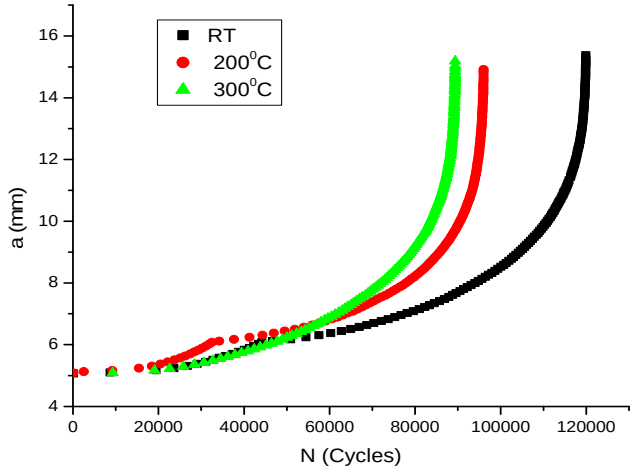

Figure 4-14 Crack Length (a) vs. N at R = 0.1

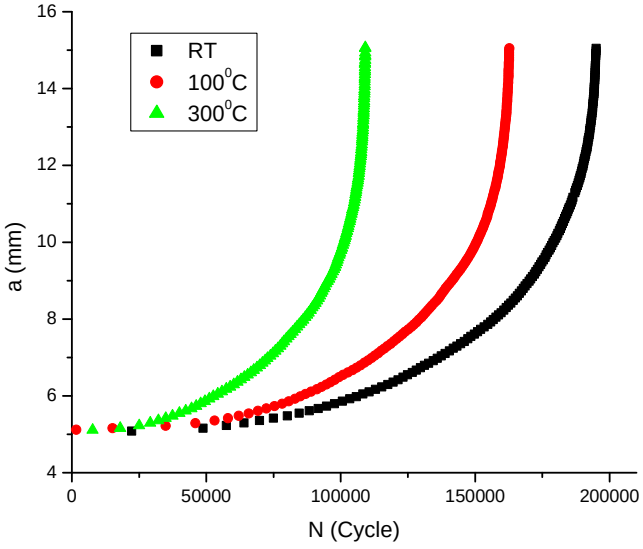

Figure 4-15 Crack Length (a) vs. N at R = 0.2

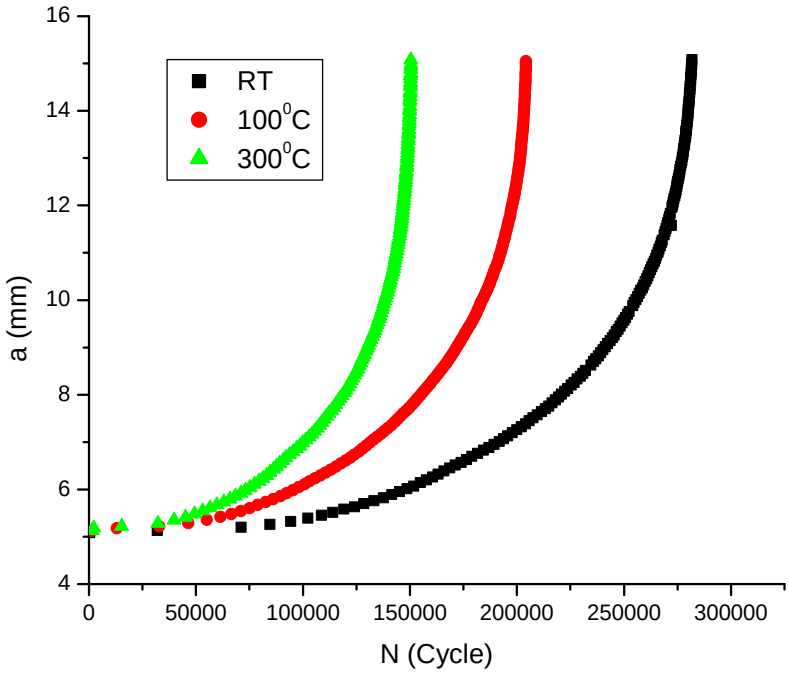

Figure 4-16 Crack Length (a) vs. N at R = 0.3

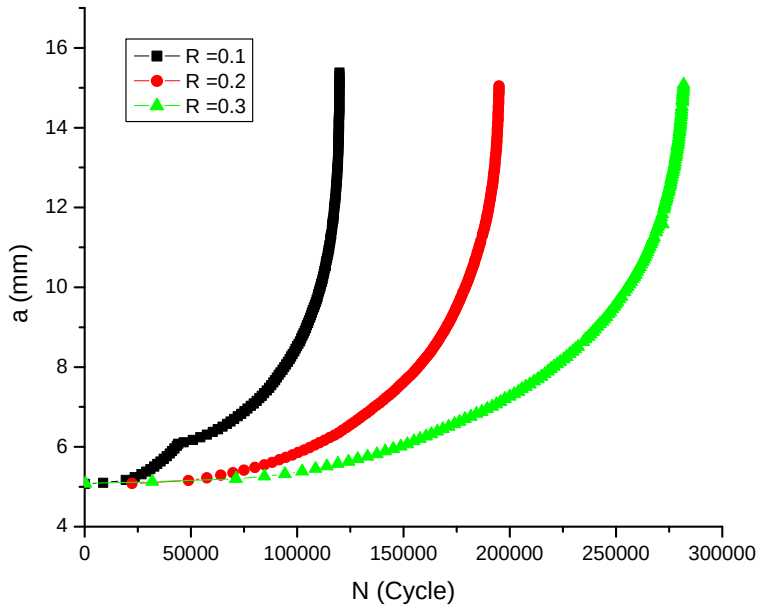

Figure 4-17 Crack Length (a) vs. N at Room Temperature

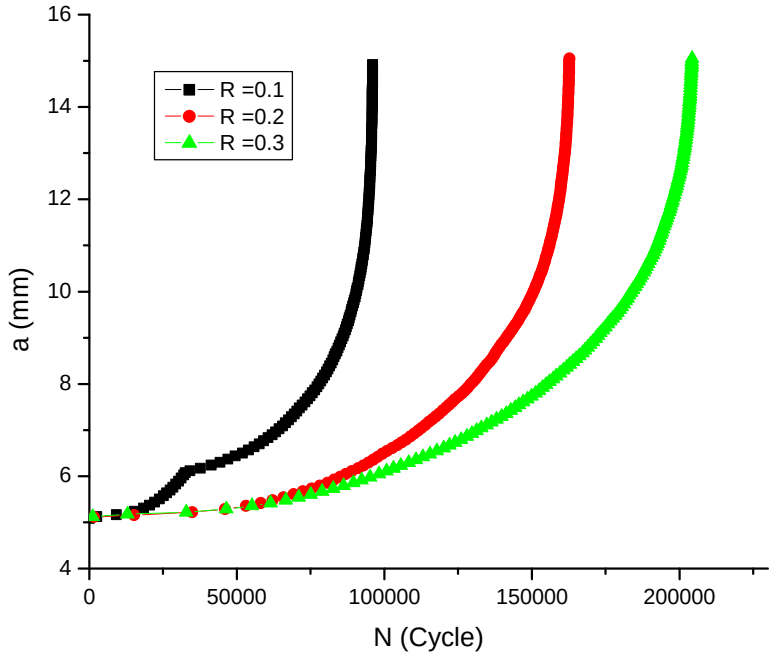

Figure 4-18 Crack Length (a) vs. N at 100 °C

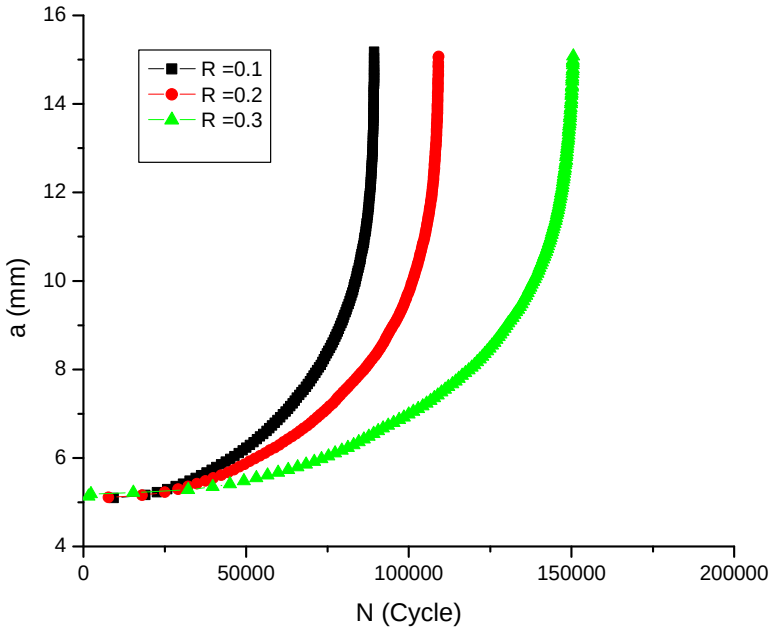

Figure 4-19 Crack Length (a) vs. N at 300 °C

4.3.3 N versus Temperature and R

The variation of N with temperature as a function of R (0.1, 0.2 and 0.3) is illustrated in Figure 4-20. Once again, these data indicate that the number of cycles needed for comparable crack extension was significantly reduced at 100 °C compared to that at room temperature, irrespective of the R value. Interestingly, the magnitude of N was not significantly reduced at a higher temperature (300 °C), suggesting that the crack might have reached a critical length within a temperature range of 100-300 ^{o}C, especially under a load ratio of 0.1. The variation of N with R at different temperatures is illustrated in Figure 4-21, once again confirming the detrimental effect of the lowest R value and highest testing temperature in enhancing the cracking susceptibility of Alloy 617 by resulting in a reduced number of cycles.

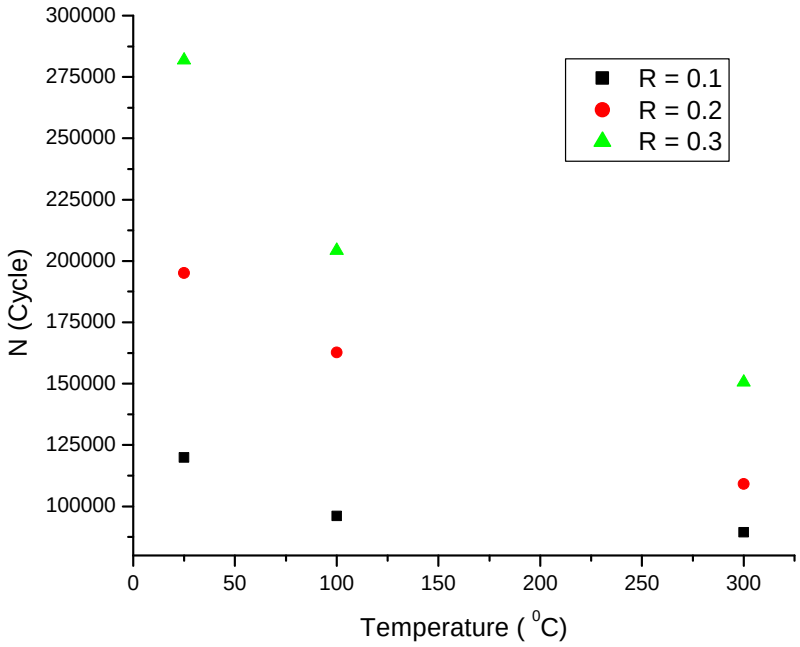

Figure 4-20 N vs. Temperature

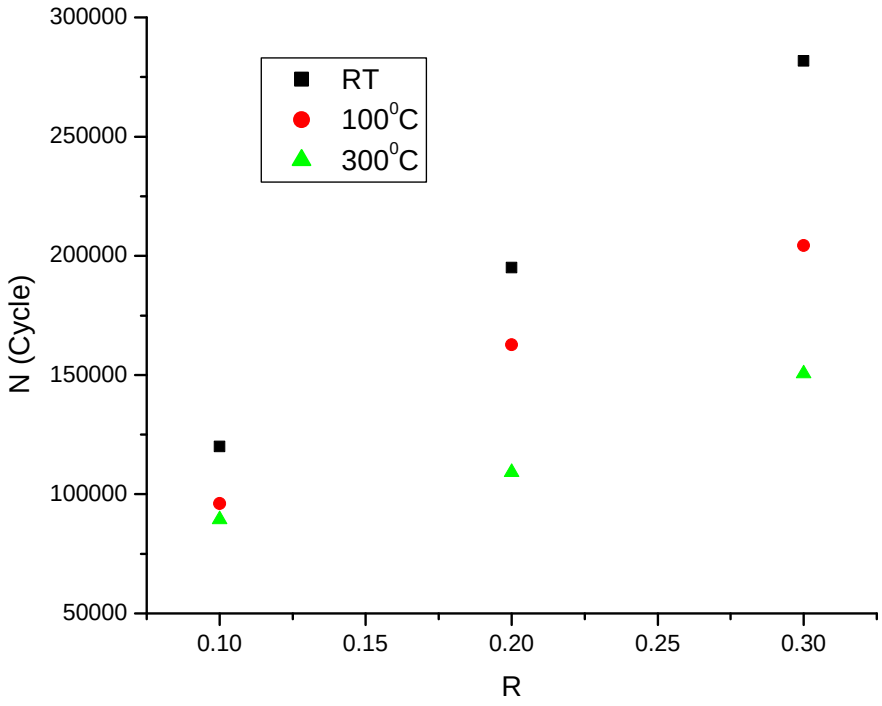

Figure 4-21 N vs. R

4.3.4 Number of Cycles to Failure versus Temperature and R

Efforts were made to calculate the number of cycles to failure (N_f) at different temperatures under all three tested R values. The magnitude of N_f was calculated using Equation 3-9, derived from the Paris equation. The variations of N_f with temperature and R are illustrated in Figures 4-22 and 4-23, respectively. These data, once again, confirm the detrimental effects of higher temperature and lower R value on crack extension of Alloy 617 by showing reduced N_f values.

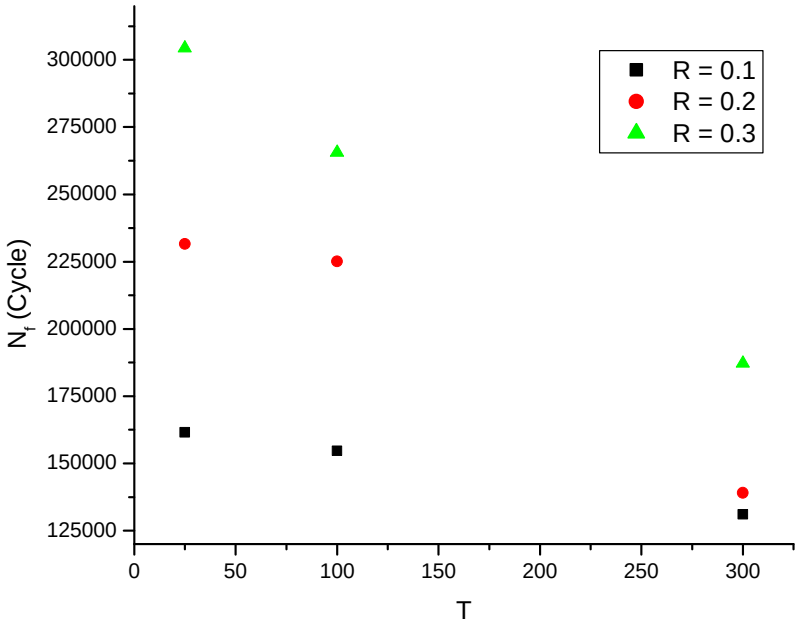

Figure 4-22 N_f vs. Temperature

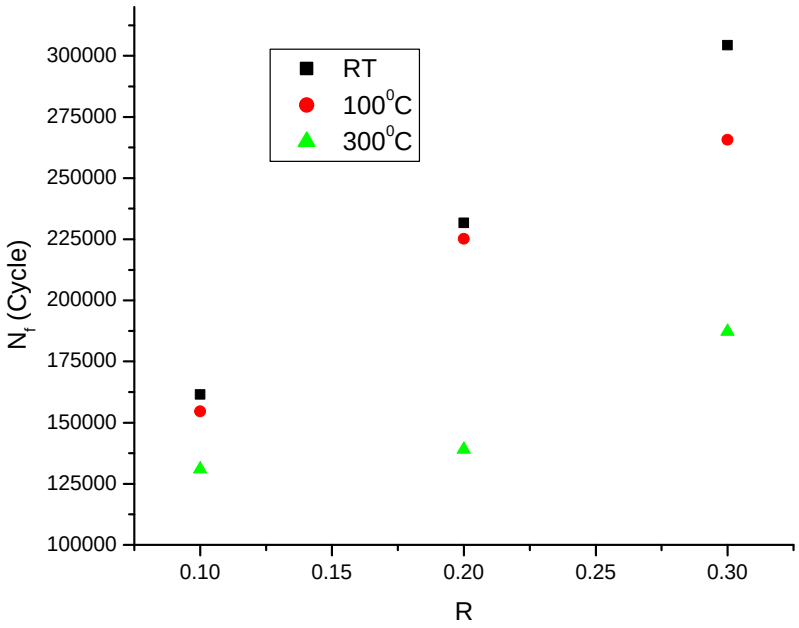

Figure 4-23 N_f vs. R

4.3.5 Determination of Slope and Crack-Growth Coefficient

The magnitudes of the slope (m) and crack-growth coefficient or intercept (A) of the linear portion of the da/dN versus ΔK plot (using Paris Equation) at different temperatures and R values are given in Tables 4-3 and 4-4, respectively. These data suggest that, irrespective of the testing temperature and R value, there were no significant variation in m value (i.e., 3.63-4.82). However, the magnitude of 'A' was gradually increased with an increase in temperature from ambient to 300 °C at the R value of 0.1, and an opposite trend was observed for the R values of 0.2 and 0.3. Also, the magnitude of A was gradually increased at higher R values when the temperature was kept constant.

Table 4-3 Calculated m Values from da/dN vs. ΔK Plots

Temperature (°C)	m		
	R = 0.1	R = 0.2	R = 0.3
Ambient	4.19	3.73	3.63
100	4.21	4.31	3.71
300	4.82	4.25	4.07

Table 4-4 Calculated A Values from da/dN vs. ΔK Plots

Temperature (°C)	A ($\times 10^{-13}$ MPa$\sqrt{m}$)		
	R = 0.1	R = 0.2	R = 0.3
Ambient	0.65	5.01	7.19
100	0.89	2.61	4.71
300	1.13	2.52	4.31

4.3.6 Determination of Threshold Stress Intensity Factor Ranges

The variations of threshold stress intensity factor range (ΔK_{th}) with temperature at three different R values are given in Table 4-5. These data indicate insignificant variation of ΔK_{th} value with temperature at R values of 0.2 and 0.3. However, an anomalous behavior was observed at an R value of 0.1. Nevertheless, the magnitude of ΔK_{th} was gradually reduced with increasing R value irrespective of the testing temperature. Such results can be justified in terms of relatively higher loading constraint due to a greater load range (ΔP) at lower R values, thus causing relatively higher cracking tendency.

Table 4-5 Average ΔK_{th} Value vs. Temperature and R

Temperature (°C)	ΔK_{th} (MPa$\sqrt{m}$)		
	R = 0.1	R = 0.2	R = 0.3
Room Temperature	22.31	18.56	16.43
100	23.11	17.91	16.05
300	18.03	17.56	16.91

4.3.7 Determination of Activation Energy

The calculated values of activation energy (Q) for crack propagation of Alloy 617 within a temperature range of ambient to 300 °C at all three tested R values are given in Table 4-6. The Q values were ranged between 139 to 151J/mole. While no literature data exist as to the Q value for crack propagation of this alloy, the Q values estimated in this study seems to be close to that of a similar type of Ni-based alloy [62]. It is, however, interesting to note that the magnitude Q was somewhat enhanced at higher R values,

suggesting that greater driving forces were necessary for crack extension at higher R values due to lesser loading constraint. Plot of ln (A) versus 1/T is shown in Figures 4-24 at an R value of 0.1, from which the Q value was calculated using the slope of the resultant line.

Table 4-6 Calculated Q Values vs. R

R	Average Q (J/mole) at a particular R Value
0.1	139.15
0.2	142.60
0.3	151.42

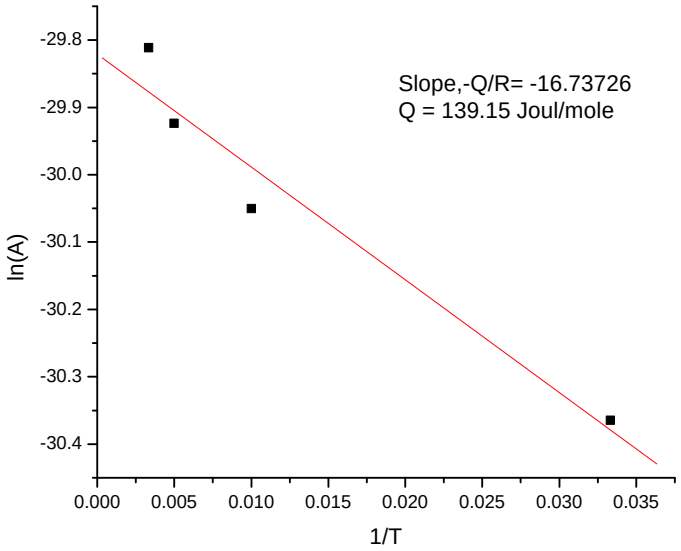

Figure 4-24 ln (A) vs. 1/T at R = 0.1

4.3.8 Results of Constant K Testing

The results of CGR testing, performed under different ΔK values at an R value of 0.1 at ambient temperature, are illustrated in Figure 4-25 in the form of crack-length (a) versus number of cycles (N) plot. These data reveal a linear relationship for all three ΔK values. The slopes of these linear plots (da/dN) were calculated and are shown in Table 4-7 corresponding to different ΔK values. The variation of the number of cycles (N) with the ΔK values for comparable crack growth (15 mm) is also shown in Table 4-7. These data indicate that, as the magnitude of ΔK was increased, CGR in terms of da/dN was also increased by virtue of the reduced N value arising from a greater loading constraint. The plots of crack length (a) versus load (P) are also shown in Figure 4-26. The P value was gradually decreased with increasing 'a' for all three sets of K values. This is due to a fact that, in a constant-K test, the only variables are 'a' and P. So if 'a' increases, P decreases [$K = \sigma\sqrt{(\pi a)}\times\alpha$, where σ = stress = P/area, and α = geometric factor (constant)].

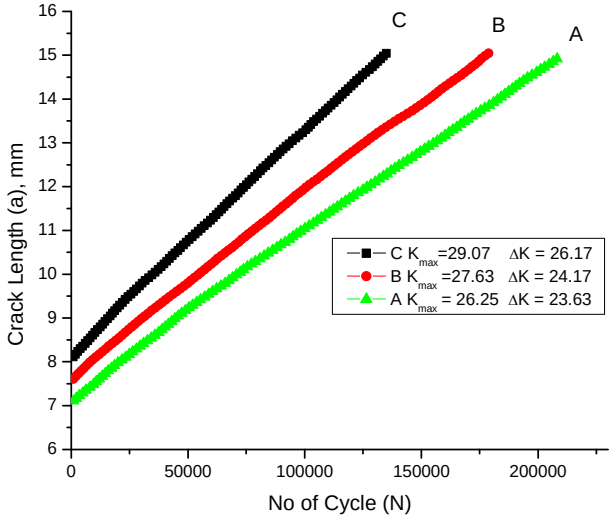

Figure 4-25 Crack Length (a) vs. N

Table 4-7 da/dN and N Values vs. ΔK

ΔK (MPa√m)	Average da/dN (mm/cycle) $\times 10^{-5}$	N (Cycles)
23.63	3.69	338704
24.17	4.13	309207
26.17	5.10	282419

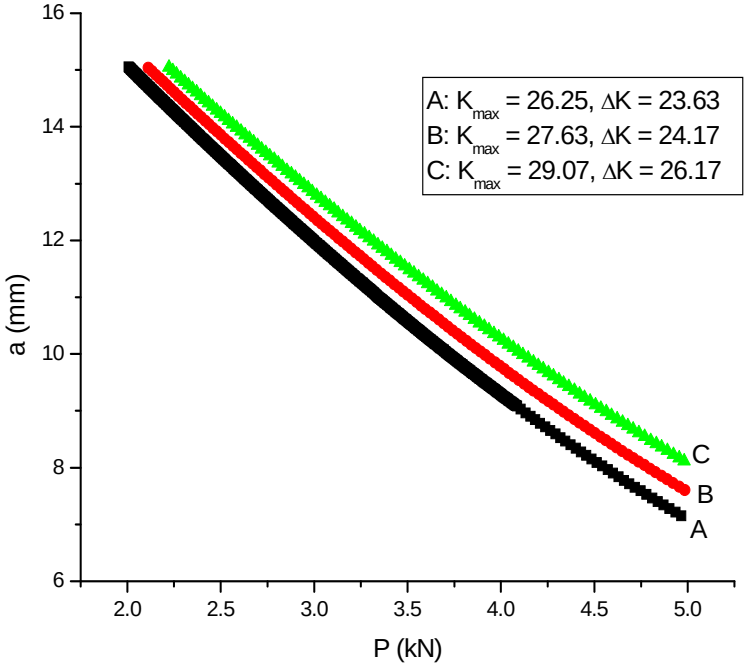

Figure 4-26 a vs. P

4.4 Results of Fracture Toughness Testing

4.4.1 Determination of J_{IC}

The measured conditional fracture toughness (J_Q) values determined from J_{IC} testing satisfied the validity criteria set by the ASTM Designation E 813-1989 [39]. The average J_{IC} values of Alloy 617 tested at room temperature, 100, 200 and 500 °C are given in Table 4-8. Also, the variation of J_{IC} with temperature is illustrated in Figure 4-27. These data indicate that the J_{IC} value was not appreciably reduced with increasing temperature, the reduction being more pronounced as the temperature was increased from ambient to 100 to 200 °C. Between 200 and 500 °C, the change in J_{IC} was not significant, confirming observations made by other investigators [89] as to the role of higher temperature on J_{IC}. A load versus load-line-displacement (LLD) plot and a J-Integral versus Δa plot, used in J_{IC} calculation, are illustrated in Figures 4-28 and 4-29, respectively.

Table 4-8 J_{IC} vs. Temperature

Temperature (°C)	Average J_{IC} (KJ/m^2)
Ambient Temperature	118.61
100	114.10
200	109.88
500	109.10

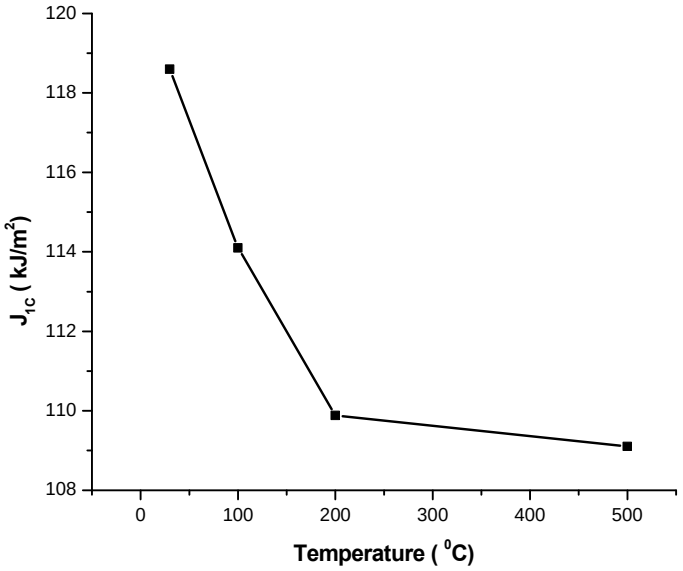

Figure 4-27 J_{IC} vs. Temperature

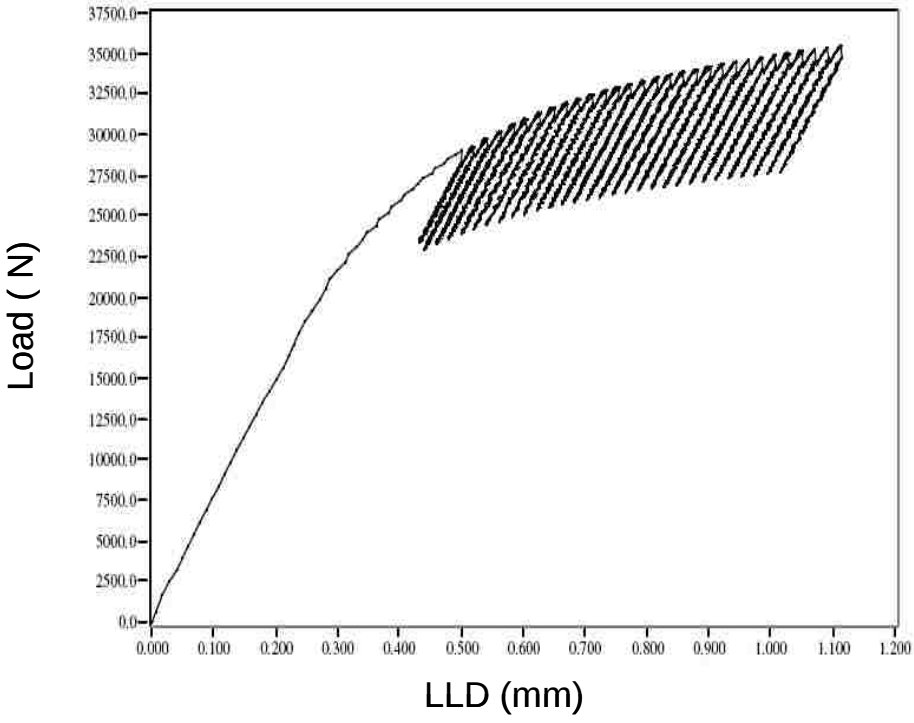

Figure 4-28 Load vs. LLD at Ambient Temperature

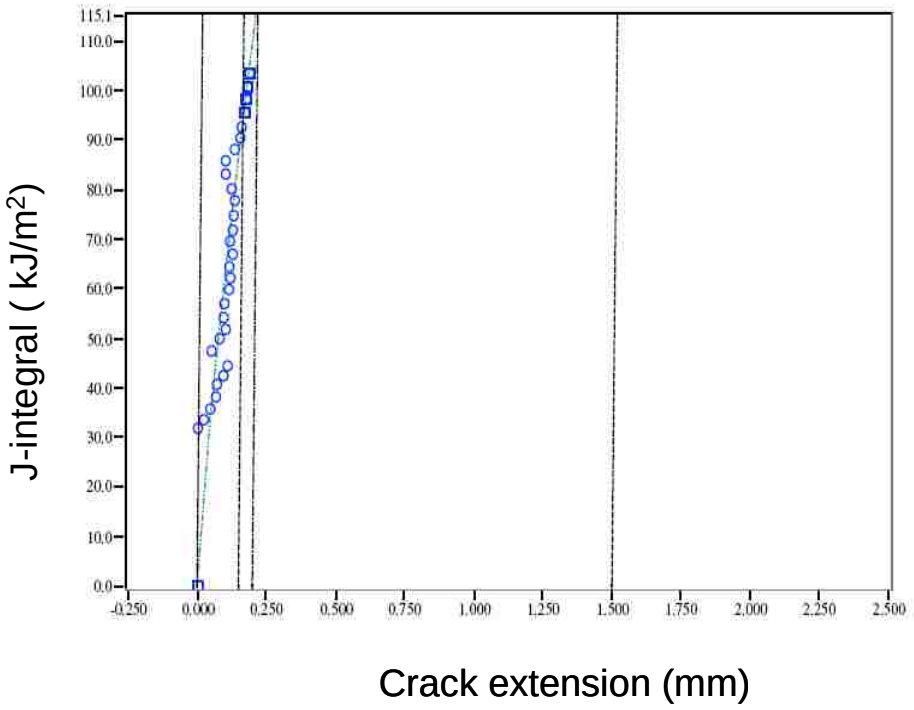

Figure 4-29 J-Integral vs. Δa at Ambient Temperature

4.4.2 Equivalent K_{IC} and CTOD Values

The average calculated values of equivalent K_{IC} (determined by using Equation 3-20) and CTOD (δ -determined by using Equation 3-21) at different temperatures are given in Table 4-9. No significant variations in the K_{IC} and δ values were noted at temperatures ranging from 100 to 500 ºC. However, the fracture toughness of Alloy 617, in terms of all these parameters (J_{IC}, K_{IC} and δ), as determined in this study, was significantly higher than those cited for other engineering materials [61]. Nevertheless, the magnitude of δ was close to a range 0.1 to 0.2 that represents fracture toughness values for an adequately tough material [90].

Table 4-9 K_{IC} and δ Values vs. Temperature

Temperature (°C)	Average K_{IC} (MPa√m)	Average δ (mm)
Room Temperature	163	0.175
100	160	0.204
200	157	0.213
500	156	0.245

4.4.3 Tearing Modulus Values

From the results of the J-integral R-curve for Alloy 617, a dimensionless parameter, known as the tearing modulus (T), has been calculated. Value of dJ/da was determined from the J versus 'a' plot, as shown in the Figure 4-30. The resistance of a material to tearing instability is usually expressed as the tearing modulus, which depends on the slope of J-integral R-curve and other well-known properties including the flow stress and elastic modulus (E). The variation of tearing modulus is shown in Figure 4-28 on a semi-logarithmic scale, as a function of the testing temperature (K).

The data shown in Figure 4-31 indicate that the tearing modulus (T) remained almost constant at temperatures ranging from ambient to 200ºC. However, there was a slight increase in the T value as the temperature was increased from 200 to 500ºC. The magnitude of T was found to be well above 100, implying that Alloy 617 should have a significant resistance to tearing within the temperature regime tested in this study.

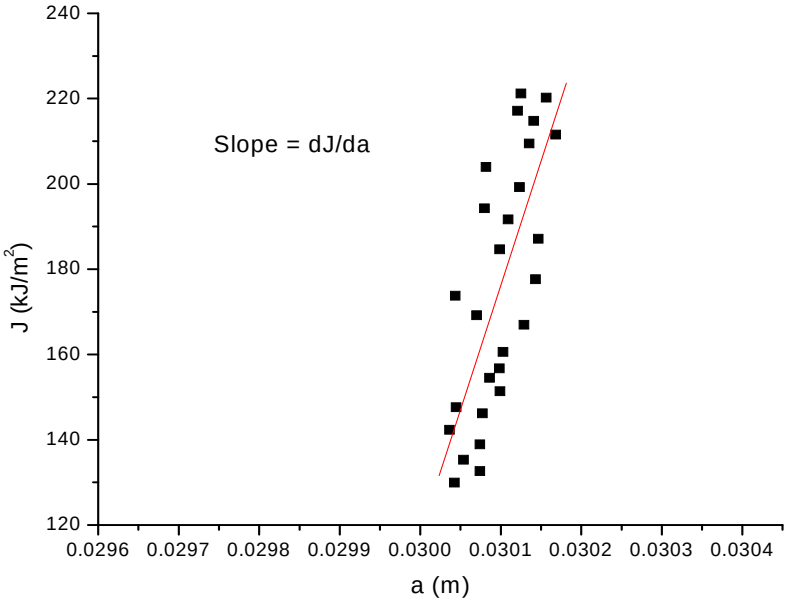

Figure 4-30 J vs. Crack Length (a) at Room Temperature

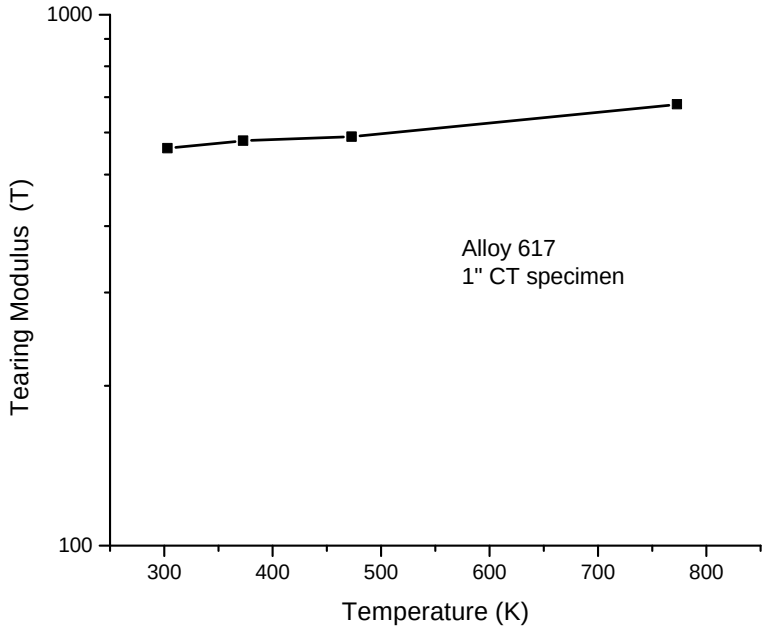

Figure 4-31 Tearing Modulus vs. Temperature

4.5 Results of SCC Testing

The result of SCC testing using pre-cracked and wedge-loaded DCB specimens of Alloy 617, exposed to a 100 ºC acidic solution for durations of 2, 4 and 8 months, are given in Table 4-10. Average crack extensions (Δa) of 0.45, 0.70 and 1.20 mm were observed in this alloy, following exposures of 2, 4 and 8 months, respectively. Corresponding to these crack extensions, the tested specimens showed average reduction in stress intensity factor ($\Delta K = K_I - K_f$) values of 5.85, 11.49 and 20.89 MPa√m, respectively.

It is well known that DCB method of SCC evaluation constitutes a constant displacement technique, in which the gap between the two arms of the specimen is kept constant by inserting wedges of selected thickness. Thus, as the crack progresses, the load imparted by the wedge gradually drops until a threshold load is reached, at which the crack cannot propagate any further. The results obtained from this study indicate that the DCB specimens experienced continuous growth of crack length up to an exposure period of 8 months, suggesting that a threshold stress intensity factor for SCC (K_{ISCC}) might not have yet been reached. In addition, the reduction in wedge load (ΔP) was more pronounced for specimens loaded to higher K_I values, as shown in Table 4-10 and Figure 4-32. The average crack growth rate (CGR), corresponding to the exposure periods of 2, 4 and 8 months, respectively is shown in Figure 4-33. As anticipated, the average CGR was substantially reduced between 2 and 4 months due to a significant reduction in the wedge load. The overall data suggest that K_{ISCC} value could possibly be achieved, should the specimens be tested in an identical solution for durations longer than 8-month. An effort was made to analyze the characteristics of broken DCB specimens along the

fractured faces by using SEM. Fractographic evaluation revealed three distinct regions, showing the characteristics of fatigue failure, environmental cracking (SCC), and tensile-overload fracture, as illustrated in Figures. 4-34 and 4-35. Pre-cracking of the DCB specimen in air at the notched area by cyclic loading was characterized by striations. The fractured face, immediately following the pre-cracked area, was the result of transgranular brittle or quasi-cleavage failure resulting from the exposure of the DCB specimens to the 100ºC acidic solution. Similar types of stress-assisted failure have been reported elsewhere [91] or Ni-base alloys tested in a hydrogen-containing environment as well as in methanol. The tensile-overload fracture of the DCB specimen, upon completion of testing and removal of wedge, was characterized by dimpled microstructure indicating ductile failure. A comparison of the pH of the solutions before, during and after testing indicated that the pH value ranged between 1.06 and 2.81, which still represent a strong acidic solution. Further, the amount of corrosion product was very negligible for all exposure periods.

Table 4-10 Results of DCB Testing

Specimen No.	P_i, N	ΔP, N	Δa, mm	Ki, MPa√m	K_f, MPa√m	ΔK, MPa√m	T, hours	Δa/T, mm/hr
1	2202	299	0.40	29.96	26.15	3.80	1440	2.78E-04
2	3105	817	0.56	42.25	31.57	10.68	2880	1.94E-04
3	2895	1488	1.05	39.39	19.64	19.74	5760	1.82E-04
4	3298	614	0.49	44.87	36.97	7.90	1440	3.40E-04
5	3485	958	0.85	47.42	35.11	12.30	2880	2.95E-04
6	3388	1678	1.35	46.10	24.05	22.04	5760	2.34E-04

where

P_i = Initial load, N

P_f = Final load, N

ΔP = Reduction in Load, N

a_i = Initial crack length, mm

a_f = Final crack length, mm

Δa = Crack extension, mm

K_1 = Initial stress intensity factor, MPa$\sqrt{m}$

K_f = Final stress intensity factor after exposure, MPa$\sqrt{m}$

ΔK = Difference in stress intensity factor, MPa$\sqrt{m}$

CGR = Crack-growth-rate, mm/hr

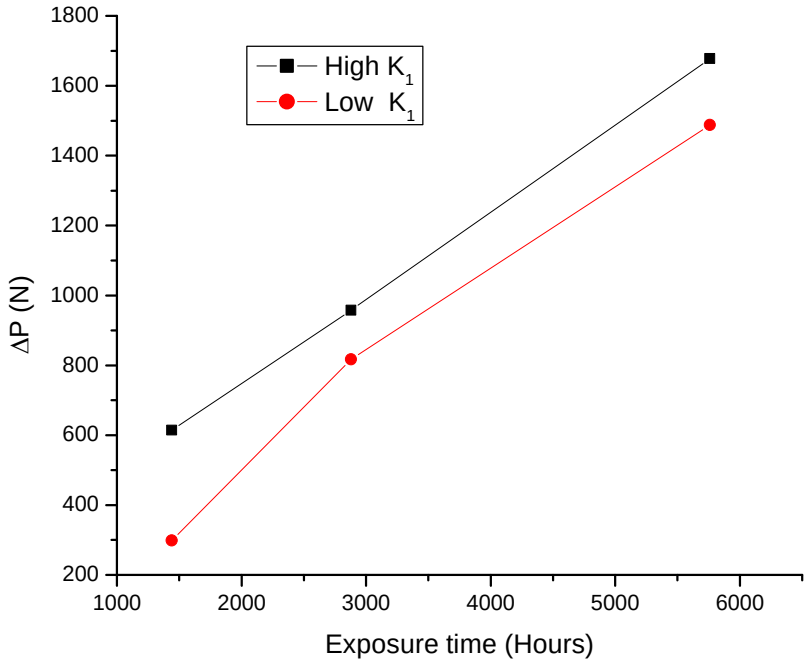

Figure 4-32 ΔP vs. Exposure time

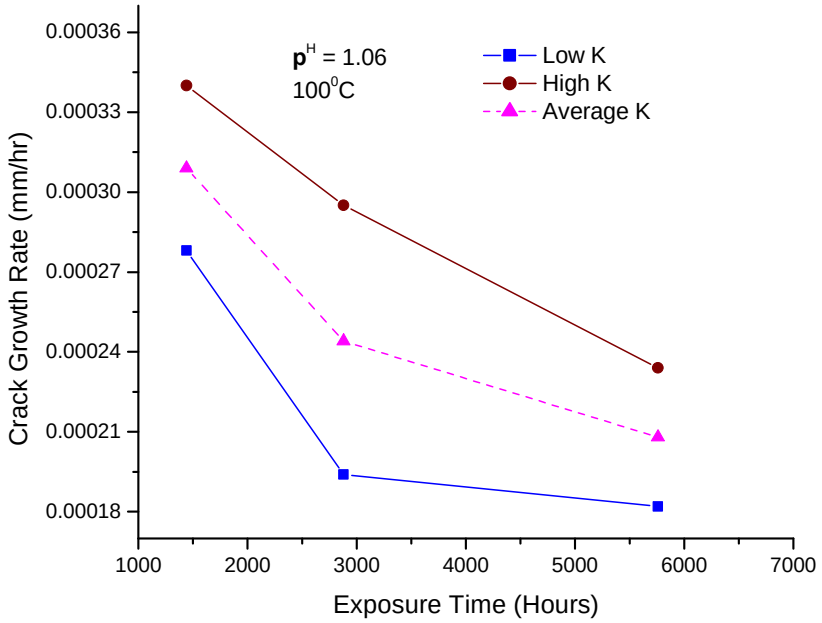

Figure 4-33 CGR vs. Exposure time

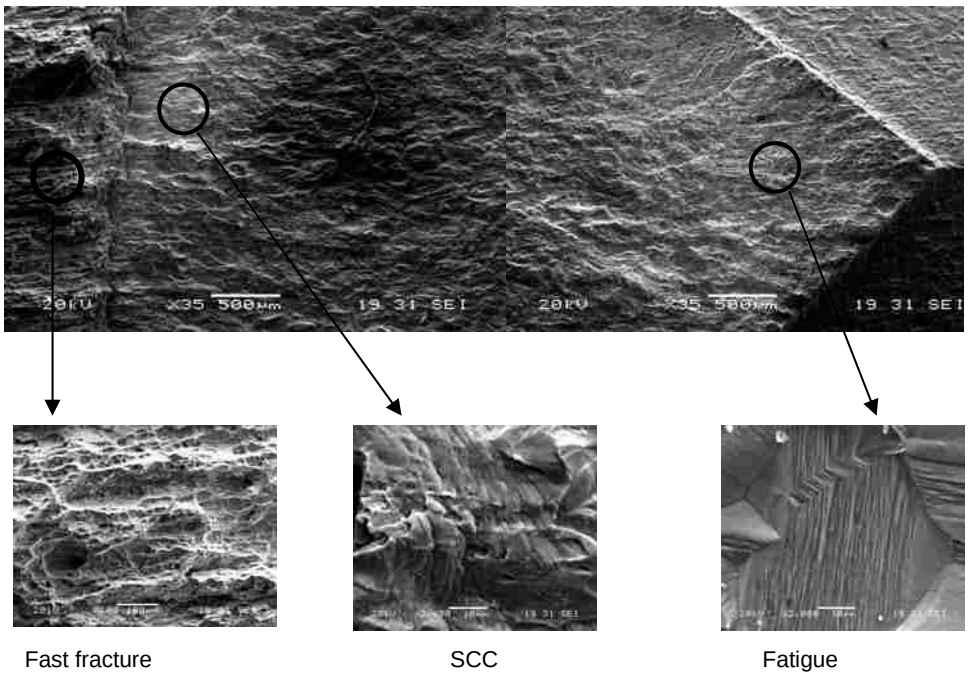

Figure 4-34 SEM Micrographs of a DCB Specimen (Four Months, High K)

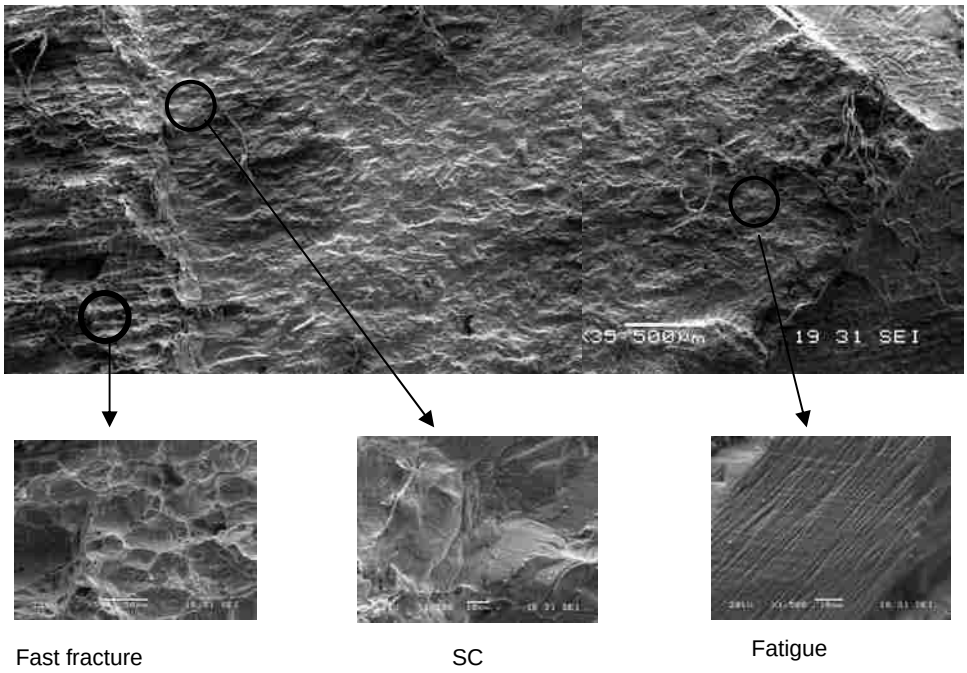

Figure 4-35 SEM Micrograph of a DCB specimen (Four Months, Low K)

4.6 Results of Stress Rupture Testing

Results of stress rupture tests, including the time to failure and Larson-Miller parameter (LMP), are given in the Table 4-11. LMP is a measure of predicting life-time of a material, as functions of time and temperature using a correlative approach based on an Arrhenius rate equation. Since a limited number of testing has been performed in this investigation, life-time could not be calculated by extrapolation . The magnitude of LMP constant (C) was determined from Figure 4-36. An estimated value of C was found to be approximately 43, which is greater than a conventional value of 20, cited in the open literature [43].

Table 4-11 Stress Rupture Testing Results

Temperature, °C	Applied Stress Level, Ksi (MPa)	Time to Failure (t_f), hr	LMP
750	25 (172.37)	590	44833
800	25 (172.37)	87.8	48223
850	25 (172.37)	6.7	50026

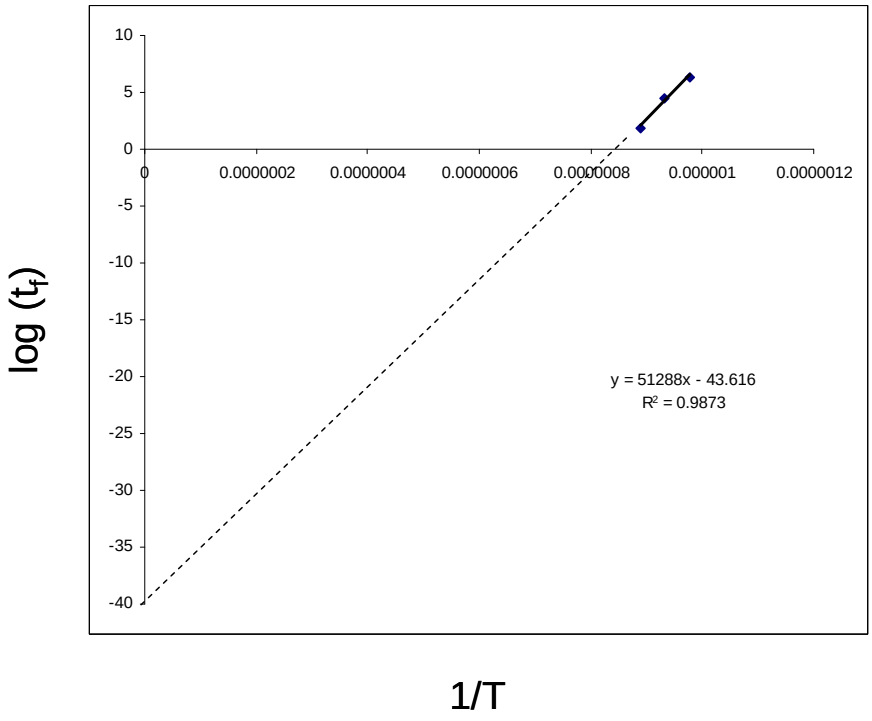

Figure 4-36 log (t_f) vs. 1/T

4.7 Characterization of Defects

Transmission electron microscopy (TEM) has been used to characterize defects including dislocations and precipitates within grains, and in and around the grain

boundaries of Alloy 617, developed during its time-dependent deformation at three tested temperatures. Figure 4-37 illustrates a TEM micrograph of a specimen tested under a sustained loading of 0.25YS value (59 MPa), showing dislocation pile-up at grain boundaries and sub-grains formed within the austenitic grains. The formation of precipitates is also evident in Figure 4-38 that resulted during creep deformation at this temperature. Precipitates formed within the austenitic grains can lead to the development of sub-grains. Both grain boundary precipitation and sub-grain formation can inhibit dislocation motion [37, 46, 78,], thus preventing accelerated deformation rate of Alloy 617 under relatively lower applied stress levels (0.10YS and 0.25YS), showing prolonged steady-state creep curves. Parallel dislocation lines were also seen in the TEM micrograph developed by selected area deflection, as shown in Figure 4-39.

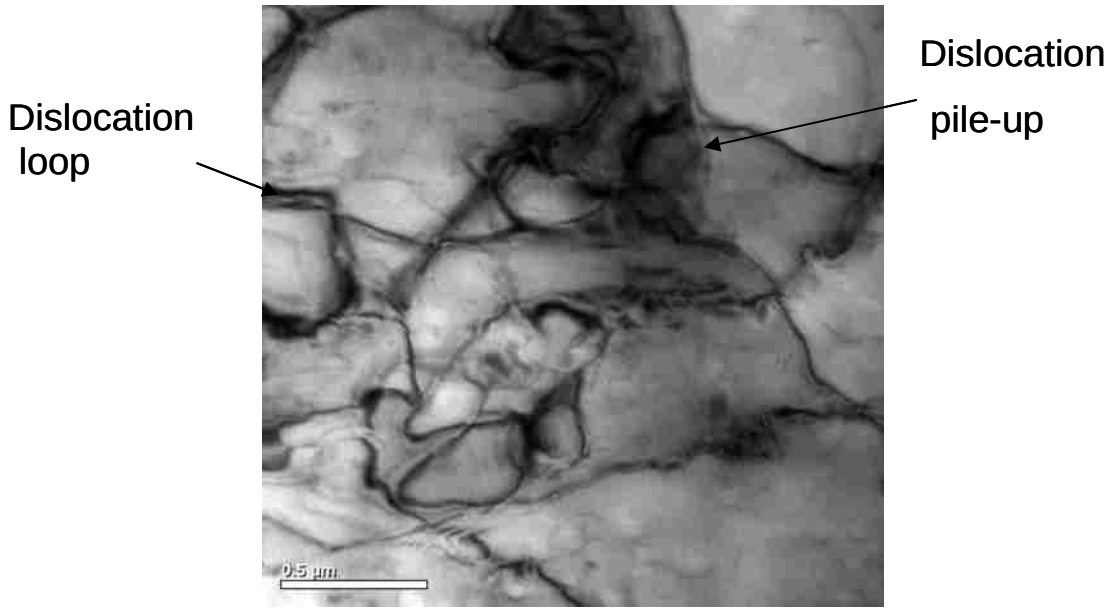

Figure 4-37 TEM Micrograph of Specimen Tested at 59 MPa-850°C

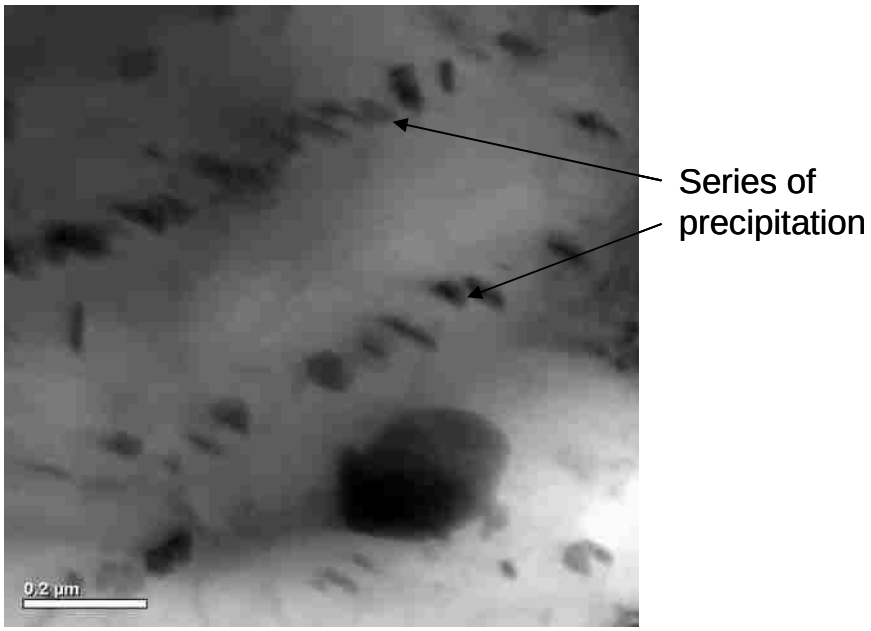

Figure 4-38 TEM Micrograph Showing Precipitates

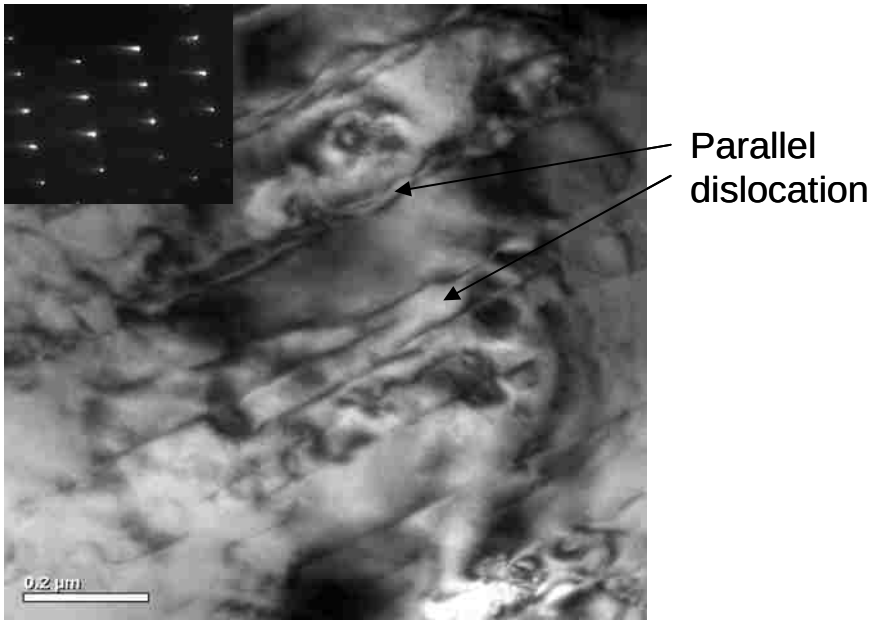

Figure 4-39 Selected Area Diffraction (SAD) showing Parallel Dislocations

There are indications in the open literature [32, 37] that carbides of M_6C and $M_{23}C_6$ types can be precipitated at the grain boundaries and as intragranular particles during solution-annealing treatment of Ni-base alloys. Scanning transmission electron microscopic (STEM) image mode and energy dispersive spectroscopy (EDS) were used for elemental analyses both at a precipitate and within the matrix of Alloy 617. The resultant spectra at a precipitate and within the matrix are shown in Figures 4-40 and 4-41, respectively. As expected, both spectra exhibited elements that are commonly present in Ni-base austenitic alloys including Alloy 617. However, these spectra indicate that the concentrations of Cr and Mo were enhanced in the precipitate relative to those within the matrix. Simultaneously, the Ni content in the precipitate was significantly reduced. The increased concentrations of Cr and Mo were also observed in a line scan spectra (Figure 4-42), suggesting that the resultant precipitates most likely consisted of carbides of Cr and Mo.

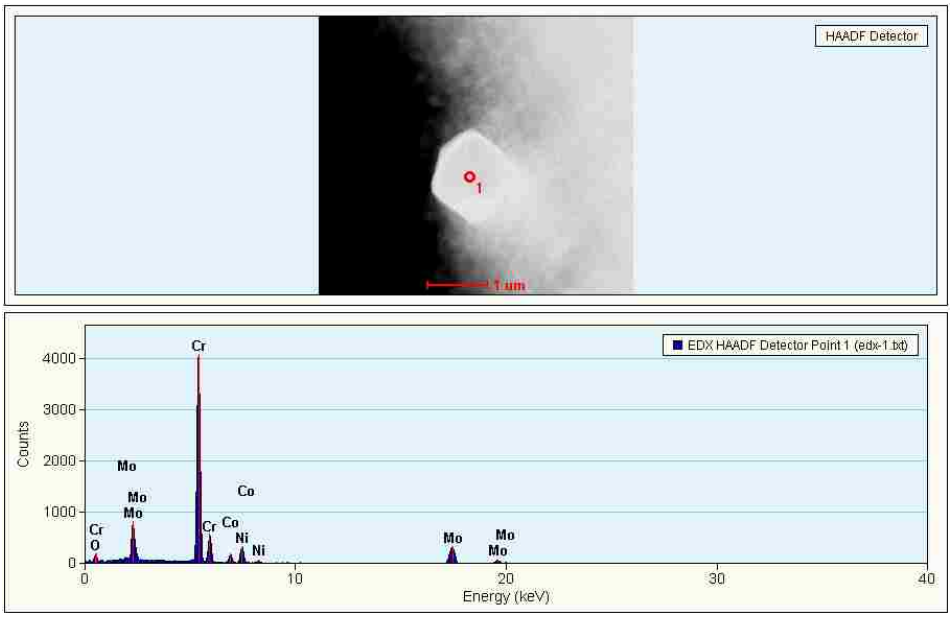

Figure 4-40 Spectra for Precipitate

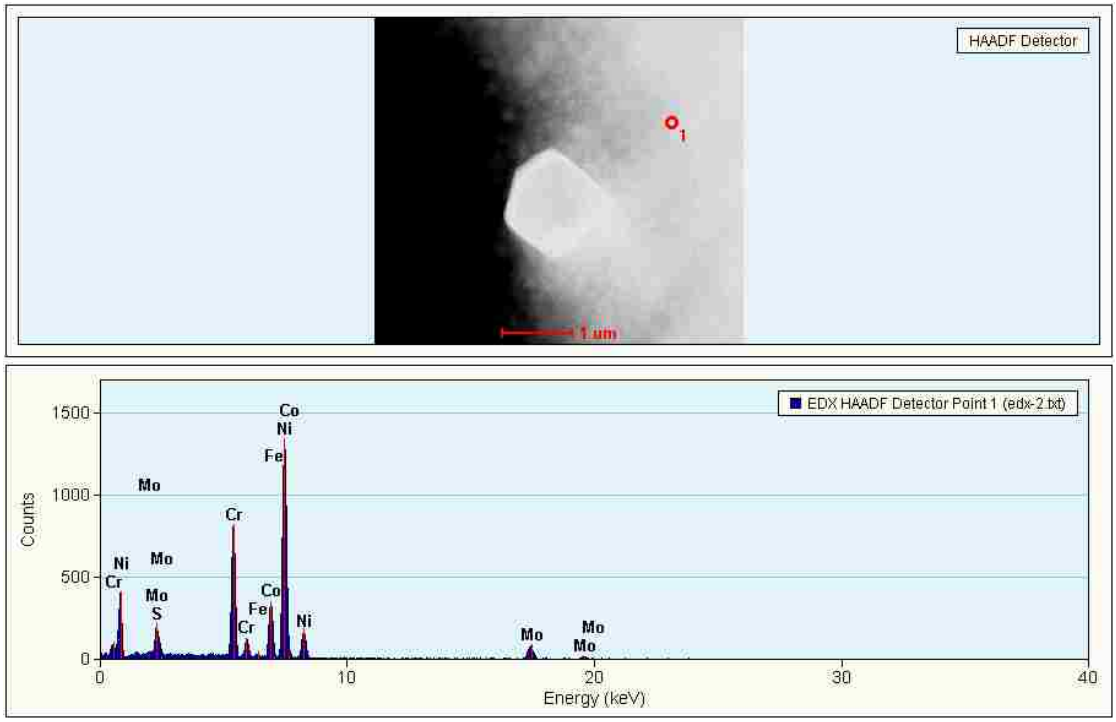

Figure 4-41 Spectra for Matrix

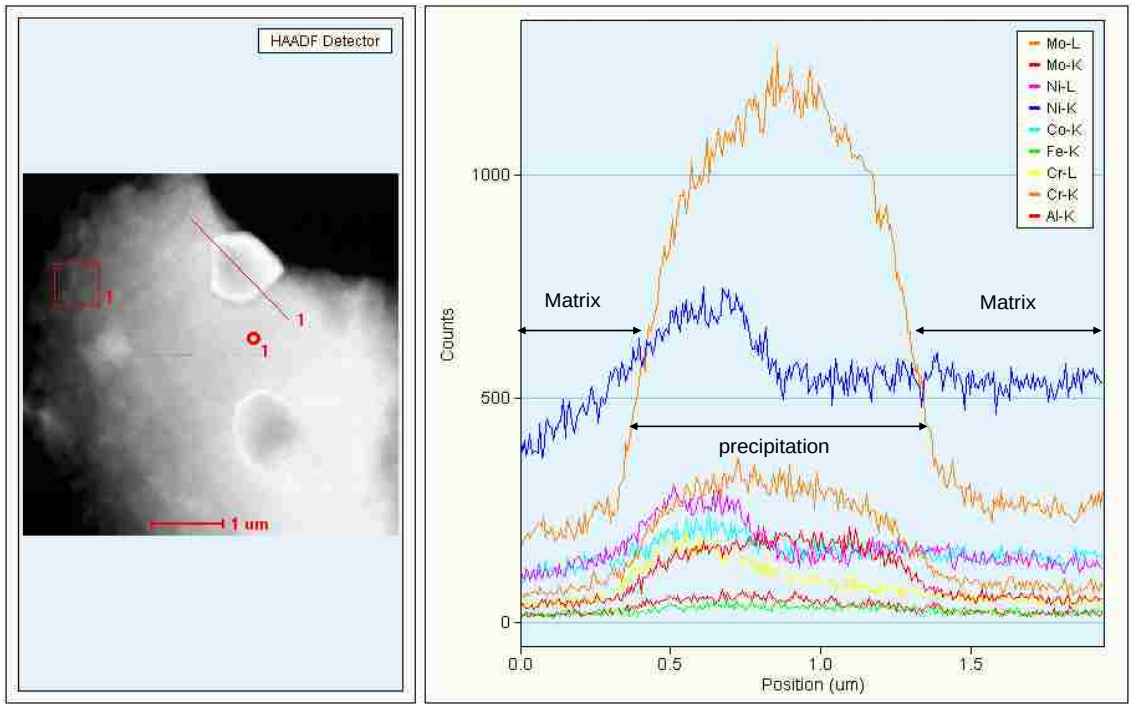

Figure 4-42 Line scanning for Precipitate and Matrix

4.8 Grain Size Measurements

The metallurgical microstructures of Alloy 617, tested under applied stress levels corresponding to its 0.25YS values at 750, 850 and 950 °C, are shown in Figure 4-43 (a, b and c). The ASTM grain size number (G) and the average grain diameters, determined from these micrographs by the mean lineal intercept method (8), are given in Table 4-12. The average diameter of the austenitic grain in the as-machined condition was 0.097 mm. However, the average grain diameter was increased from 0.098 mm to 0.126 mm when tested within a temperature range of 750 to 950 ºC under different applied stress levels. Standard deviations of ± 0.013 mm were determined based on these measured grain diameter values. The overall data suggest that there was a tendency for the grain size of this alloy to slightly enhance as the temperature and/or testing time were increased. The corresponding values of G at different temperatures ranged between 4 and 3, as shown in Table 4-12.

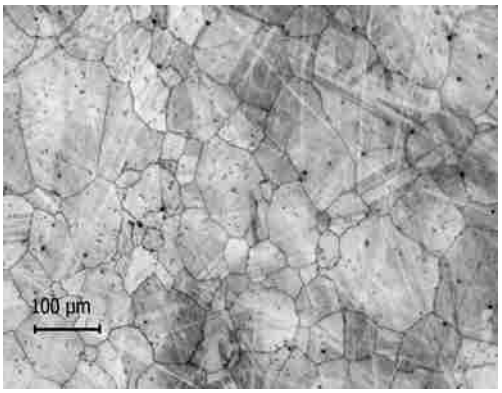

(a) 750 ºC, 22 MPa, 1000 hr

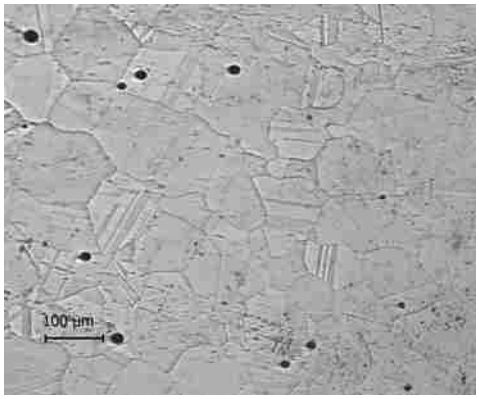

(b) 850 ºC, 24 MPa, 1000 hr

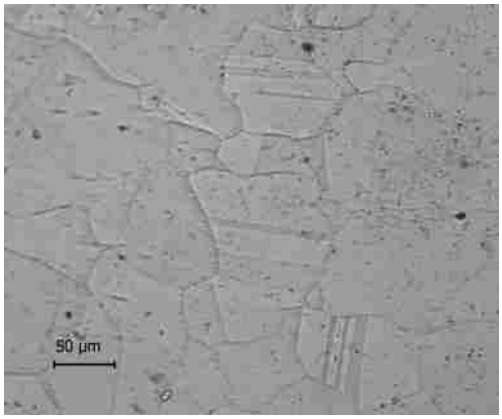

(c) 950 ºC, 18 MPa, 216 hr

Figure 4-43 Optical Micrographs of Tested Specimens, Kalling's Reagent

Table 4-12 ASTM Grain Size (G) vs. Temperature

Temperature	G	Average Grain Diameter (mm)
Ambient	3.66 ~ 4	0.097
750 ^{o}C	3.66 ~ 4	0.098
850 ^{o}C	2.66 ~ 3	0.124
950 ^{o}C	2.66 ~ 3	0.126

4.9 Fractographic Evaluation of CT Specimens

SEM micrographs of a broken CT specimen used in fracture toughness (J_{IC}) testing are illustrated in Figure 4-44, showing three fractured regions. The pre-cracked region was characterized by striations due to cyclic loading. The region that experienced loading and unloading sequences during J-Integral testing, suffered from brittle

transgranular failure. Finally, the broken surface of the tested specimen showed dimpled microstructure resulting from fast fracture, indicating ductile failure.

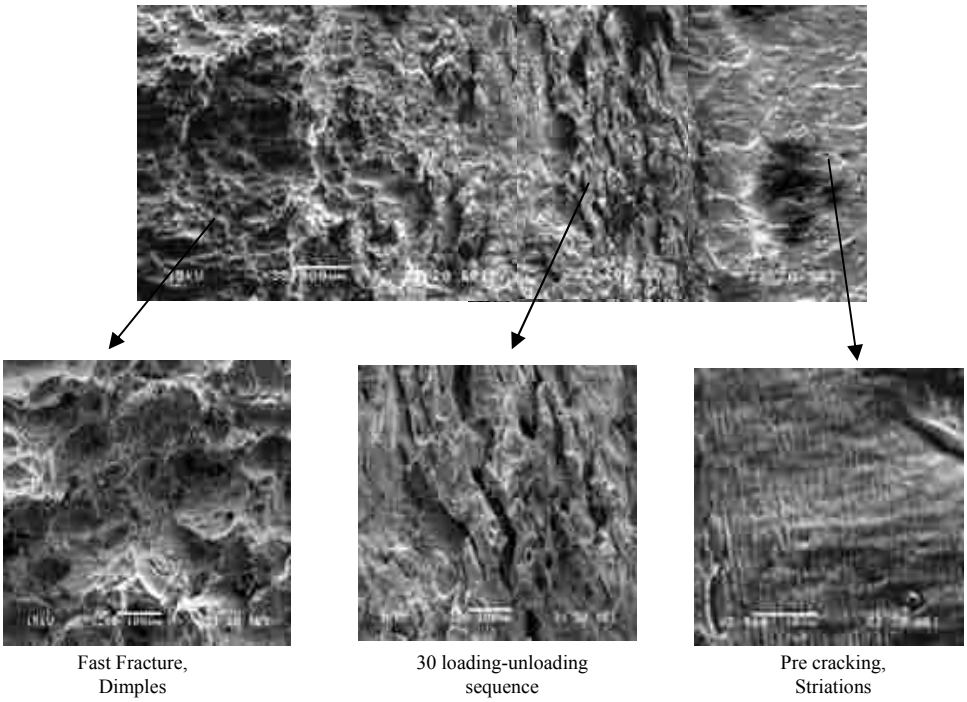

Figure 4-44 SEM Micrographs of a Broken CT Specimen used in J_{IC} Testing

The fracture morphologies of broken CT specimens, used in CGR testing at ambient temperature and 300 ^{o}C, are illustrated in SEM micrographs (Figures 4-45 and 4-46, respectively). Once again, the notched area was characterized by striations resulting from repeated cycles of loading, followed by dimples due to ductile tearing of the specimen by tensile over-load upon completion of the CGR testing.

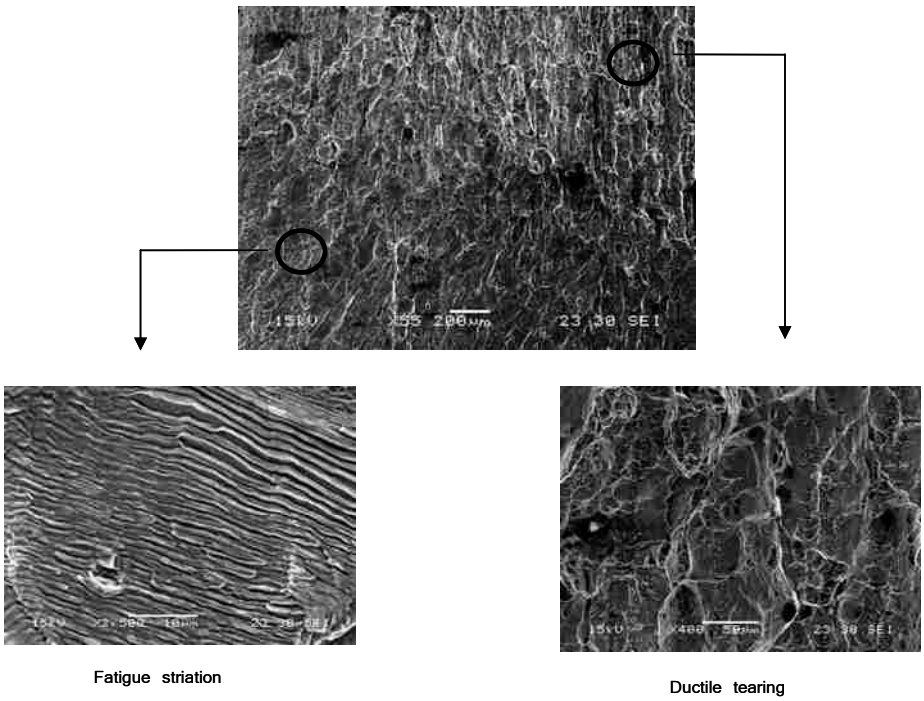

Figure 4-45 SEM Micrographs of a Broken CT Specimen

(CGR Testing, Room Temperature)

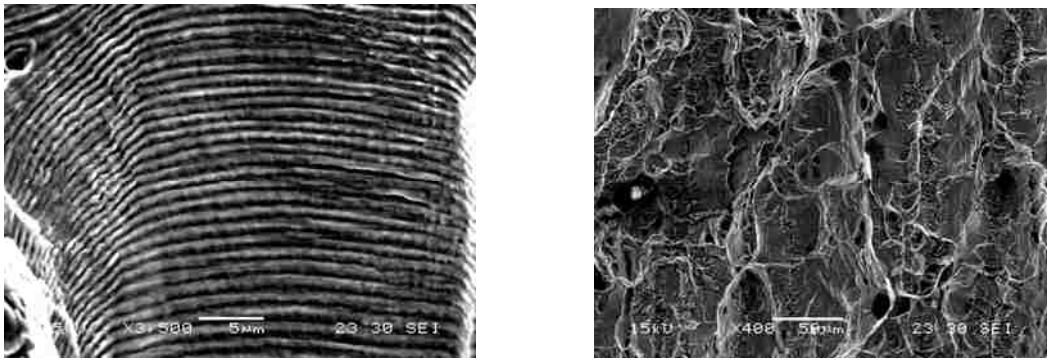

(a) Striations, 3500X (b) Dimples, 400X

Figure 4-46 SEM Micrographs of a Broken CT Specimen

(CGR Testing, 300 °C)

4.10 Results of X-ray Diffractometry

The XRD samples were harvested from creep test specimen and were ground and polished to a 3 micron finish. XRD pattern were taken using a PANalytical X'Pert Pro X-ray diffractometer with multiple silicon strip detector (X'Celerator) as shown in Figure 4-47 and Figure 4-48.

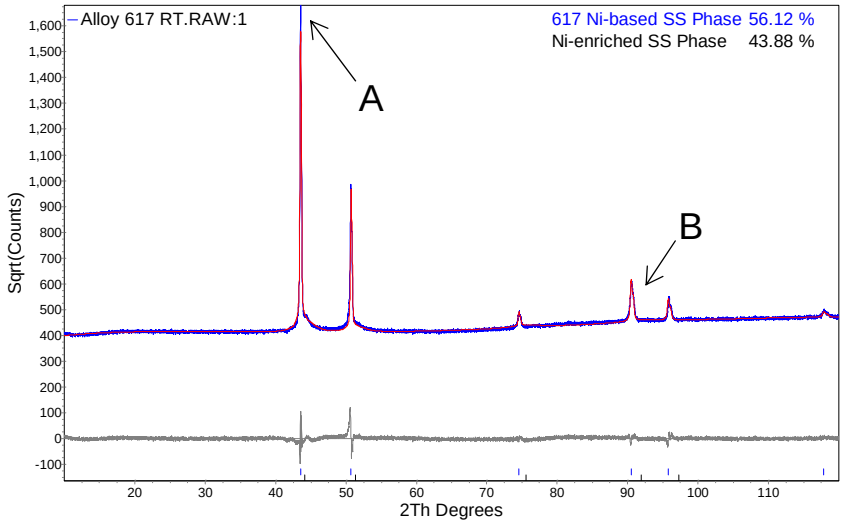

Figure 4-47 XRD/Rietveld Analysis of Alloy 617 at RT, 3 micron finish

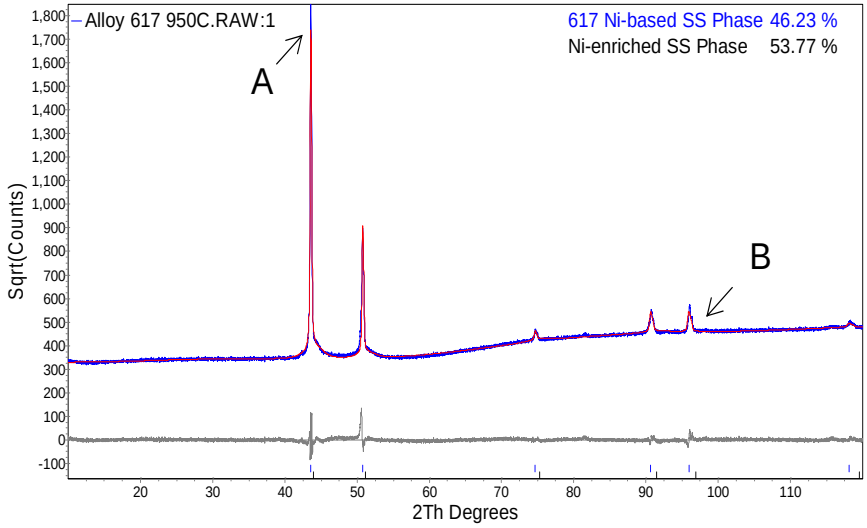

Figure 4-48 XRD/Rietveld Analysis of Alloy 617 at 950°C, 3 micron finish

In both the X-ray patterns of Figure 4-47 and 4-48 blue line (A) represents the measured pattern and the red line (B) represents the calculated pattern. Texture model of spherical harmonics of 8th order was applied to optimize the fit and to achieve low refinement residuals (Rwp = 3.4%). The Lattice parameter (a) was calculated to be 3.59311 ± 0.00005 Å from the multiple silicon detector XRD analysis.

Further, the specimen Alloy 617 at RT was prepared to be measured with a high-resolution Bruker AXS Vario powder-diffractometer and the data (6 hour data collection) are displayed in Figure 4-49. Rietveld analysis was performed and a refinement residual Rwp of 8.8% was achieved. The relative large refinement residuals are a result of fewer total peak intensities and very small FWHM as a result of the experimental set-up (Johansson monochromator, scintillation counter, small detector slits). In addition, this high-resolution set-up does not provide greater accuracy in the lattice parameter refinement (a =3.599 ± 0.004 Å). It has to be noted that all Alloy 617 pattern especially the (002) refection do show Lorentzian type strain broadening prospectively due to the impact of machining the creep test specimen.

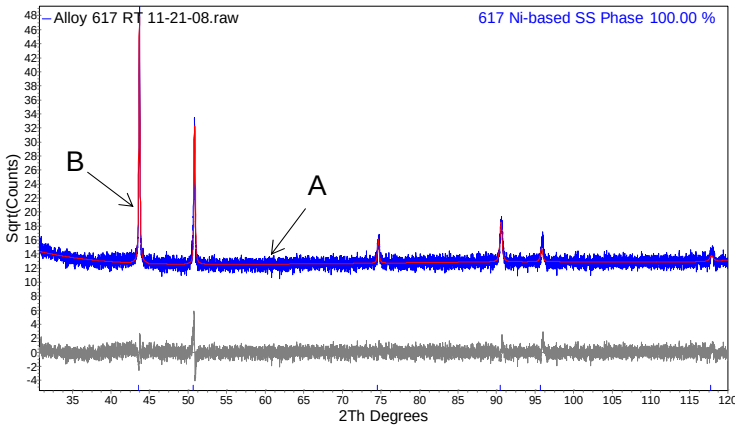

Figure 4-49 XRD/Rietveld Analysis of Alloy 617 at RT, 3 micron finish

CHAPTER 5

DISCUSSION

Austenitic Ni-base Alloy 617 has been extensively studied in this investigation to evaluate its metallurgical, mechanical and corrosion behavior for prospective application as a structural material in the NGNP program to generate electricity and hydrogen using nuclear heat. These studies include microstructural evaluation as a function of temperature, crack-growth-rate (da/dN) and fracture toughness (J_{IC}) evaluation, characterization of time-dependent plastic deformation (creep), estimation of failure time as functions of applied stress and temperature (stress-rupture), determination of cracking susceptibility in an acidic solution (SCC), defects and precipitates characterization, and fractographic evaluation of relevant tested specimens using different state-of-the-art analytical tools.

5.1 Microstructure and Grain Size Evaluations

Austenitic grains and annealing twins, common characteristics of solution-annealed Ni-base alloys, were observed in the optical micrographs of Alloy 617 tested at different temperatures. The average grain diameter was increased at 850 and 950 ^{o}C, causing a change in the ASTM grain size number (G) from 4 to 3. Carbide precipitation was also observed within the austenitic grains. The larger grain size at 950 °C indicates that this material can undergo considerable amount of deformation before failure, resulting in loss of strength, and hence, substantial amount of creep.

5.2 Creep Evaluation

The results of creep testing revealed somewhat higher anelastic (elastic plus plastic) strain at higher applied stresses and temperatures before the onset of time-dependent

plastic deformation, possibly due to reduced modulus of elasticity at elevated temperatures. Even though three-stage creep curves were observed in the overall testing, the primary creep curve was relatively shorter at higher initial applied stress levels, especially at 950 ^{o}C. As to the secondary or steady-state region, substantially longer creep curves were seen at 750 and 850 ^{o}C, when the specimens were loaded at 0.10YS values at these temperatures. However, the secondary creep curve became shorter with increasing stress levels of 0.25YS and 0.35YS at these temperatures, finally disappearing at 950 ^{o}C, showing only a steeper tertiary creep curve. Assuming that a heat exchanger material must not suffer from creep deformation beyond 1% strain following 1000 hours of loading under different levels of applied stresses, it could be stated that Alloy 617 may not be able to sustain an operating temperature of 950 ^{o}C at applied stresses above its 0.10YS value. Nevertheless, this alloy was capable of withstanding all four levels of applied stresses (0.05YS. 0.10YS, 0.25YS and 0.35YS) at 750 ^{o}C for durations exceeding 1000 hours. Although, this alloy was very close to meeting the acceptable strain criterion of 1% in 1000 hours of loading at 0.25YS-850 ^{o}C, the inference is strong that Alloy 617 may not be suitable for NGNP application under operating stresses equivalent to its 0.25YS and 0.35YS values at 850 ^{o}C and above. Average activation energy for creep deformation (Q) of this alloy ranges from 132 to 606 kJ/mole., which is close to the lower bound of Q values cited in the open literature. Q is observed to increase which could be explained by realizing that Q is function of several parameters like stress component, stress, temperature and a constant. Change of slip systems, formation of sub grains, dislocation pile ups, blocking of dislocation movement and precipitations of type $M_{26}C_6$, M_6C carbides within the matrix were observed in the TEM micrographs of the specimen

tested at 750 °C at 0.10YS. All these factors can contribute to lower creep deformation at 750 and 850 °C at an applied stress level of 0.05 and 0.10YS. At 950 °C, these carbides may undergo dissolution, subsequently causing migration of carbides and creation of voids that could lead to the faster deformation in the tertiary region and a short steady-state region. The EDS spectra suggest that the precipitates could be made of carbides of Cr and Mo.

5.2 Crack-growth-rate Evaluation

The results of crack-growth-rate (CGR) study indicate that the magnitude of CGR in terms of da/dN was significantly higher at 100 ^{o}C, irrespective of the R value. Even though the CGR was further enhanced at 300 ^{o}C, the rate of increase was sufficiently lower compared to that at 100 ^{o}C, suggesting that the crack might have reached a critical length beyond which appreciable crack extension may not occur. At 300 ^{o}C, the number of cycles (N) needed for comparable crack extension was significantly reduced at an R value of 0.1, thus causing a maximum CGR in terms of da/dN. An R value of 0.1 corresponded to a maximum loading constraint due to the highest load range (ΔP) of 4.5 kN used during the CGR testing. The combined effect of higher temperature and lower R value in enhancing the cracking susceptibility of Alloy 617 was also noted in terms of the number of cycles to failure (N_f). Activation energies for crack extension (Q) were determined to be within the range of 139 to 151 J/mole, which seem to be close to that of another Ni-base Alloy 276. The overall CGR results suggests that the crack propagation almost reached a threshold point at 300 °C, probably due to blunting of the crack-tip at elevated temperatures. Thus, even though testing could not be performed beyond 300 °C

due to the failure of the Instron furnace, it can be predicted that the crack growth rate of this alloy would not enhance any further at temperatures higher than 300 °C.

5.3 Fracture Toughness Evaluation

With respect to the fracture toughness of this alloy in terms of J_{IC}, slight reduction in fracture toughness was noted with increasing temperature from ambient to 100 to 200 ^{o}C. However fracture toughness values changes insignificantly within the temperature range of 200ºC to 500ºC and based on the literature it can be concluded that this alloy can maintain the same fracture toughness values up to 700ºC. The fracture toughness values, in terms of J_{IC}, K_{IC} and δ, were significantly higher compared to those of other engineering materials, implying an adequate toughness of this alloy at ambient and elevated temperatures. The magnitude of the tearing modulus (T), which is a measure of a material's resistance to tearing instability, was found to be well above 100, suggesting that Alloy 617 would be resistant to tearing at temperatures ranging from ambient to 500 ^{o}C.

5.4 Stress-corrosion-cracking Evaluation

The results of SCC testing indicate that the pre-cracked and wedge-loaded DCB specimens of Alloy 617 experienced continuous growth of cracking in a 100 ^{o}C acidic solution while loaded under different initial stress intensity factor (K_I) values for variable exposure periods. The reduction in wedge load (ΔP) due to crack extension was more pronounced for specimens loaded to relatively higher K_I values. The overall data suggest that SCC testing for periods longer than 8-month may be necessary to establish a threshold stress intensity factor for SCC (K_{ISCC}), below which no further crack-growth would occur. It is to be noted that due to leaking of the autoclave, SCC testing could not

be performed at temperatures beyond 100 °C. In addition, testing at temperatures higher than 300 °C can not be conducted in the liquid phase since the boiling point of sulfuric acid is around 327-340 °C at 100 kPa.

Fractographic evaluation of the tested DCB specimens revealed striations, cleavage failures, and dimples in the SEM micrographs along their broken surfaces. The CT specimens used in J_{IC} and CGR testing also exhibited striations at the notched area due to cyclic loading, and dimpled microstructures due to fast fracture by tensile loading. Additionally, transgranular brittle failures were observed in the CT specimens during J_{IC} testing by virtue of the loading-unloading sequences.

CHAPTER 6

SUMMARY AND CONCLUSIONS

Alloy 617 has been extensively studied for evaluation of its metallurgical and mechanical properties, and corrosion susceptibility under conditions relevant to the NHI and NGNP programs. The key results and significant conclusions drawn from this investigation are summarized below.

- Austenitic grains and annealing twins, two common microstructural characteristics of solution-annealed nickel-base alloys, were observed in the optical micrographs of Alloy 617. Precipitation of carbides was also seen in these micrographs.
- The average grain size of this alloy was slightly enhanced due to a change in temperature from ambient to 950 °C.
- The primary creep curve of this alloy was very short, irrespective of the testing temperature and the applied stress level.
- Severe creep deformation, characterized by the formation of an instantaneous tertiary region, was observed with Alloy 617 when testing was performed at 850 and 950 ^{o}C under applied stresses equivalent to its 35% YS values (83 and 64 MPa) at these temperatures.
- This alloy was capable of sustaining all four levels of applied stress (11, 22, 54 and 78 MPa) for durations exceeding 1000 hours at 750 ^{o}C. Considering a maximum allowable strain of 1% following 1000 hours of sustained loading, this alloy may be suitable for use as a heat exchanger material under applied stresses not exceeding its 0.10YS values at temperatures up to 750 °C.

- At 950 °C and higher applied stresses, the unstable intragranular carbides and grain boundary carbides may undergo dissolution, causing migration of carbides and grain boundaries that could lead to the initiation of voids. Such event could account for enhanced creep deformation of this alloy at this temperature, as seen in this study.
- Average activation energy (Q) for creep deformation of this alloy was found to range between 290 and 351 kJ/mole.K.
- A Larson-Miller constant (C) of 43 was determined for Alloy 617, which is substantially higher, compared to its range (15-25) cited in the literature.
- The crack-growth-rate of this alloy, in terms of da/dN, was gradually enhanced with increasing temperature at a constant R value. However, the rate of increase of da/dN was substantially lower at 300 °C, compared to that at 100 °C, possibly due to a reduction in the modulus of elasticity (E) at the higher temperature.
- A maximum da/dN value was observed at the lowest R value of 0.1 due to a greater loading constraint associated with the largest ΔP value of 4.5 kN at a constant temperature.
- Consistent with the maximum da/dN value at an R value of 0.1, a lowest number of cycles to failure (N_f) was also observed at this R value, irrespective of the testing temperature. Interestingly, the number of cycles needed for comparable crack extension at a constant R value was also gradually reduced at relatively higher temperatures.

- Even though the slope (m) of the steady-state region in the da/dN versus ΔK plot was not influenced by temperature, a greater value of the intercept (A) was observed at higher temperatures when the R value was kept at 0.1, indicating enhanced cracking tendency.
- Average activation energy (Q) for crack-growth of approximately 144 J/mole was calculated for Alloy 617, which appears to be close to the Q value for another austenitic alloy.
- Increased ΔK values in constant-K CGR testing showed somewhat higher da/dN values due to a greater loading constraint, arising from reduced N values.
- Consistent with the literature data, no significant variation in J_{IC} was observed within a temperature range of ambient to 500 ^{o}C.
- A continuous growth of crack length was observed in DCB specimens due to a synergistic effect of the corrosive environment and the wedge-load during SCC testing conducted for variable exposure periods. The wedge-load was, however, significantly reduced in specimens subjected to higher initial stress intensity factor (K_I) values for longer testing durations.
- The TEM micrographs of the tested creep specimens showed precipitates, dislocation pile-ups, and sub-grains that could have contributed to reduced steady-state creep deformation at 750 and 850 °C.
- The CT specimens used in the CGR testing showed striations and dimpled microstructures in the SEM micrographs due to cyclic loading and fast fracture, respectively.

- Three types of fracture were observed along the broken surfaces of the DCB specimens used in SCC testing. They were brittle (striations), cleavage and ductile failures resulting from repeated loading cycles to pre-crack the specimen, occurrence of SCC due to environmental effect, and ductile tearing, respectively.

CHAPTER 7

SUGGESTED FUTURE WORK

- Additional SCC testing involving pre-cracked and wedge-loaded DCB specimens in an identical acidic environment for durations longer than 8-month may enable the determination of K_{ISCC}, below which no further crack-growth may occur.

APPENDIX A

CREEP TESTING DATA

WinCCS Data acquisition system

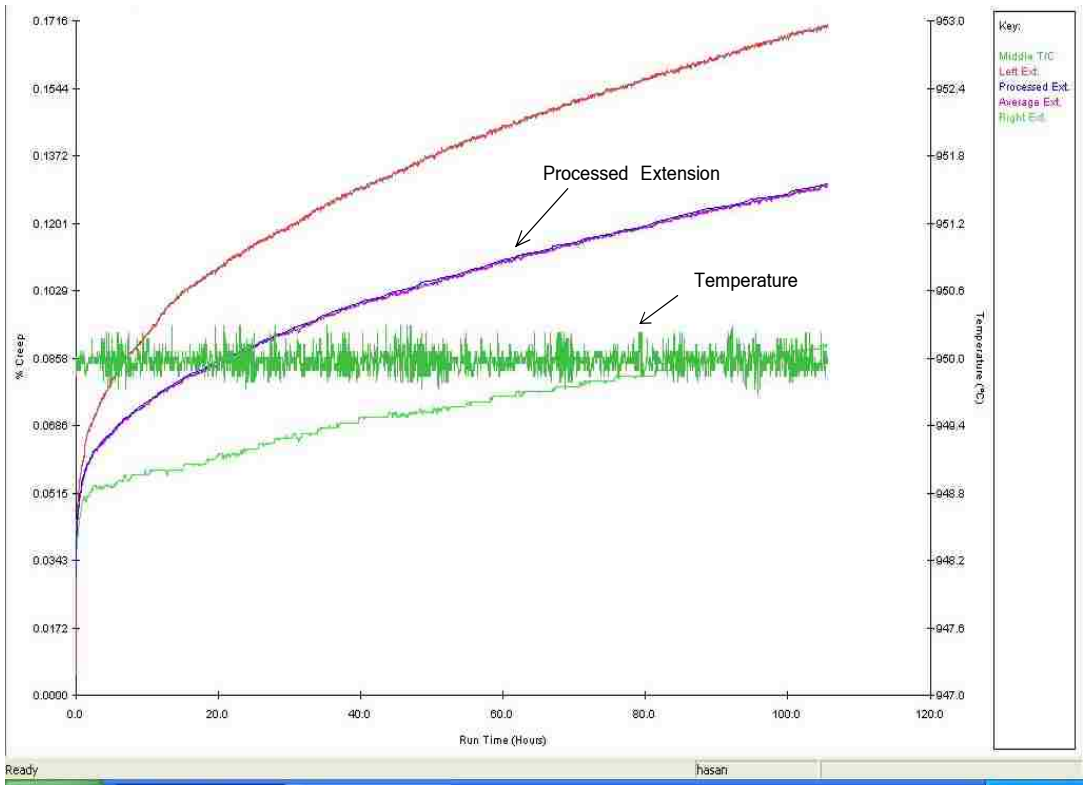

A1 Isothermal Creep Curves

A1.1 750 °C (Duplicate Test)

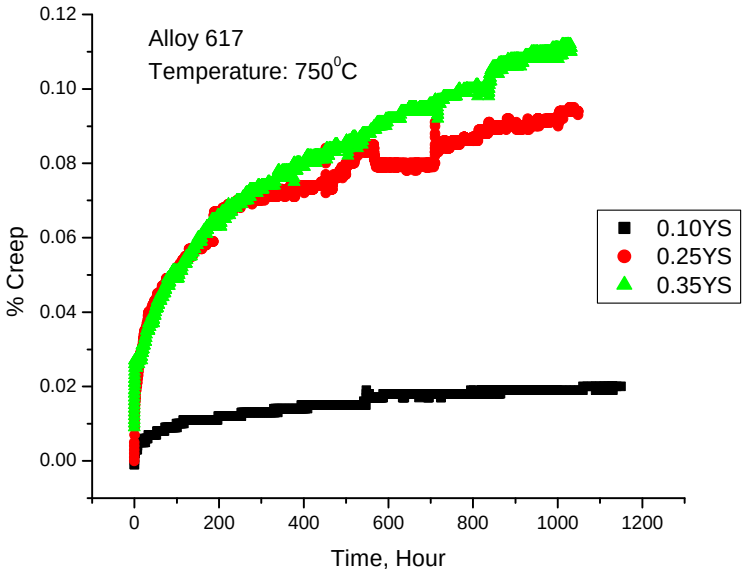
Alloy 617
Temperature: 750^{0}C
% Creep
Time, Hour
0.10YS
0.25YS
0.35YS
0.00
0.02
0.04
0.06
0.08
0.10
0.12
0
200
400
600
800
1000
1200

A1.2 850 °C (Duplicate Test)

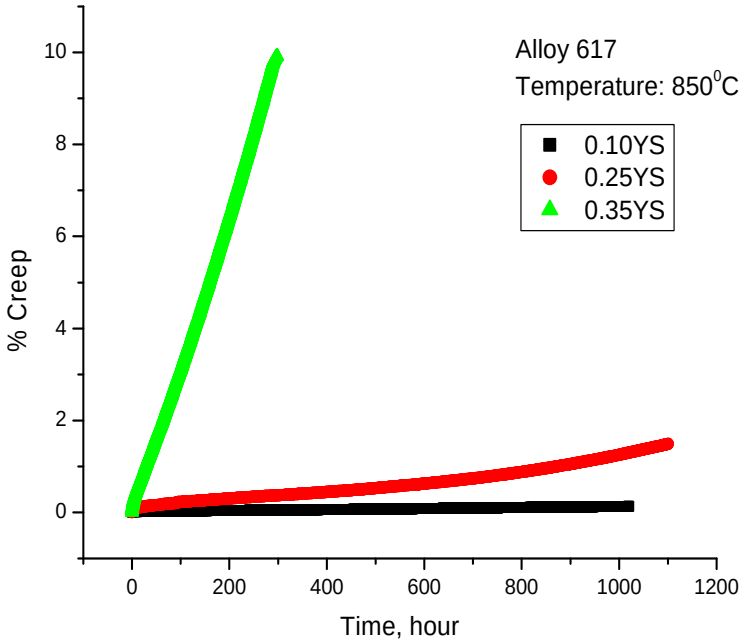

A1.3 950 °C (Duplicate Test)

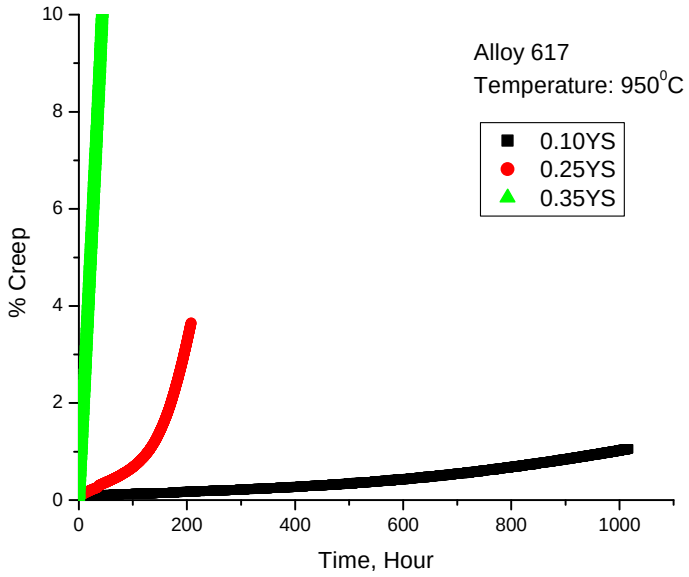

A1.4 750 °C@0.10YS (Duplicate Test)

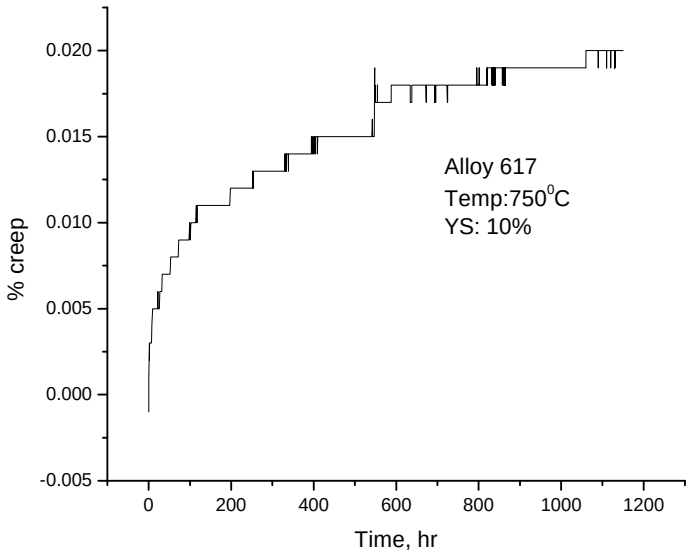

A1.5 950 °C @0.10YS (Duplicate Test)

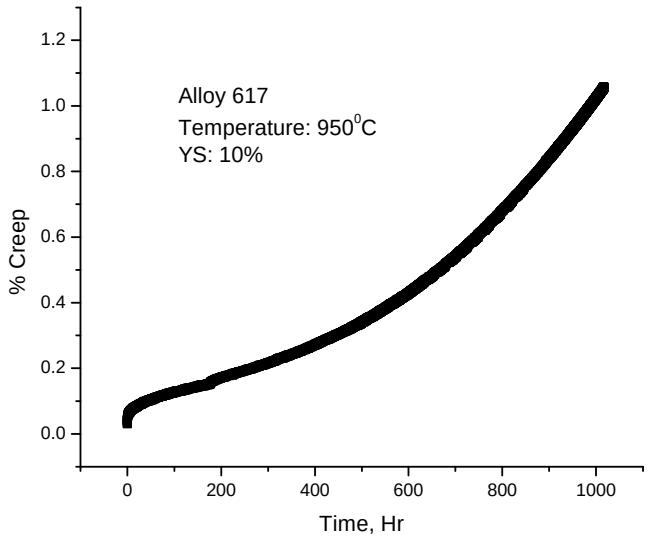

A1.6 750 °C @0.35YS (Duplicate Test)

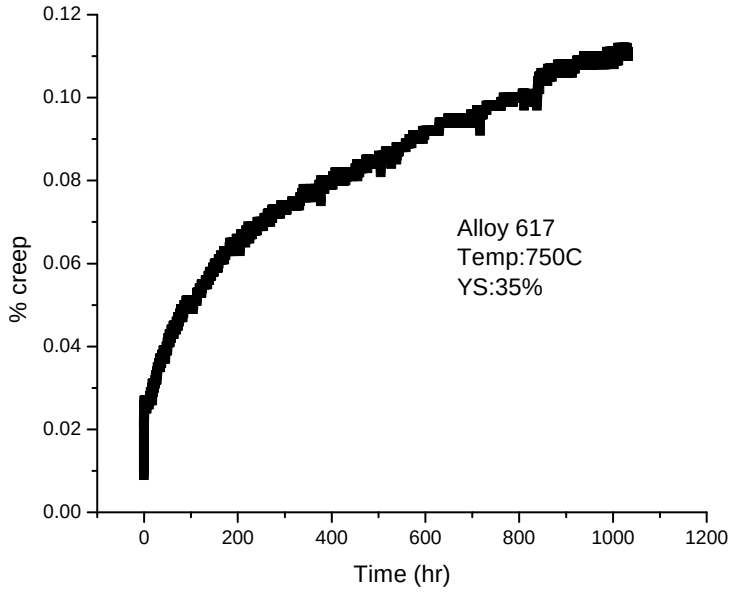

A1.7 Creep Rate calculation from Steady State Creep @ 750/850/950 °C

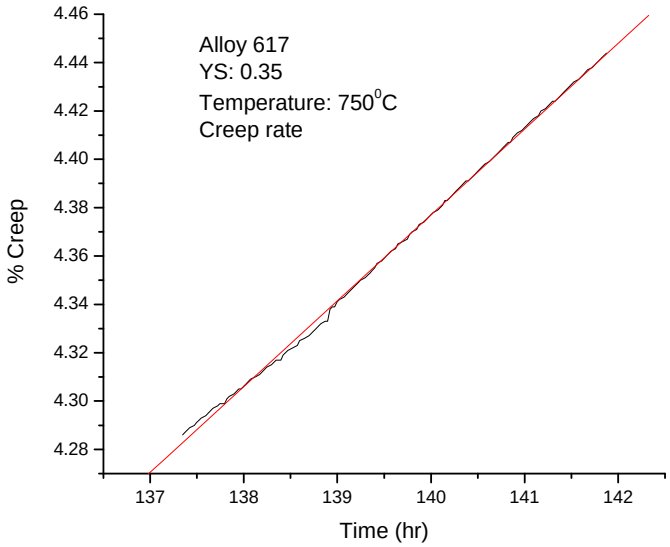
Alloy 617
YS: 0.35
Temperature: 750^{0}C
Creep rate
% Creep
Time (hr)
4.46
4.44
4.42
4.40
4.38
4.36
4.34
4.32
4.30
4.28
137
138
139
140
141
142

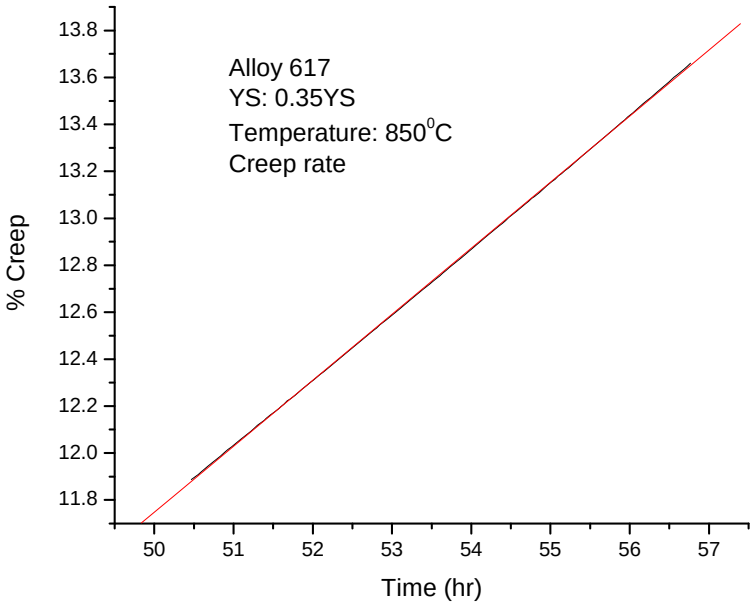
Alloy 617
YS: 0.35YS
Temperature: 850^{0}C
Creep rate
% Creep
Time (hr)
13.8
13.6
13.4
13.2
13.0
12.8
12.6
12.4
12.2
12.0
11.8
50
51
52
53
54
55
56
57

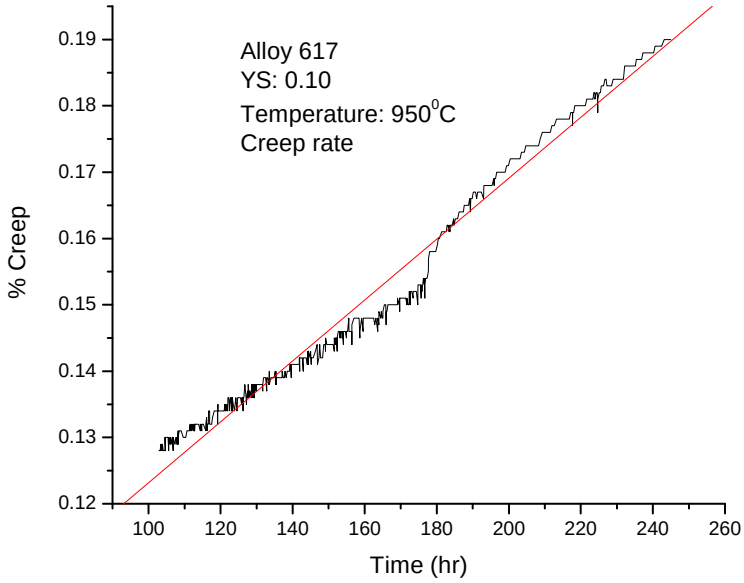

A2 Initial Rapid Elongation vs. Temperature and Applied Stress

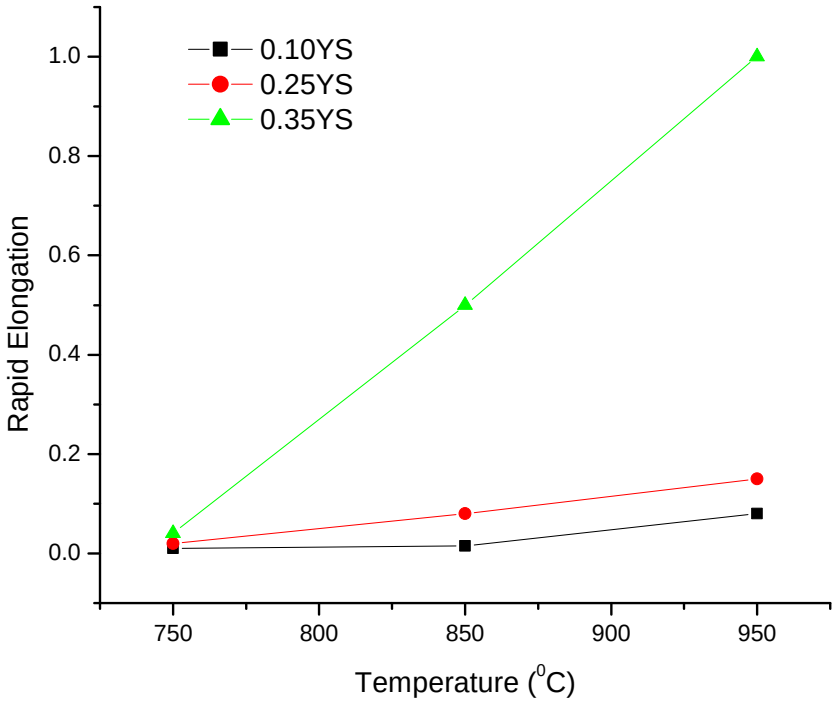

APPENDIX B

CRACK-GROWTH-RATE TESTING DATA

B1 Direct-current-potential-drop (DCPD) System

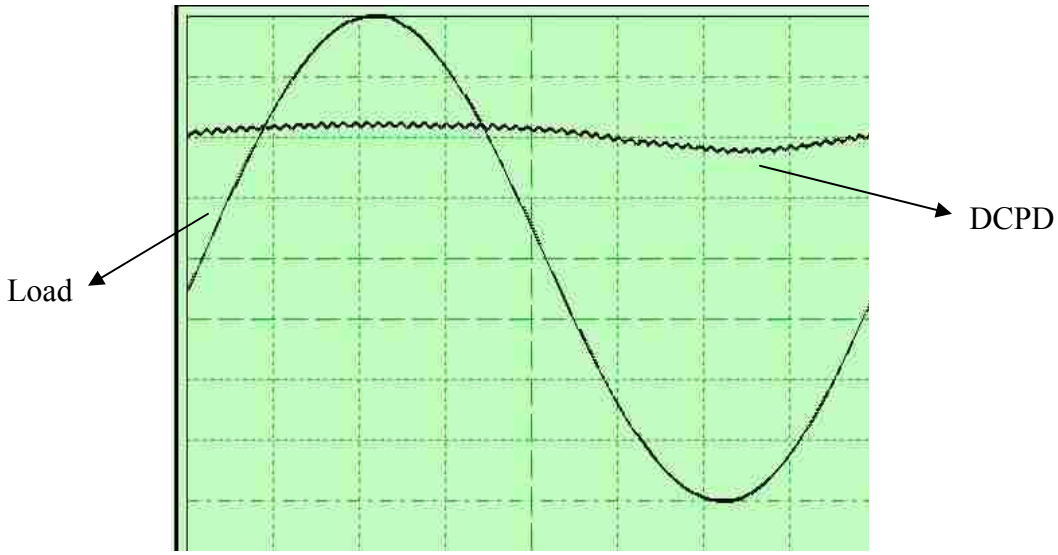

Load vs. DCPD

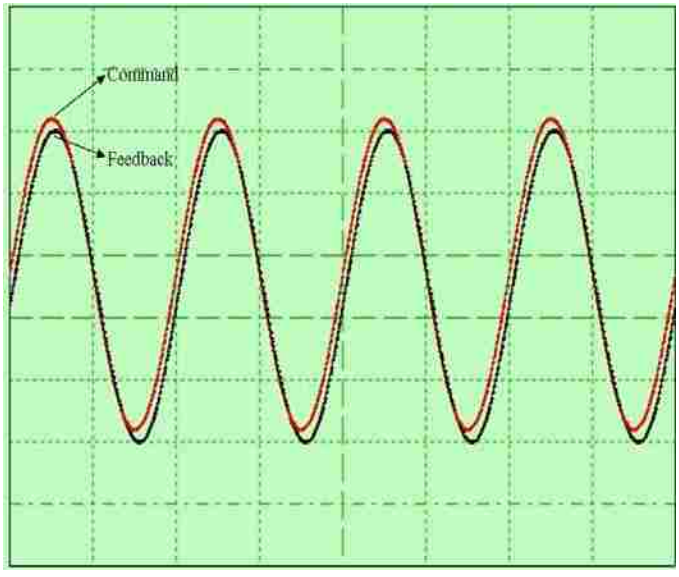

Command Load (DCPD) vs. Feedback Load (Instron)

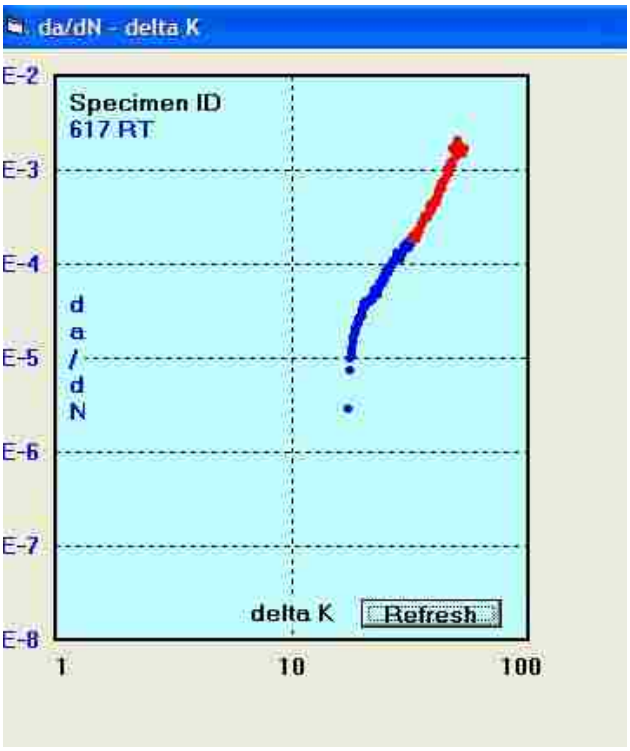

da/dN vs. Δk

B2 Constant-Load CGR Testing Data

B2.1 da/dN vs. ΔK Plots

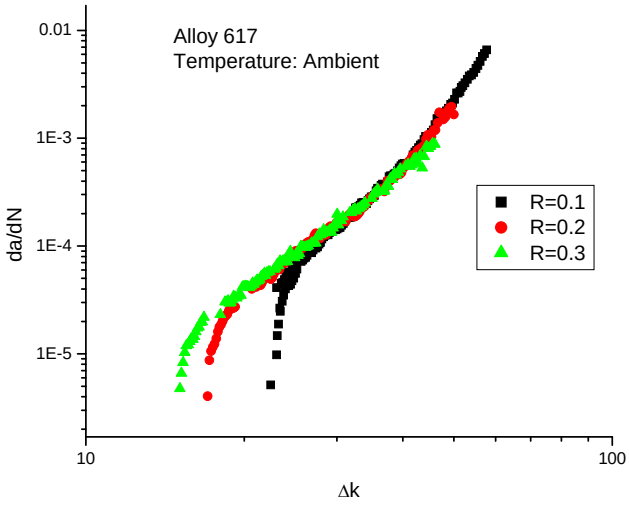

Ambient Temperature (Duplicate Test)

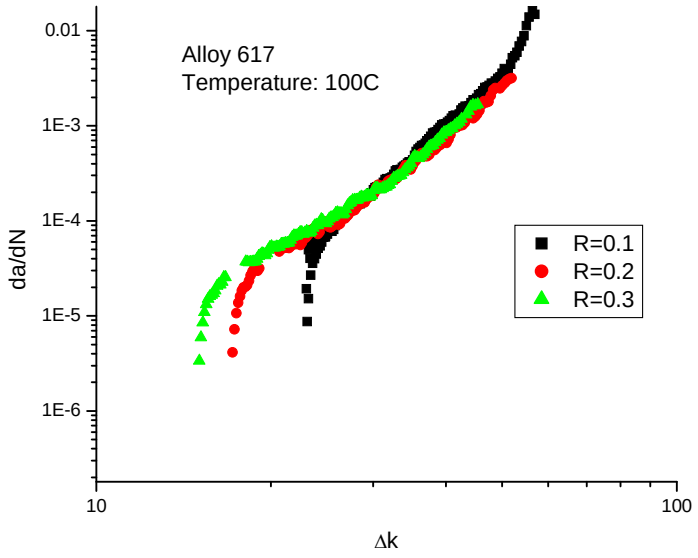

100ºC (Duplicate Test)

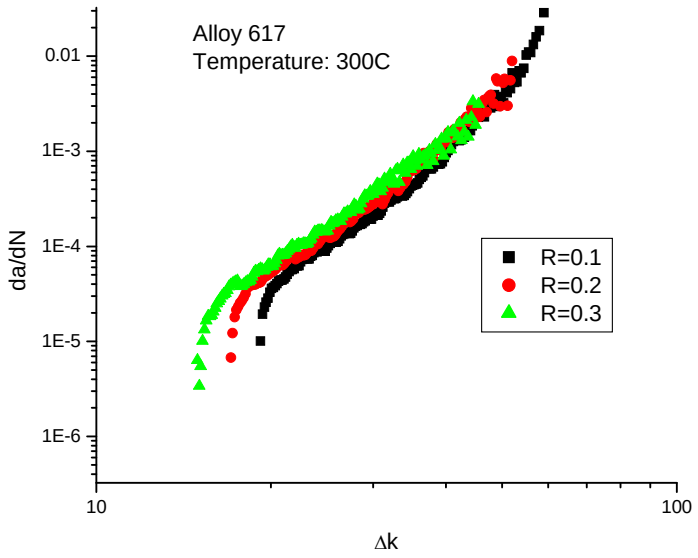

300ºC (Duplicate Test)

B2.2 Slope (m) calculations

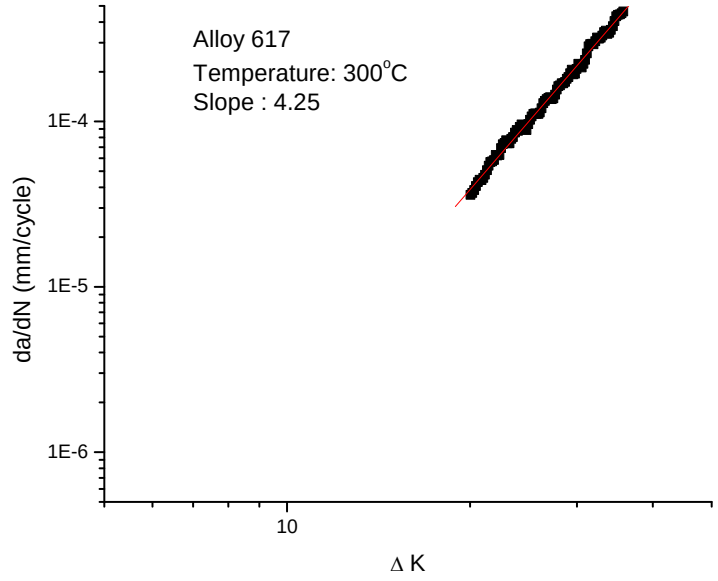

R = 0.1, T = 300ºC (Sample 2)

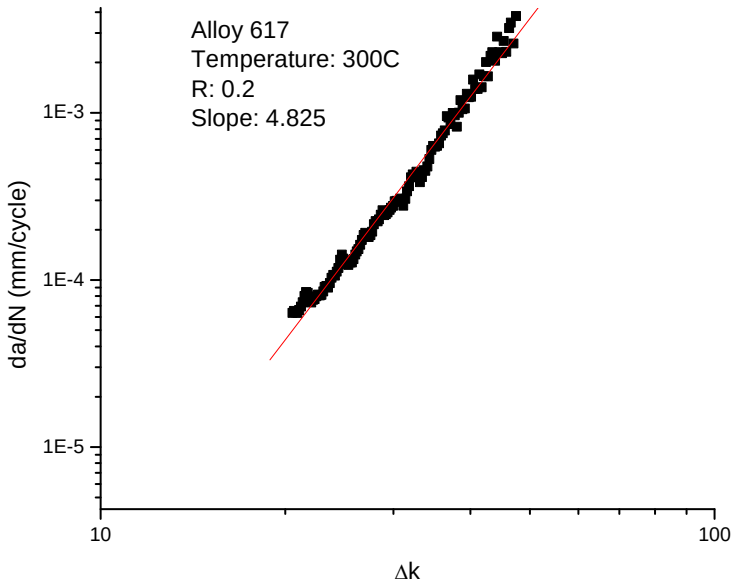

R = 0.2, T = 300ºC (Sample 2)

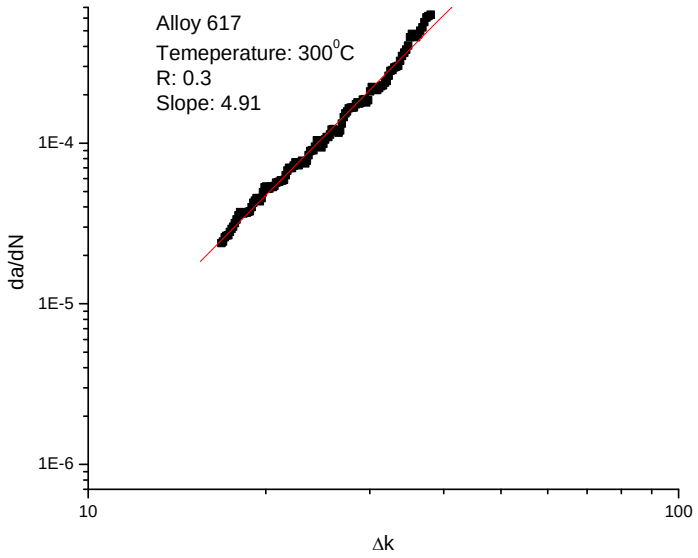

R = 0.3, T = 300ºC (Sample 2)

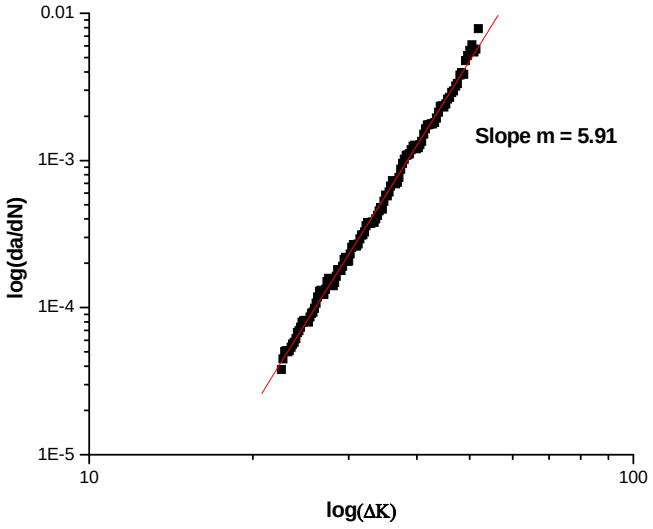

R = 0.1, T = 100ºC (Sample 2)

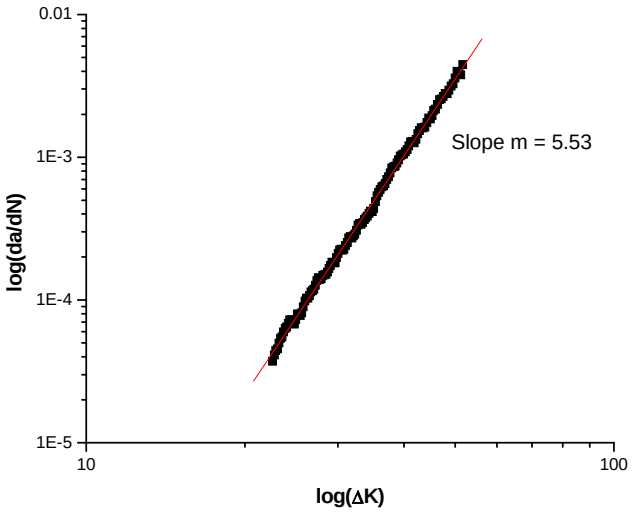

R = 0.2, T = 100ºC (Sample 2)

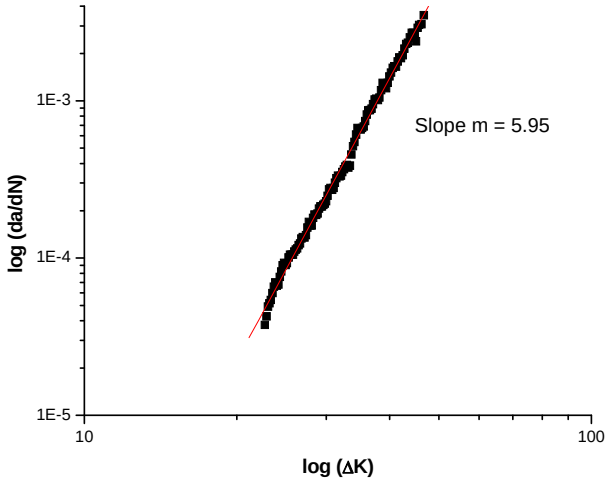

R = 0.3, T = 100ºC (Sample 2)

B3 Ambient-Temperature Constant-K CGR Testing Data

B3.1 da/dN vs. ΔK Plots

B3.1.1 $\Delta K = 23.62$ MPa$\sqrt{m}$

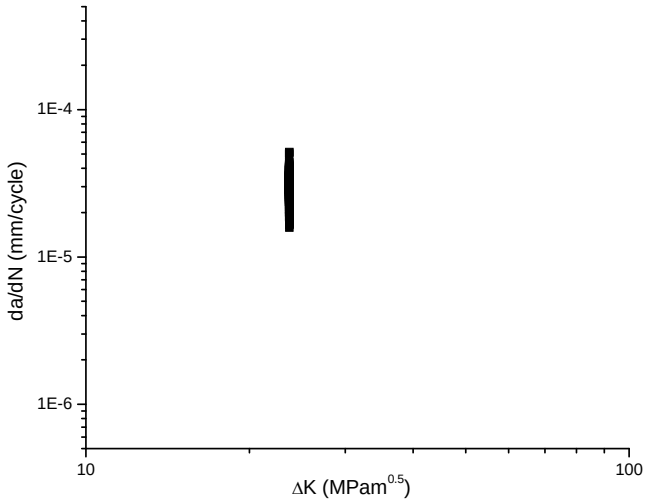

Sample 1

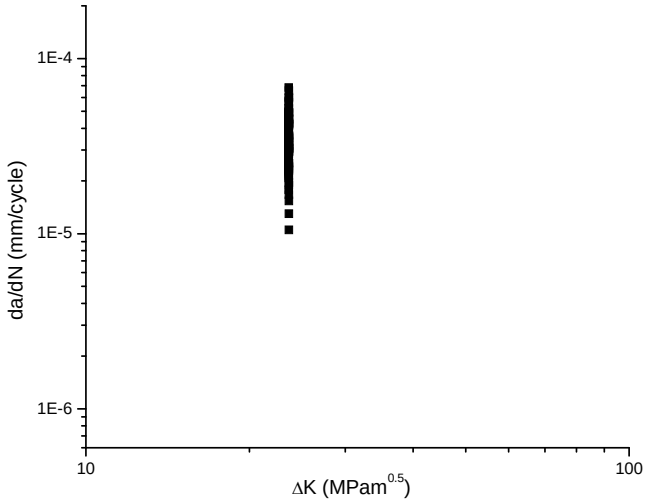

Sample 2

B3.1.2 $\Delta K = 24.87$ MPa$\sqrt{m}$

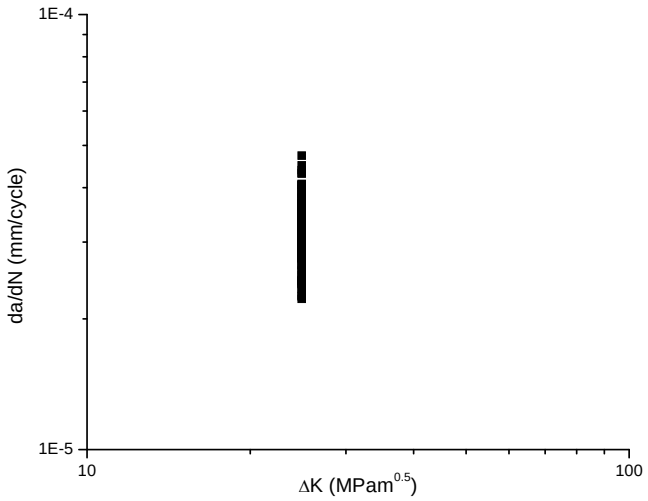

Sample 1

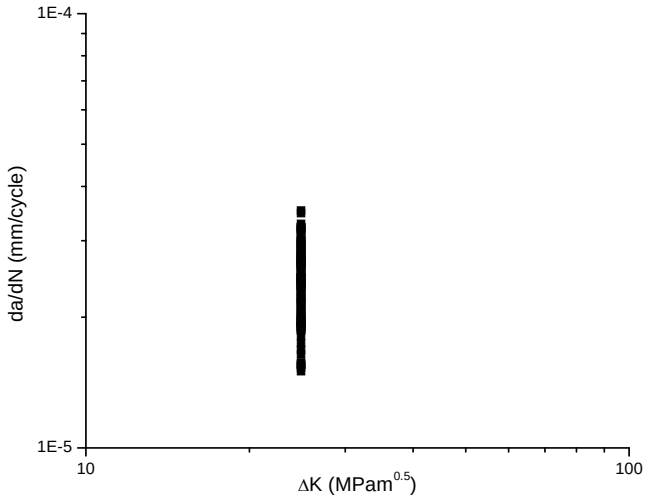

Sample 2

B3.1.3 $\Delta K = 26.17$ MPa$\sqrt{m}$

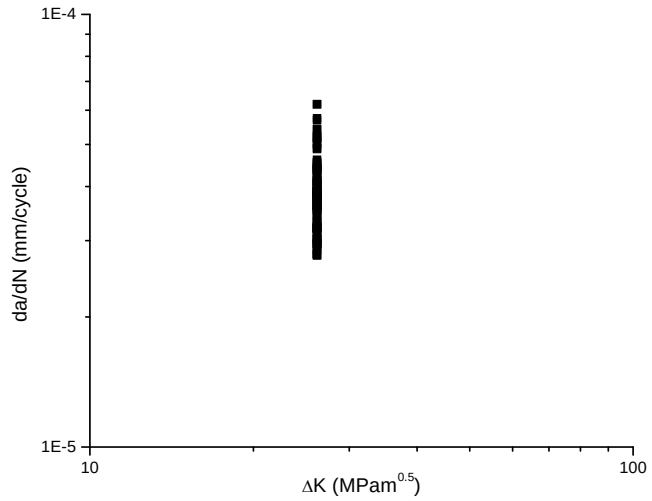

Sample 1

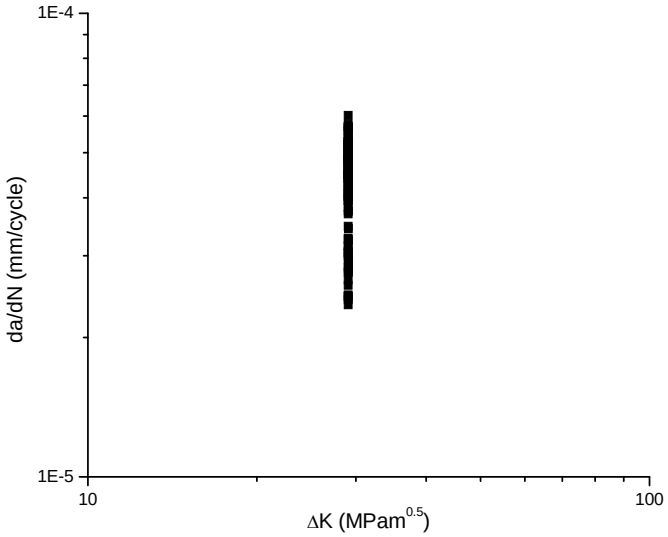

Sample 2

B3.2 Crack-length (a) vs. Number of Cycles (N) Plot

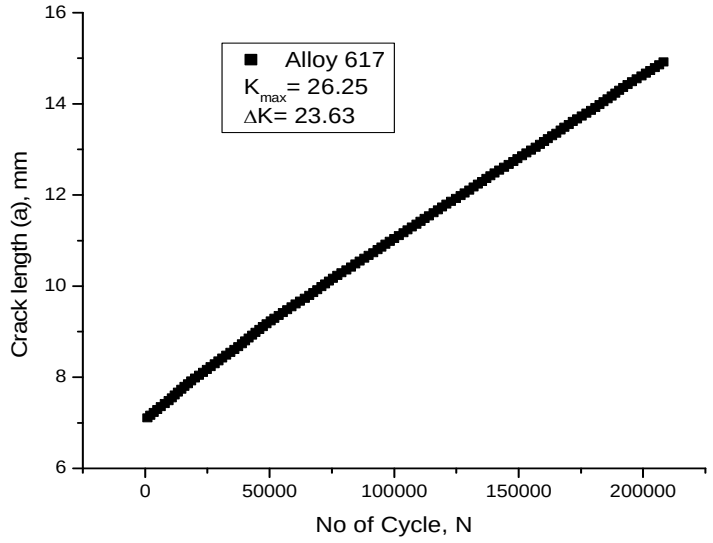

Sample 2

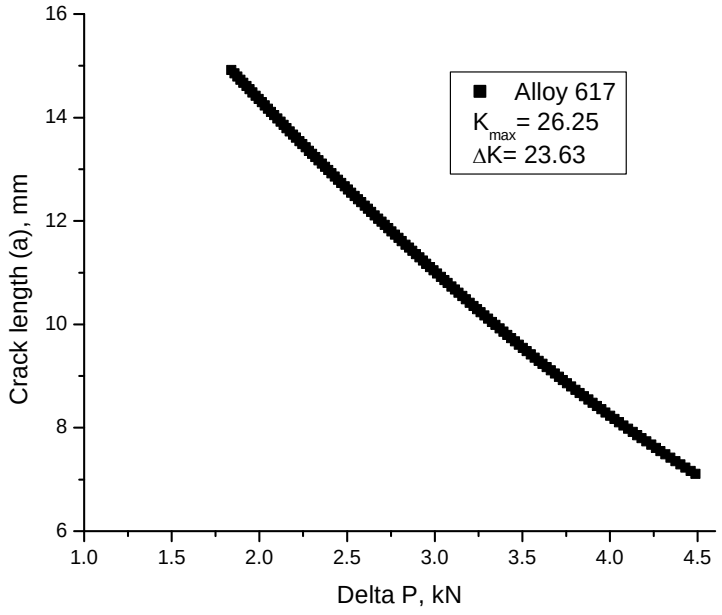

Sample 2

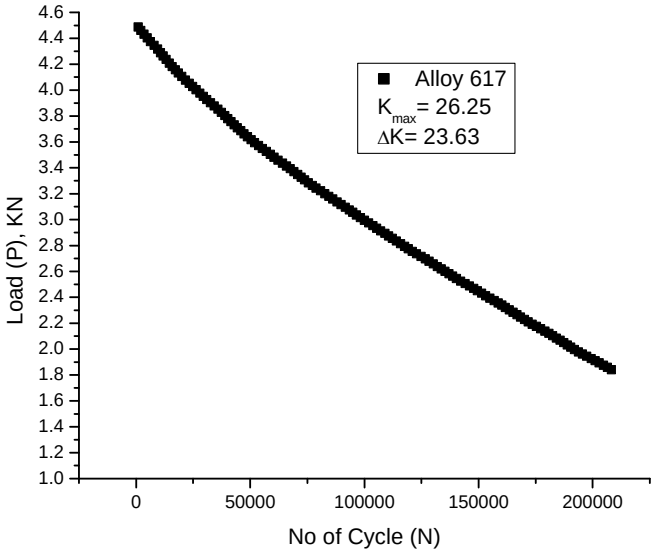
Alloy 617
K_{max} = 26.25
ΔK= 23.63
Load (P), KN
No of Cycle (N)
4.6
4.4
4.2
4.0
3.8
3.6
3.4
3.2
3.0
2.8
2.6
2.4
2.2
2.0
1.8
1.6
1.4
1.2
1.0
0
50000
100000
150000
200000

Sample 2

APPENDIX C

FRACTURE TOUGHNESS TESTING DATA

C1 Fracture Toughness (J_{IC}) Software

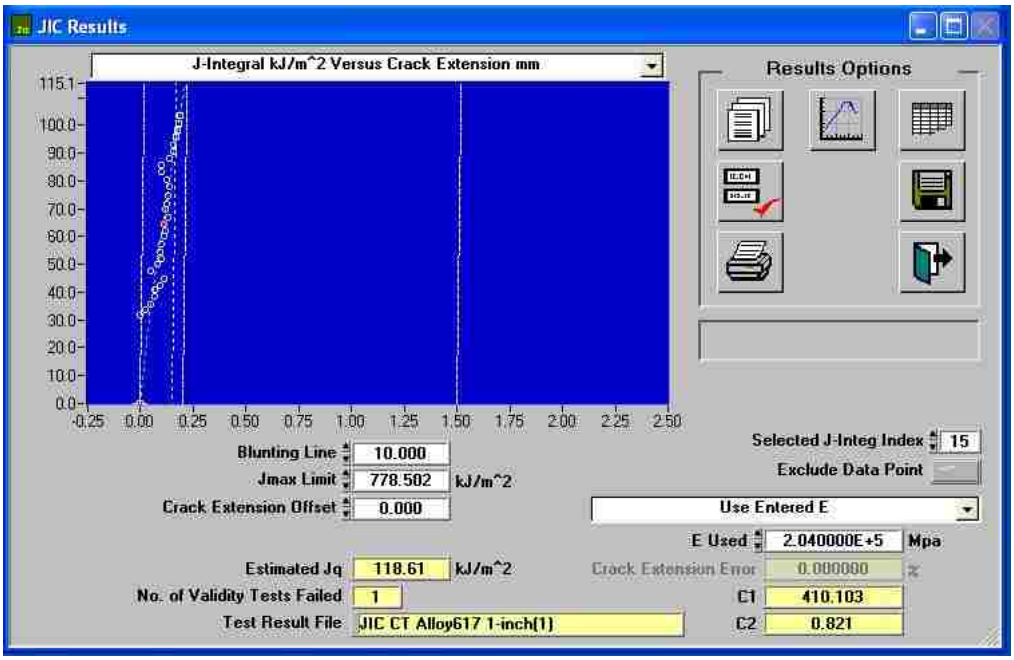

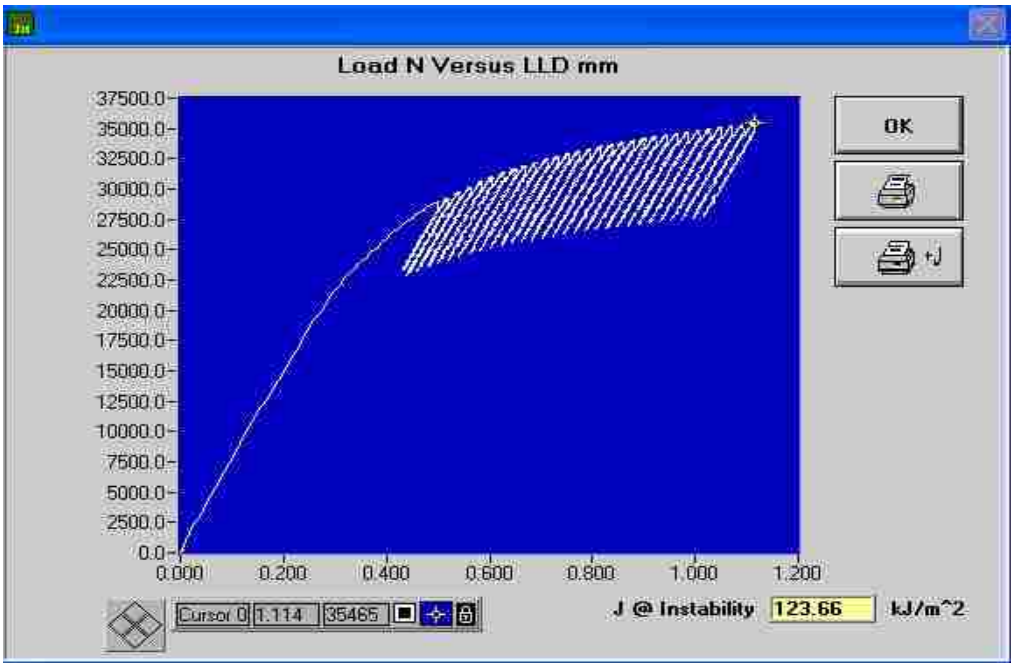

C2 Fracture Toughness (J_{IC}) Values

Temperature (°C)	J_{IC} (KJ/m^2)	
	Sample 1	Sample 2
Room Temperature	118.61	116.2
100	114.10	115.1
200	109.88	110.3
500	109.10	109.7

C3 Fracture Toughness (K_{IC}) and CTOD (δ) Values

Temperature (°C)	K_{IC} (MPa√m)		δ (mm)	
	Sample 1	Sample 2	Sample 1	Sample 2
Room Temperature	163.05	161.07	0.175646	0.17264
100	159.93	158.87	0.204943	0.20421
200	156.94	157.68	0.213334	0.22143
500	156.38	155.29	0.245999	0.25016

C4 Tearing Modulus (T) Values

Temperature (°C)	T	
	Sample 1	Sample 2
Room Temperature	560.23	562.13
100	578.87	576.77
200	588.96	582.24
500	677.60	671.57

APPENDIX D

SCANNING ELECTRON MICROGRAPHS

D1 SEM Micrographs of CT Specimens Tested for da/dN Studies

D1.1 Ambient Temperature, R = 0.2

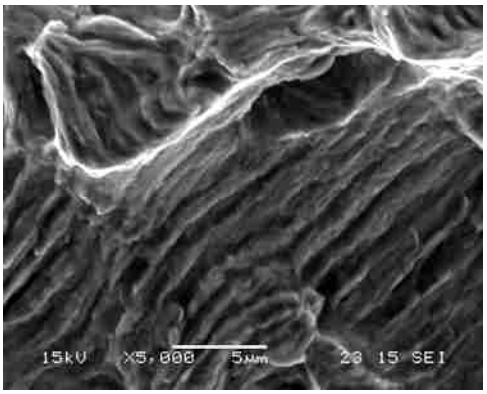

Striations

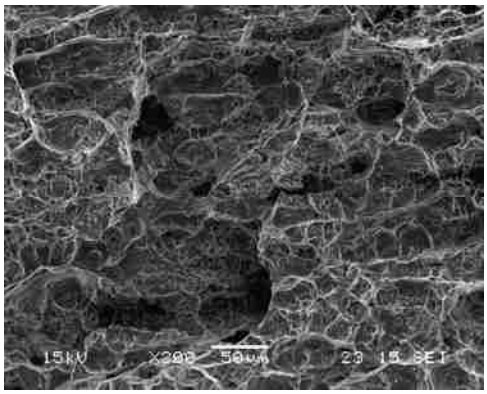

Dimples

D1.2 Ambient Temperature, R = 0.3

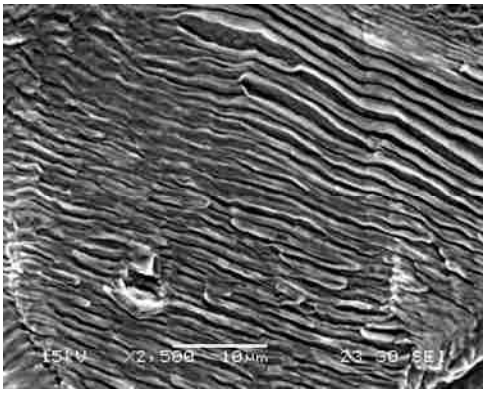

Striations

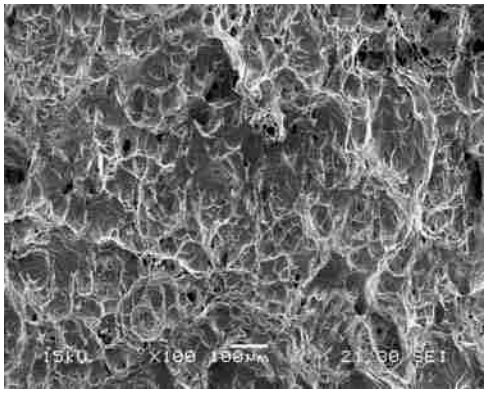

Dimples

D1.3 100 °C, R = 0.1

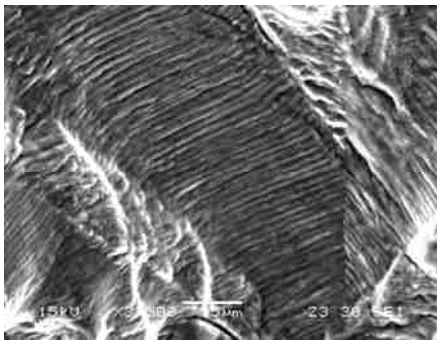

Striations

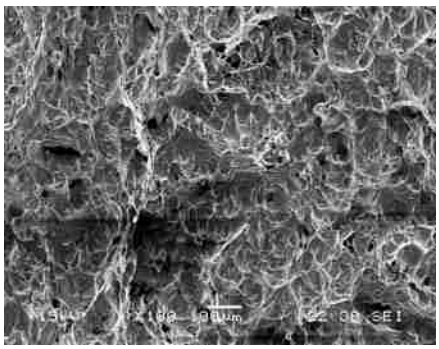

Dimples

D1.4 100 °C, R = 0.2

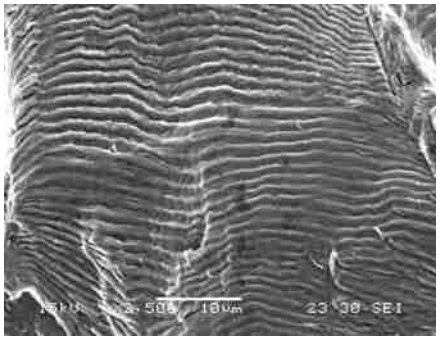

Striations

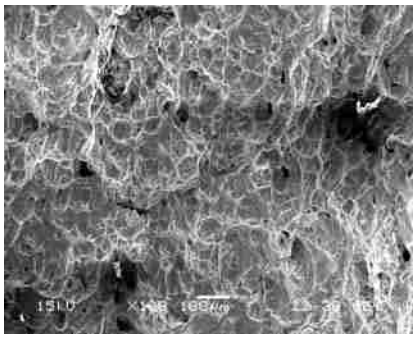

Dimples

D1.5 100 °C, R = 0.3

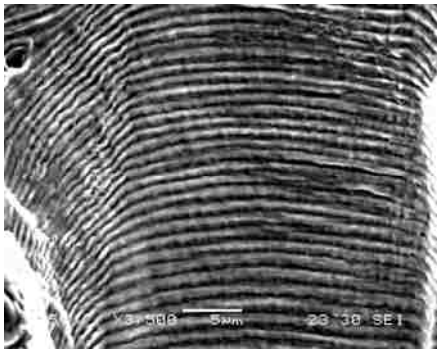

Striations

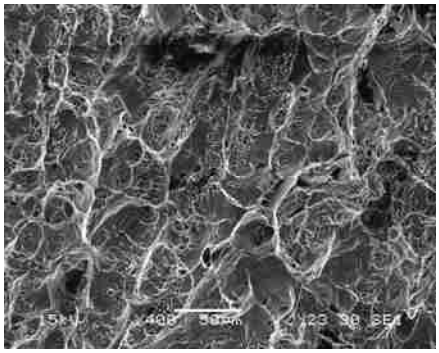

Dimples

D2 SEM Montage Micrographs of DCB Specimens Tested for Variable Exposure Periods

D2.1 2-month Test Duration, High K_I

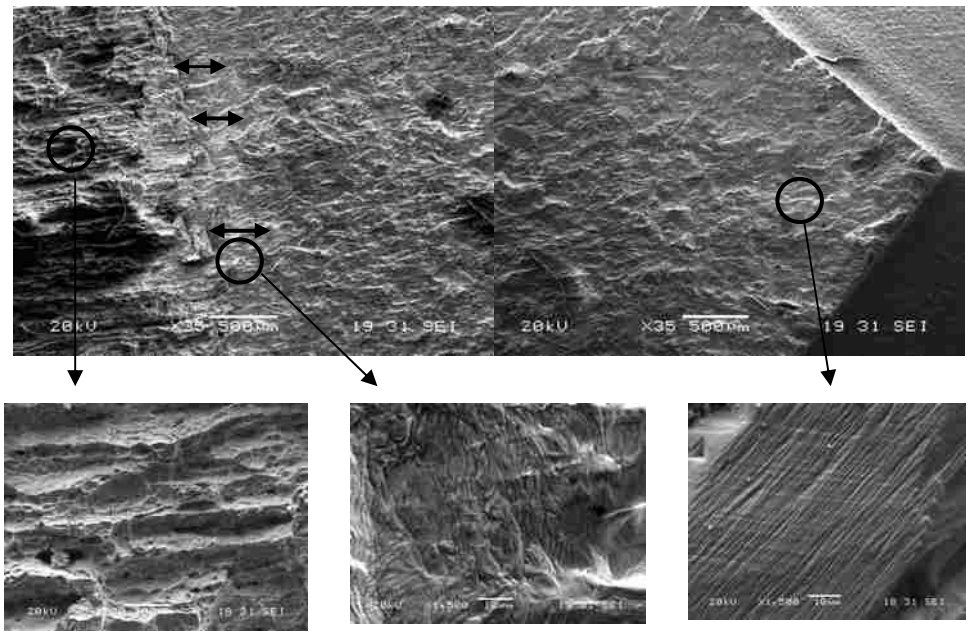

Fast fracture (Dimples) SCC (cleavages) Fatigue Striation

D2.2 2-month Test Duration, Low K_I

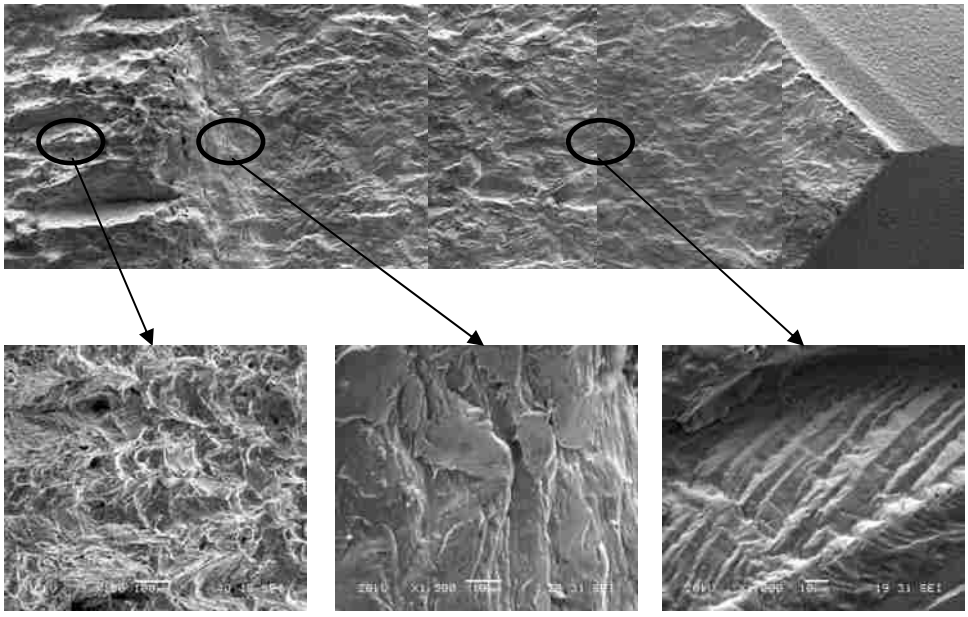

Fast Fracture Region (Dimples) SCC Region (Cleavages) Fatigue Pre-crack Region (Striations)

D2.3 4-months Test Duration, Low K_I

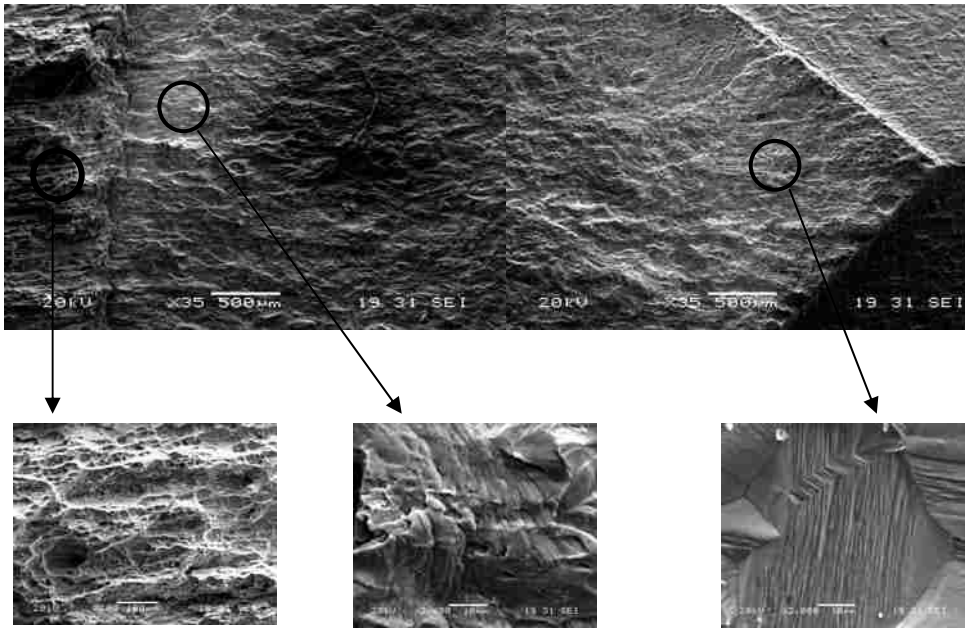

Fast fracture SCC Fatigue

D2.4 4-months Test Duration, High K_I

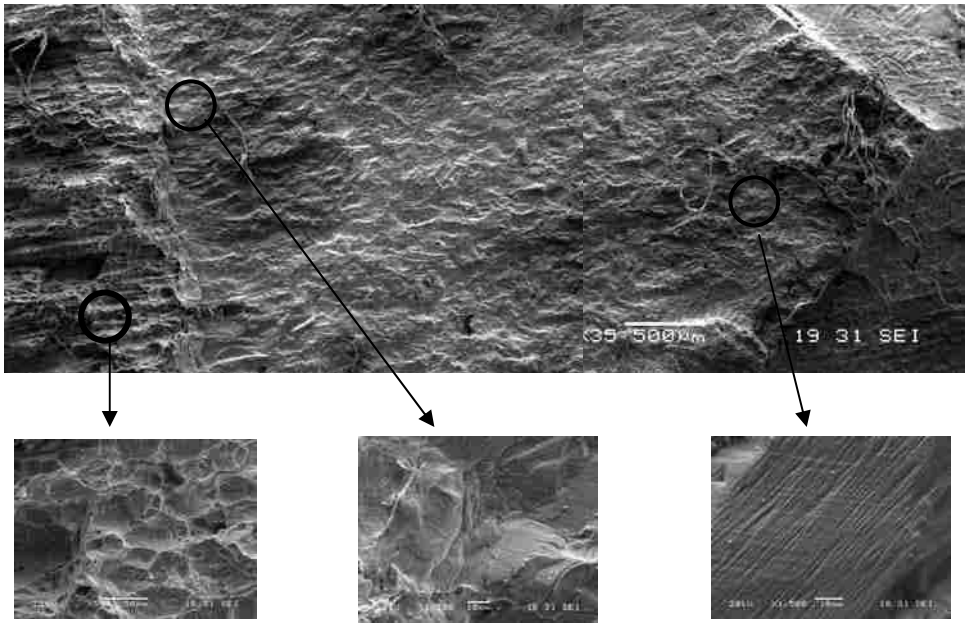

Fast fracture SC Fatigue

D2.5 8-months Test Duration, Low K_I

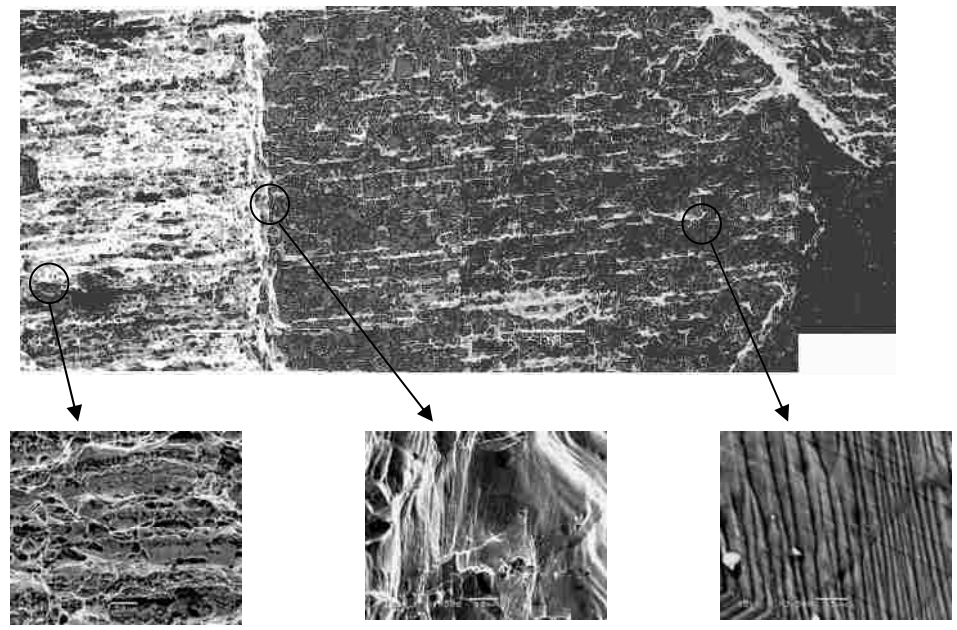

Fast fracture SC Fatigue

D2.6 8-months Test Duration, High K_I

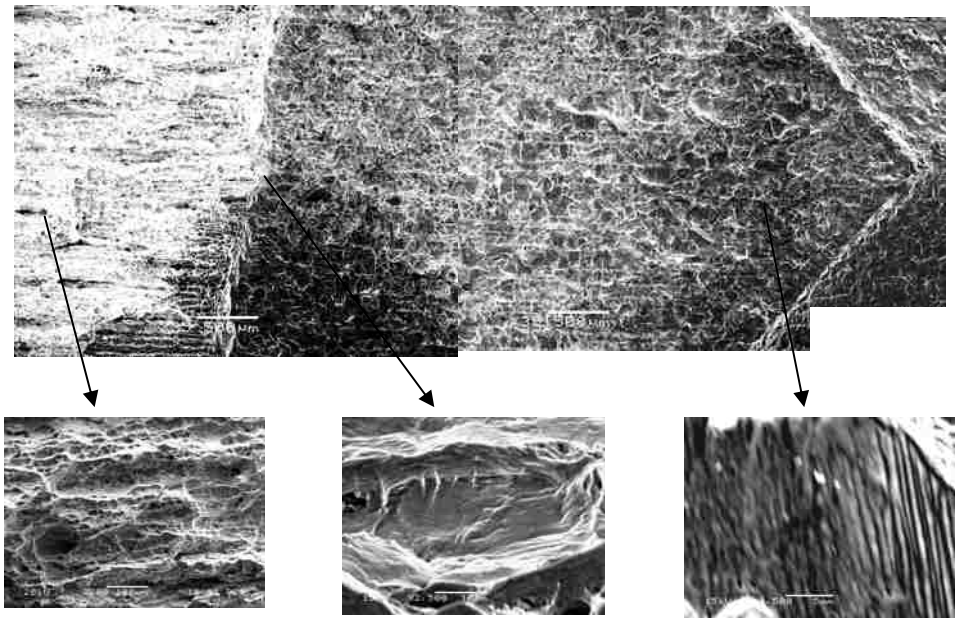

Fast fracture SC Fatigue

APPENDIX E

TRANSMISSION ELECTRON MICROGRAPHS

E1 Bright Field Images Showing Dislocations and Precipitates

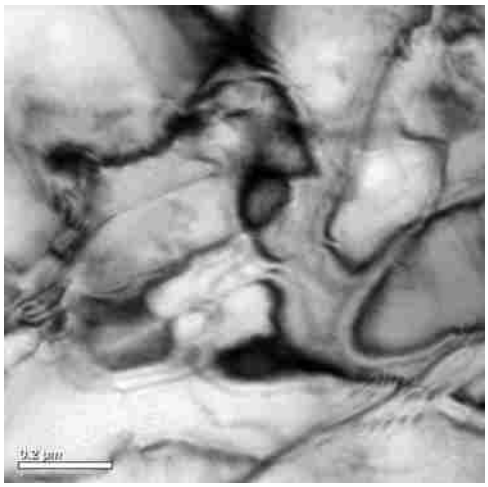

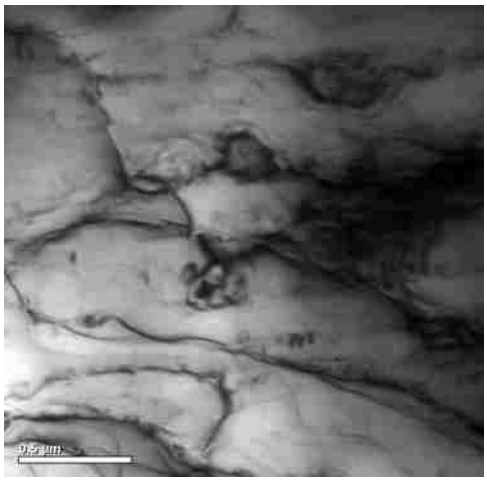

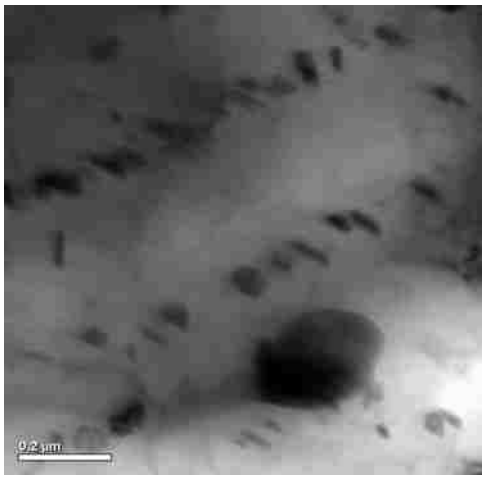

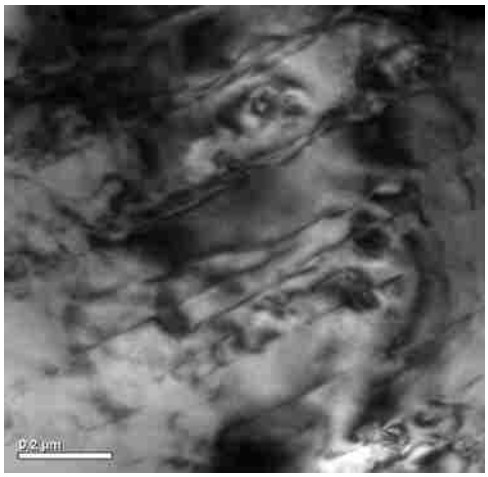

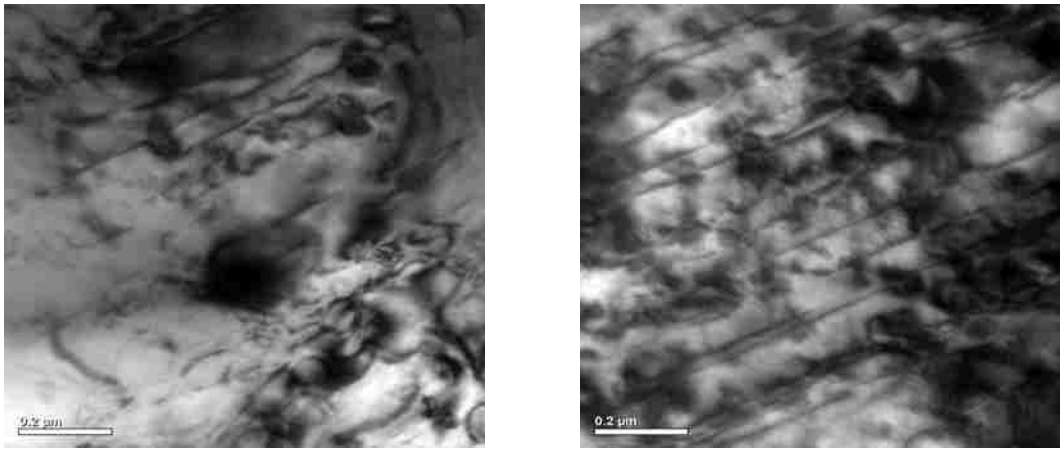

E2 STEM Mode Image Revealing Various Precipitates

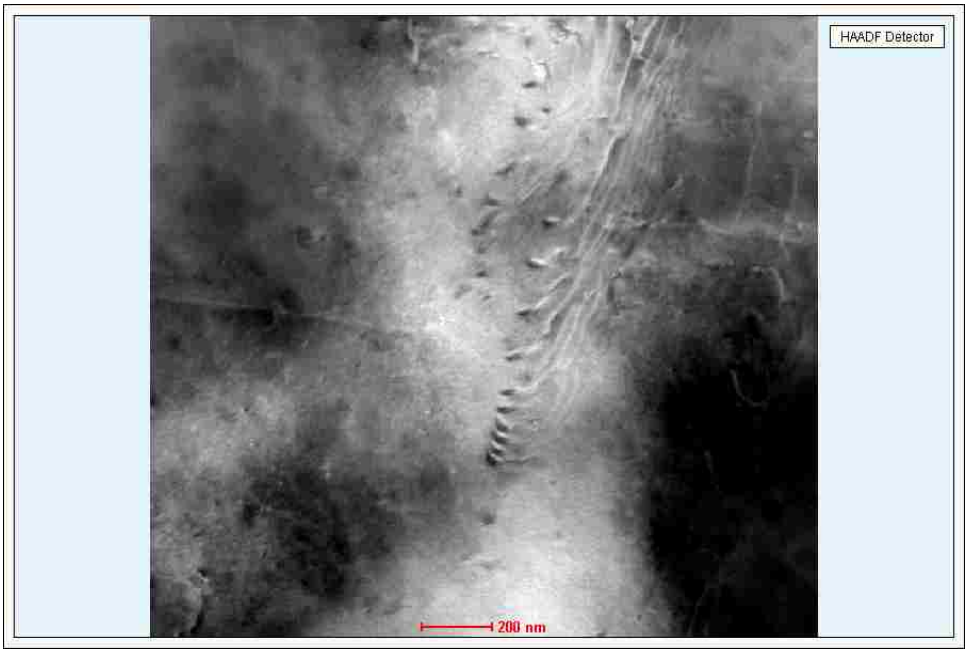

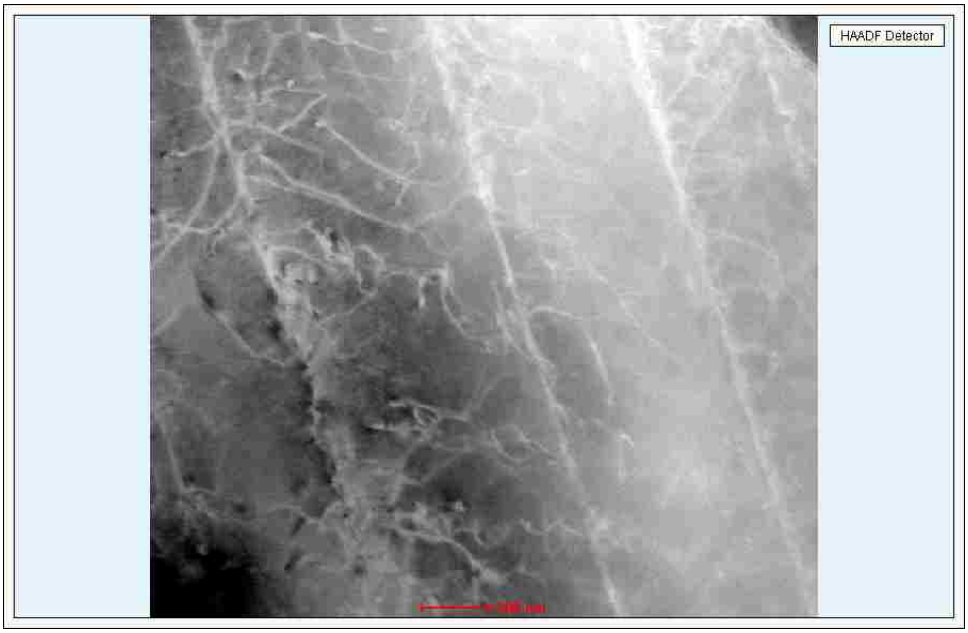
HAADF Detector

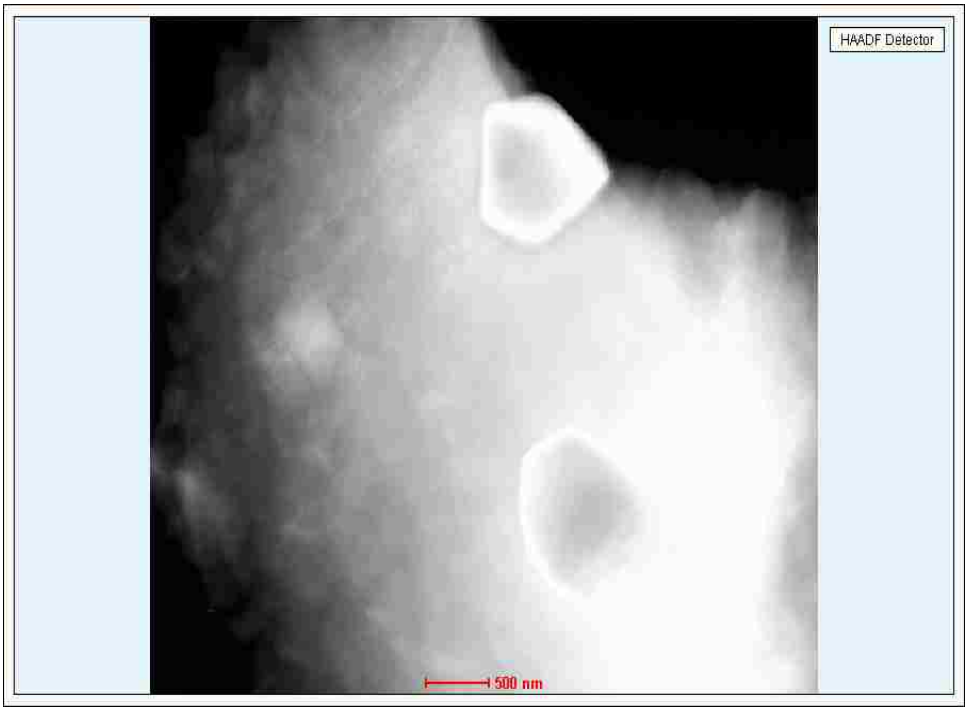
HAADF Detector
500 nm

E3 Elemental analysis at STEM Mode

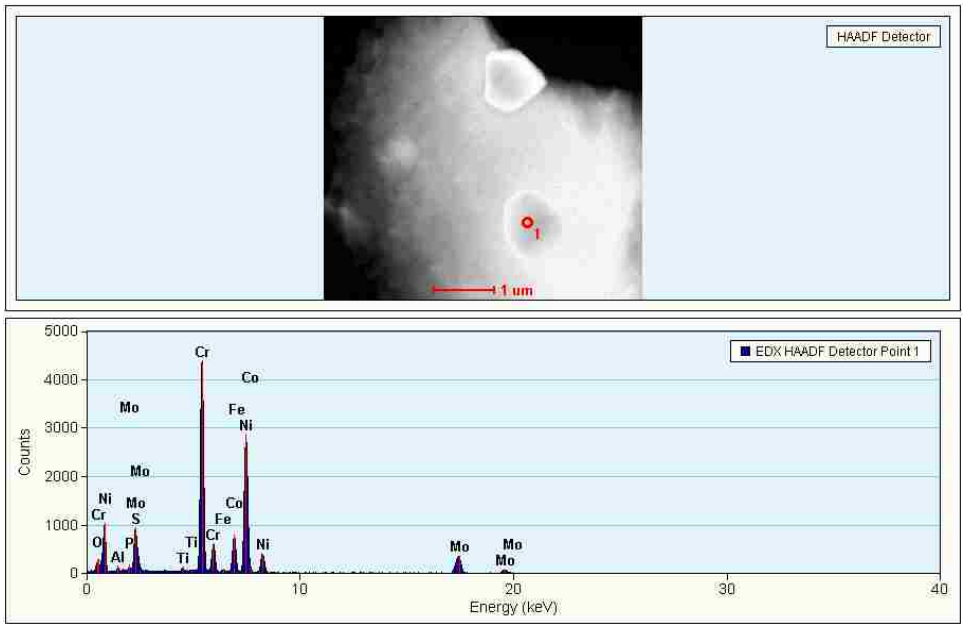

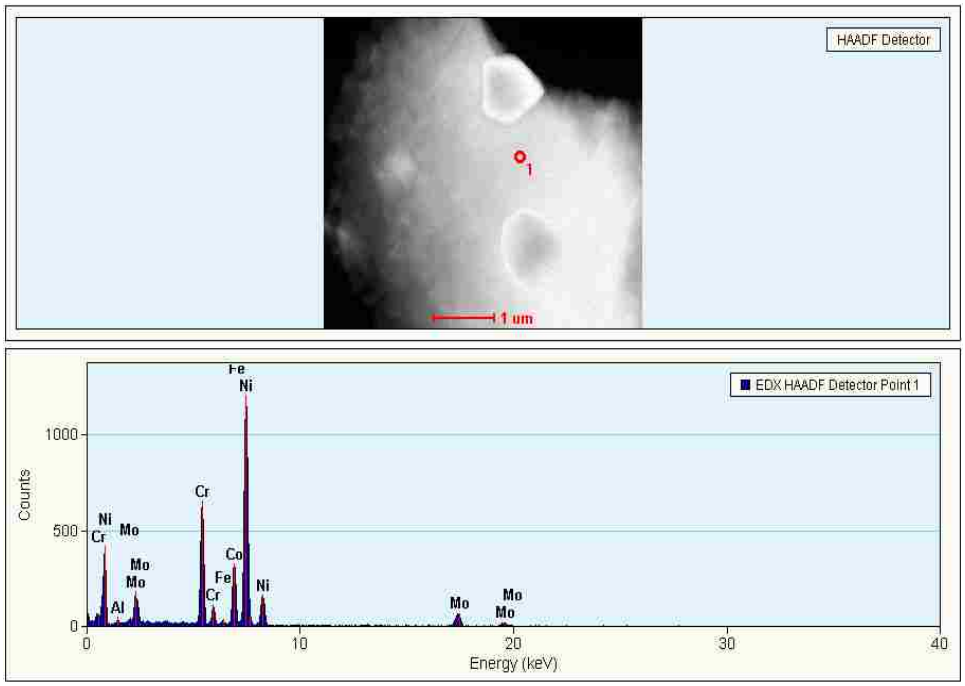

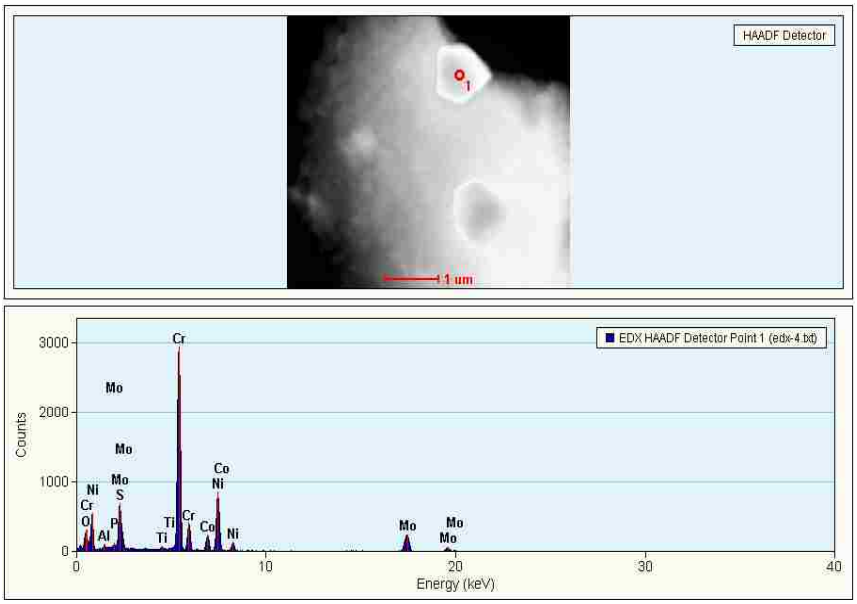
HAADF Detector
1
1 um
EDX HAADF Detector Point 1 (edx-4.txt)
Counts
Energy (keV)
Cr
Mo
Mo
Mo
S
Ni
Cr
O
Al
P
Ti
Ti
Cr
Co
Co
Ni
Ni
Mo
Mo
Mo

APPENDIX F

OPTICAL MICROGRAPHS

F 1 Optical Micrographs of Tested Creep specimens

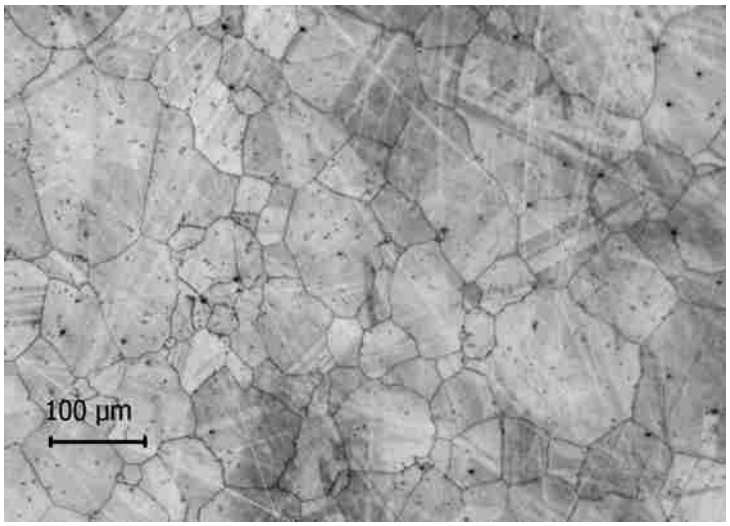

750ºC @0.10YS

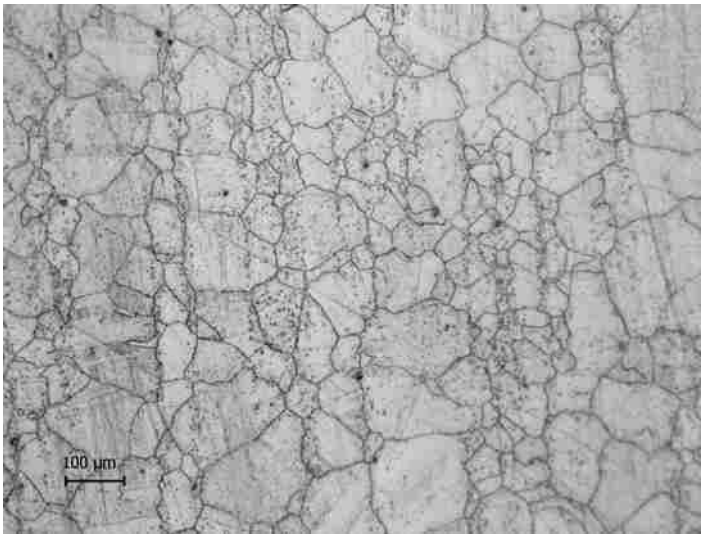

850ºC @ 0.10YS

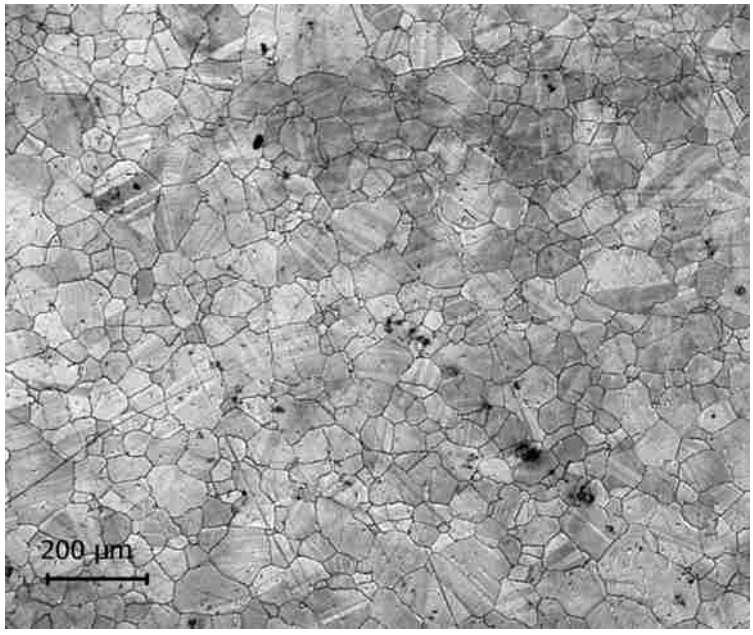

950ºC @0.10YS

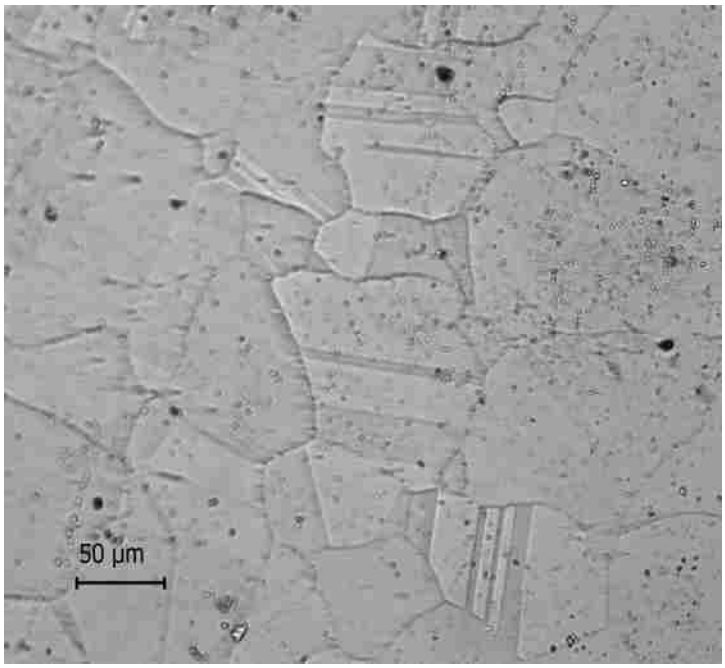

950ºC @0.25YS

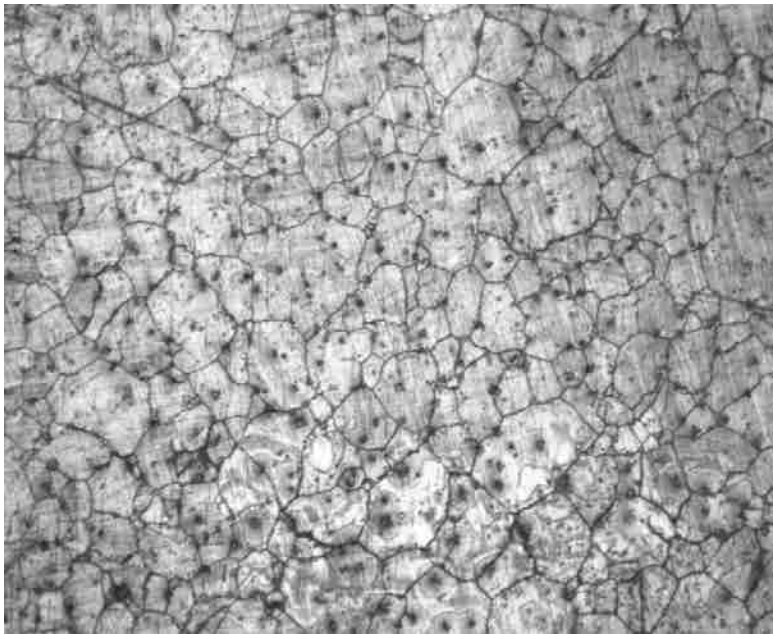

950ºC @0.35YS

APPENDIX G

UNCERTAINTY ANALYSES OF EXPERIMENTAL RESULTS

A precise method of estimating uncertainty in experimental results of CGR testing has been presented by Georgsson [92]. This method is applicable to tests conducted in load control mode at constant-amplitude (using the DCPD technique) and performed under uniaxial loading at ambient temperature.

The combined uncertainty in the results of this investigation was calculated by using the root sum squares equation, given below [92]. This uncertainty corresponds to plus or minus one standard deviation on the normal distribution law representing the studied quantity. This combined uncertainty has an associated confidence level of 68.27%.

$$U_c(y) = \sqrt{\sum_{i=1}^{N}\left[c_i u(x_i)\right]^2} \qquad \text{Equation G-1}$$

where

$U_c(y)$ = Combined uncertainty in the results

c_i = Sensitivity coefficient associated with x_i, usually = 1

The expanded uncertainty (U) was obtained by multiplying the combined uncertainty (U_c) by a coverage factor (k), the value of which was taken as 2 that corresponds to a confidence interval of 95.4% [92, 93]. It is to be noted that all uncertainty calculations in this section are based on a crack length of 0.9 mm for a CT specimen tested at ambient

temperature and a load ratio of 0.1. However, this analysis can be applied to all other crack lengths.

G1 Uncertainty in Crack Length [U(a)]

Sample Calculation:

Standard deviation in crack length error due to PD-variation = $S_{ea} = \pm 3.57$ μm (S_{ea} value was determined from the 'ea' versus 'a' plot, as illustrated in Figure G-1).

Error in crack length = $ea = \left(a_{N+\Delta N} - a_N\right) - \left[\left(\frac{da}{dN}\right) \times \Delta N\right]$

Uncertainty in crack length due to PD variation =

$$u(a)_{PD} = \left(\frac{\delta a}{a}\right)_{PD} = S_{ea} \times d_v = \pm 3.57 \times 1 = \pm 3.57 \text{ μm}$$

Combined uncertainty in crack length =

$$U_c(a) = \sqrt{\sum_{i=1}^{N}\left[c_i u(x_i)\right]^2} = \sqrt{\left[c_{PD} u(a)_{PD}\right]^2} = \sqrt{\left[1 \times 3.57\right]^2} = \pm 3.57 \text{ μm}$$

Expanded uncertainty in crack length =

$U(a) = U_c(a) \times k$

$= \pm 3.57 \times 2$

$= \pm 7.14$ μm

$= \pm 0.00714$ mm

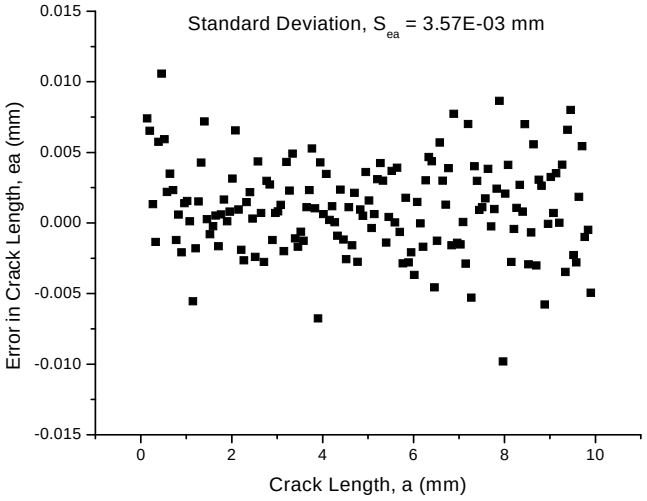

Figure G-1 ea vs. a

G2 Uncertainty in Stress-intensity-factor-range [U(ΔK)]

Sample Calculation:

Following analysis is based on ΔK = 21.04 MPa√m, corresponding to crack length of 0.9 mm.

G2.1 Uncertainty due to Alignment $[u(\Delta K)_a]$

Uncertainty in Instron alignment = ea = ±5% = ±0.05

$$u(\Delta K)_a = \left(\frac{\delta \Delta K}{K}\right)_a = \Delta K \times ea \times d_v = 21.04 \times \pm 0.05 \times 0.5 = \pm 0.526 \text{ MPa}\sqrt{m}$$

G2.2 Uncertainty due to Load Cell $[u(\Delta K)_l]$

Uncertainty in Instron load cell = ea = ±0.25% = ±0.0025

$$u(\Delta K)_l = \left(\frac{\delta \Delta K}{K}\right)_l = \Delta K \times ea \times d_v = 21.04 \times \pm 0.0025 \times 0.5 = \pm 0.0263 \text{ MPa}\sqrt{m}$$

Combined uncertainty in ΔK =

$$U_c(\Delta K) = \sqrt{\sum_{i=1}^{N}\left[c_i u(x_i)\right]^2} = \sqrt{\left[c_a u(\Delta K)_a\right]^2 + \left[c_l u(\Delta K)_l\right]^2}$$

$$= \sqrt{\left[1 \times 0.526\right]^2 + \left[1 \times 0.0263\right]^2} = \pm 0.527 \text{ MPa}\sqrt{\text{m}}$$

Expanded uncertainty in ΔK =

$U(\Delta K) = U_c(\Delta K) \times k$

$= \pm 0.527 \times 2$

$= \pm \underline{1.054 \text{ MPa}\sqrt{\text{m}}}$

G3 Uncertainty in da/dN [U(da/dN)]

Sample Calculation:

$$\frac{da}{dN} = \frac{\Delta a}{\Delta N} = \frac{\Delta a}{N_{average,(a=0.9mm)} - N_{average,(a=0.83mm)}} = \frac{0.9 - 0.83}{100472.8 - 97881} = 2.7 \times 10^{-5} \text{ mm/cycle}$$

$$\left(\frac{da}{dN}\right)_{S_N} = \frac{\Delta a}{\Delta N - S_N} = \frac{0.9 - 0.83}{\left(100472.8 - 97881\right) - 10145.445} = -9.3 \times 10^{-6} \text{ mm/cycle}$$

Error in da/dN =

$$u\left(\frac{da}{dN}\right) = \delta\left(\frac{da}{dN}\right) = \left[\left(\frac{da}{dN}\right)_{S_N} - \left(\frac{da}{dN}\right)\right] \times d_v$$

$$= \left[\left(-9.3 \times 10^{-6}\right) - \left(2.7 \times 10^{-5}\right)\right] \times 0.5$$

$$= \pm 1.815 \times 10^{-5} \text{ mm / cycle}$$

Combined uncertainty in da/dN =

$$U_c\left(\frac{da}{dN}\right) = \sqrt{\sum_{i=1}^{N}\left[c_i u(x_i)\right]^2} = \sqrt{\left[c \times u\left(\frac{da}{dN}\right)_a\right]^2}$$

$$= \sqrt{\left[1 \times (1.815 \times 10^{-5})\right]^2}$$

$$= \pm 1.815 \times 10^{-5} \text{ mm/cycle}$$

Expanded uncertainty in da/dN =

$U(da/dN) = U_c(da/dN) \times k$

$= \pm(1.815 \times 10^{-5}) \times 2$

$= \pm\underline{3.63 \times 10^{-5} \text{ mm/cycle}}$

BIBLIOGRAPHY

1. "A National Vision of America's Transition to a Hydrogen Economy into 2030 and Beyond" National Hydrogen Vision Meeting document, US Dept. of Energy, February 2002
2. Mike Campbell and Ken Schultz "Fusion as a Source for Hydrogen Production" 13 December 2004, 25th Annual Fusion Power Associates Meeting
3. C. W. Forsberg and K. L. Peddicord: Hydrogen Production as a Major Nuclear Energy Application, Nuclear News, September 2001
4. Paul M. Mathias and Lloyd C. Brown "Thermodynamics of the Sulfur-Iodine Cycle for Thermochemical Hydrogen Production" Japan March 2003, 68th Annual Meeting of the Society of Chemical Engineers, Japan The University of Tokyo
5. L. C. Brown, G. E. Besenbruch, R. D, Lentsch "High Efficiency Generation of Hydrogen Fuels using Nuclear Power" Technical Report December 2003, Nuclear Energy Research Initiative (NERI) Program
6. "The Hydrogen Economy: Opportunities, Costs, Barriers, and R&D Needs", The National Academies Press, Washington DC
7. G.E. Besenbruch: General Atomic "Sulfur-Iodine Thermochemical Water-Splitting Process" American Chemical Society, Division of Petroleum Chemistry, 271, 48 (1982)

8. W. Xinxin, O. Kaoru, “Thermochemical Water Splitting for Hydrogen Production Utilizing Nuclear Heat from an HTGR”, Tsinghua Science and Technology, vol. 10, n. 2, 2005, pp. 270-276.
9. W. Ren, R. Swindeman, “Preliminary Consideration of Alloys 617 and 230 for Generation IV Nuclear Reactor Applications” Proceedings of 2007 ASME Pressure Vessels and Piping Division Conference, July 22-26, 2007, San Antonio, TX, USA
10. H. Nakajima, M. Sakurai, K. Ikenoya, G. J. Hwong, K. Onuki, S. Shimizu, “A study on a closed-cycle hydrogen production by thermochemical water-splitting IS process” Proceedings of the Seventh International Conference on Nuclear Engineering (ICONE-7), Tokyo, April 1999. ICONE-7104
11. “A technology Roadmap for Generation IV Nuclear Energy Systems, US DOE Nuclear Energy Research Advisory Committee and the Generation IV International Forum,” December 2002
12. A. K. Roy, V. Virupaksha, “ Performance of Alloy 800H for High Temperature Heat Exchanger Applications”, Materials Science and Engineering A, 452-453, 2007, pp. 665-672
13. Yelavarthi, Jagadesh K., “High-temperature deformation and environment-induced degradation of Waspaloy.”, M.S. thesis, University of Nevada, Las Vegas, United States – Nevada, 2006
14. V. Virupaksha, “Use of alloy 800H for applications in hydrogen generation using nuclear power.”, M.S. thesis, University of Nevada, Las Vegas, United States, 2006

15. Special Metals Corporation, “Technical Bulletin – Inconel Alloy-617”, Products – Alloy Portfolio
16. F. Jalilian, M. Jahazi, R. A. L. Drew, “Microstructural evolution during transient liquid phase bonding of Inconel 617 using Ni-Si-B Filler Metal”, Materials Science and Engineering A, 426, 2006, 269-281
17. Y. Sakai, T. Tanabe, T. Suzuki, H. Yoshida, “Corrosion Behavior of Inconel 617 in a Simulated HTGR Helium”, Transactions of National Research Institute for Metals, vol. 27, 1985, pp. 20-27
18. U. Bruch, D. Schumacher, P. Ennis, E. Heesen, “Tensile and Impact Properties of Candidate Alloys for High-Temperature Gas-Cooled Reactor Applications”, Nuclear Technology, vol. 66, 1984, pp. 357-362
19. B. S. Rao, H. P. Meurer, H. Schuster, “Creep-Fatigue Interaction of Inconel 617 at 950°C in Simulated Nuclear Reactor Helium”, Materials Science and Engineering, A104, 1988, pp. 37-51
20. R. N. Wright, “Summary of Studies of Ageing and Environmental Effects on Inconel 617 and Haynes 230”, NGNP Materials Research and Development Program Report, Idaho National Laboratory, September 2006
21. T. C. Totemeier, H. Tian, “Creep-fatigue-environment interactions in INCONEL 617”, Materials Science and Engineering A, 468-470, 2007, pp. 81-87
22. T. S. Jo, G. S. Kim, Y. I. Seo, W. S. Ryu, Y. D. Kim, “Microstructure and High Temperature Mechanical Properties of Inconel 617”, Materials Science Forums, vol. 544-545, 2007, pp. 411-414

23. P. Ganesan, G. D. Smith, D. H. Yates, “Performance of Inconel 617 in Actual and Simulated Gas Turbine Environments”, Materials and Manufacturing Processes, vol. 10, no. 5, 1995, pp. 925-938
24. H. Fathollahnejad, B.-H. Tsao, R. Ponnappan, D. Jacobson, “Post-Test Corrosion Analysis of High-Temperature Thermal Energy Storage Capsules”, Journal of Materials Engineering and Performance, vol. 2, no. 1, 1993, 125-134
25. P. S. Korinko. “High temperature environmental interactions of Inconel 617: A paper study for the TEF”, Technical Report, WSRC-TR-2000-00136, June 16, 2007, Westinghouse Savannah River Company, Aiken, SC
26. T. Shikama, T. Tanabe, M. Fujitsuka, M. Kitajima, H. Yoshida, R. Watanabe, “Corrosion Behaviors of Inconel 617 in Hydrogen Gas Mixture”, Metallurgical and Materials Transactions A, vol. 11 A, no. 9, 1980, pp. 1589-1598
27. K. Natesan, A. Purohit, S. W. Tam, “Materials behavior in HTGR Environments”, U. S. Nuclear Regulatory Commission Report, July 2003, Washington DC
28. J. Farzad, “The influence of process parameters on TLP bonding of Inconel 617 Superalloy”, Ph.D. Dissertation, McGill University, Montreal, Canada, 2006
29. R. Wilkenhoener, H. P. Buchkremer, D. Stoever, D. Stolten, A. Koch, “Brazing of Metallic Conductors onto Ceramic Plates in Solid Oxide Fuel Cells Part II Attaching Conducting Wires”, Journal of Materials Science, vol. 36, no. 7, 2001, pp. 1783-1788
30. R. K. Clark, J. Unnam, “Response of Inconel 617 Superalloy to Combined Ground-Based and STS Reentry Exposure”, American Institute of Aeronautics

and Astronautics 19th Thermophysics Conference, June 25-28, 1984 Snowmass, CO

31. H. J. Penkalla, J. Woski, W. Fischer, F. Schubert, "Structural Investigations of Candidate Materials for Turbine Disc Applications Beyond 700°C", Superalloys 718, 625, 706 and Various Derivatives, 2001 The Minerals, Metals and Materials Society
32. Vikram Marthandam, "Tensile Deformation, Toughness and Crack Propagation Studies of Alloy 617", Ph.D. Dissertation, Mechanical Engineering, April 10, 2008.
33. R. J. Bishop, R. E. Smallman, "Strengthening and Toughning", Modern Physical Metallurgy and Materials Engineering, Chapter 8, Butterworth and Heinemann, 6th Edition, 1999
34. Larson, F.R.; and Miller, James: A Time-Temperature Relationship for Rupture and Creep Stresses. Trans. ASME, vol. 74, no. 5, pp. 765−775, July 1952.
35. R. J. Bishop, R. E. Smallman, "Strengthening and Toughning", Modern Physical Metallurgy and Materials Engineering, Chapter 8, Butterworth and Heinemann, 6th Edition, 1999
36. "http://corrosion-doctors.org/MatSelect/corrstainsteel.htm", Stainless Steel Corrosion, *Corrosion Doctors*, Working Link, September 30, 2009.
37. Shigemitsu kihara, J. B. Newkirk and al., "Morphological changes of carbides during creep and their effects on the creep properties of Inconel 617 at 1000^0C," AIME, Vol.11A, June 1980-1019.

38. ASTM Designation E 647-00, "Standard Test Method for Measurement of Fatigue Crack Growth Rates," *American Society for Testing and Materials (ASTM) International*, West Conshohocken, PA, 2004.
39. ASTM Designation E 813-89, "Standard Test Method for J_{IC}, A Measure of Fracture Toughness," *American Society for Testing and Materials (ASTM) International,* West Conshohocken, PA, 1989.
40. NACE Standard TM0177-90, "NACE Standard Double-Cantilever-Beam Test, Method D," *NACE International*, Houston, TX, 1990, pp. 17–22.
41. ASTM Designation E 139-00, "Standard Test Methods for Conducting Creep, Creep-Rupture, and Stress-Rupture Tests of Metallic Materials," *American Society for Testing and Materials (ASTM) International*, West Conshohocken, PA, 2004.
42. ASTM Designation E 139-06, "Standard Test Methods for Conducting Creep, Creep-Rupture, and Stress-Rupture Tests of Metallic Materials," *American Society for Testing and Materials (ASTM) International*, West Conshohocken, PA, 2006.
43. G. E. Dieter, "Mechanical Metallurgy," 3rd Edition, Publisher: *McGraw-Hill*, NY, 1986.
44. "http://www.doitpoms.ac.uk/tlplib/creep/intro.php," Creep Deformation of Metals – Introduction, DoITPoMS Teaching and Learning Packages, *University of Cambridge*, Working Link, September 30, 2009.

45. "http://www.metallurgy.nist.gov/solder/clech/Report_Images/Figure_1.png," Materials Science and Engineering Laboratory, *The National Institute of Standards and Technology (NIST)*, Working Link, September 30, 2009.
46. P. S. Shankar and K. Natesan, "Effect of Trace Impurities in Helium on the Creep Behavior of Alloy 617 for Very High Temperature Reactor Applications," *Journal of Nuclear Materials*, Vol. 366(1-2), 2007, pp. 28-36.
47. ASTM Designation E 647-00, "Standard Test Method for Measurement of Fatigue Crack Growth Rates," *American Society for Testing and Materials (ASTM) International*, West Conshohocken, PA, 2004.
48. "http://www.instron.us/wa/products/fatigue_testing/electric_actuator.aspx," Specifications of Model 8862, Dynamic and Fatigue Test Systems – High Precision Electric Actuator Systems, *Instron Corporation*, Working Link, September 30, 2009.
49. . A. K. Roy, J. Pal and M. H. Hasan, "Temperature and Load Ratio Effects on Crack-Growth Behavior of Austenitic Superalloys," *Journal of Engineering Materials and Technology*, Vol. 132(1), 2010.
50. Q. Peng, S. Teysseyre and G. S. Was, "Stress Corrosion Crack Growth in 316 Stainless Steel in Supercritical Water," *3rd International Symposium on Supercritical Water-Cooled Reactors-Design and Technology*, Shanghai, China, 2007.
51. G. A. Hartman and D. A. Johnson, "D-C Electric-Potential Method Applied to Thermal/Mechanical Fatigue Crack Growth," *Experimental Mechanics*, Vol. 27(1), 1987, pp. 106-112.

52. N. Merah, "Detecting and Measuring Flaws using Electric Potential Techniques," *Journal of Quality in Maintenance Engineering*, Vol. 9(2), 2003, pp. 160-175.

53. *Fracture Technology Associates*, "Automated Fatigue Crack Growth Testing and Analysis Software," Version 3.09, Series 2001, Bethlehem, PA, 2001.

54. H. H. Johnson, "Calibration of Electric Potential Method for Studying Slow Crack Growth," *Materials Research Standards*, Vol. 5(9), 1965, pp. 442-445.

55. P. C. McKeighan and D. J. Smith, "Determining the Potential Drop Calibration of a Fatigue Crack Growth Specimen subject to Limited Experimental Observations," *Journal of Testing and Evaluation*, Vol. 22(4), 1994, pp. 291-301.

56. Y. L. Lu et al., "Effects of Temperature and Hold Time on Creep-Fatigue Crack-Growth Behavior of Haynes 230 Alloy," *Materials Science and Engineering A*, 429, 2006, pp. 1-10.

57. P. K. Liaw, A. Saxena and J. Schaefer, "Creep Crack Growth Behavior of Steam Pipe Steels: Effects of Inclusion Content and Primary Creep," *Engineering Fracture Mechanics*, Vol. 57(1), 1997, pp. 105-130.

58. P. C. Paris and F. Erdogan, "A Critical Analysis of Crack Propagation Laws," *Journal of Basic Engineering (Trans. ASME)*, Vol. 85(4), 1963, pp. 528-534.

59. J. A. Newman, "The Effects of Load Ratio on Threshold Fatigue Crack Growth of Aluminum Alloys," Ph.D. Dissertation, Department of Engineering Mechanics, *Virginia Polytechnic Institute and State University,* Fall 2000.

60. J. Mallory, "Fatigue Crack Growth in 2324 Aluminum Alloy," *Journal of Young Investigators*, Vol. 15(5), 2006.

61. R. W. Hertzberg, "Deformation and Fracture Mechanics of Engineering Materials," 4th Edition, Publisher: *John Wiley & Sons, Inc*, NJ, 1996.

62. K. B. Yoon, T. G. Park and A. Saxena, "Elevated Temperature Fatigue Crack Growth Model for DS-GTD-111," *Strength, Fracture and Complexity*, Vol. 4(1), 2006, pp. 35-40.

63. T. Yokobori and T. Aizawa, "The Influence of Temperature and Stress Intensity Factor upon the Striation Spacing and Fatigue Crack Propagation Rate of Aluminum Alloy," *International Journal of Fracture*, Vol. 9(4), 1973, pp. 489-491.

64. T. Yokobori, A. T. Yokobori, Jr. and A. Kamei, "Dislocation Dynamics Theory for Fatigue Crack Growth," *International Journal of Fracture*, Vol. 11(5), 1975, pp. 781-788.

65. T. Yokobori, S. Konosu and A. T. Yokobori, Jr., "Micro and Macro Fracture Mechanics Approach to Brittle Failure and Fatigue Crack Growth," *Fracture 1977*, Vol. I(ICF4), Waterloo, Canada, 1977, pp. 665-682.

66. *Instron Corporation*, "Fast Track 2 – J_{IC} Unloading Compliance Software,"

67. "Nonlinear Fracture toughness Testing" Structural Intregrity Associates Inc., Technical Paper, San Jose, CA.

68. B.K. Neale, "The Fracture Toughness Testing of Center-Cracked Tensile Specimens using the Unloaded Compliance Techniques," Engineering Fracture Mechanics, Vol 59940, 1998, pp.487-499.

69. J.E. Ipinaa et al., "Fracture Toughness in Metal Matrix Composites," Materials Research, Vol 3(3), 2000, pp.74-78.

70. "http://www.efunda.com/formulae/solid_mechanics/fracture_mechanics/fm_epfm_CTOD.cfm," *efunda engineering fundamentals*, Working Link, September 30, 2009.

71. P. C. Paris et al., "The Theory of Instability of the Tearing Mode of Elastic-Plastic Crack Growth," *Elastic-Plastic Fracture (ASTM STP)*, Vol. 668, 1979, pp. 5-36.

72. A. Martinelli and S. Venzi, "Tearing Modulus, J-Integral, CTOA and Crack Profile Shape obtained from the Load-Displacement Curve only," *Engineering Fracture Mechanics*, Vol. 53(2), 1996, pp. 263-277.

73. M. A. Shabara and M. D. Al-Ansary, "Tearing Modulus Analysis for Cracked Plates under Biaxial Loading," *International Journal of Pressure Vessels and Piping,* Vol. 64(2), 1995, pp. 111-117.

74. A. K. Roy et al., "Stress Corrosion Cracking of Alloy C-22 and Ti Gr-12 using Double-Cantilever-Beam Technique," *Micron*, Vol. 30(6), 1999, pp. 649-654.

75. A. K. Roy, D. C. Freeman and M. K. Spragge, "Stress Corrosion Cracking Evaluation of Candidate Container Alloys by Double Cantilever Beam Method," *Corrosion 2000*, Orlando, Florida, 2000, Paper No. 00189.

76. ASTM Designation E 399-99, "Standard Test Method for Linear-Elastic Plane-Strain Fracture Toughness K_{IC} of Metallic Materials," *American Society for Testing and Materials (ASTM) International*, West Conshohocken, PA, 2004.

77. G. F. V. Voort and E. P. Manilova, "Metallographic Techniques for Superalloys," *Microsc Microanal, Microscopic Society of America*, Vol. 10(2), 2004.

78. ASTM Designation E 112-96, "Standard Test Methods for Determining Average Grain Size," *American Society for Testing and Materials (ASTM) International*, West Conshohocken, PA, 2004.

79. L. Ma, "Comparison of Different Sample Preparation Techniques in TEM Observation of Microstructure of Inconel Alloy 783 Subjected to Prolonged Isothermal Exposure," *Micron*, Vol. 35(4), 2004, pp. 273-279.

80. P. E. Fischione, "Materials Specimen Preparation for Transmission Electron Microscopy," *E. A. Fischione Instruments, Inc. Export*, PA, USA.

81. ASM Handbook, "Metallography and Microstructures," Publisher: *ASM International*, Vol. 9, Materials Park, OH, 2004.

82. K. Yabusaki and H. Sasaki, "Specimen Preparation Technique for a Microstructure Analysis using the Focused Ion Beam Process," *Furukawa Review*, No. 22, 2002.

83. M. Meier, "Measuring Grain Size," Department of Chemical Engineering and Materials Science, *University of California, Davis*, 2004.

84. J. J. Friel, "Practical Guide to Image Analysis," Publisher: *ASM International*, Materials Park, OH, 2000.

85. A. K. Roy and V. Marthandam "Mechanisom of Yield Strength Anomaly of Alloy 617,"Material Science and Engineering A *Volume 517, Issues 1-2*, *20 August 2009*, *Pages 276-280.*

86. A. K. Roy, J. Pal and C. K. Mukhopadhyay, "Dynamic Strain Ageing of an Austenitic Superalloy – Temperature and Strain Rate Effects," *Materials Science and Engineering A*, Vol. 474(1-2), 2008, pp. 363-370.

87. A. K. Roy, M. H. Hasan and J. Pal, "Creep Deformation of Alloys 617 and 276 at 750-950 °C," *Materials Science and Engineering A*, Vol. 520(1-2), 2009, pp. 184-188.

88. A. R. Ibañez, A. Saxena and J. D. Kang, "Creep Behavior of a Directionally Solidified Nickel Based Superalloy," *Strength, Fracture and Complexity*, Vol. 4(2), 2006, pp. 75-81.

89. K. Krompholz, E. D. Grosser and K. Ewert "Determination of J- Integral R-Curves for Hastelloy X and Inconel 617 up to 1223 K using the Potential Drop Technique" Verlag Chemie GmbH, D-6940 Weinheim, 1982.

90. "http://www.twi.co.uk/content/jk76.html," CTOD Testing, *TWI (World Centre for Materials Joining Technology)*, Working Link, September 30, 2009.

91. Metals Handbook, 1987: pp. 396 and 453.

92. P. Georgsson, "The Determination of Uncertainties in Fatigue Crack Growth Measurement," Manual of Codes of Practice for the Determination of Uncertainties in Mechanical Tests on Metallic Materials, Standards Measurement & Testing Programme, Issue 1, 2000.

93. BIPM, IEC, IFCC, ISO, IUPAC, OIML, "Guide to the Expression of Uncertainty in Measurement," International Organization for Standardization, Geneva, Switzerland, 1st Edition, 1993.

VITA

Graduate College
University of Nevada, Las Vegas

Muhammad Hasibul Hasan

Degrees:

Bachelor of Science in Mechanical Engineering, 2000
Bangladesh University of Engineering and Technology (BUET)
Dhaka, Bangladesh.

Master of Science in Mechanical Engineering, 2002
Wayne State University
Detroit, Michigan.

Special Honors and Awards:

- Phi Kappa Phi, Fall 2007.
- Golden Key Honor Society, Spring 2007.

Publications:

Journal Articles:

- A. K. Roy, Muhammad H. Hasan and J. Pal, "Creep deformation of alloys 617 and 276 at 750-950 °C," Materials Science and Engineering A, Vol. 520(1-2), 2009, pp. 184-188.
- A. K. Roy, J. Pal and Muhammad H. Hasan, "Temperature and load ratio effects on crack-growth behavior of austenitic superalloys," Journal of Engineering Materials and Technology, Vol. 132(1), January 2010.

Selected Conference Presentations:

- Muhammad H. Hasan, J. Pal and A. K. Roy "Time and temperature-dependent deformation of alloy 617," TMS 2009, San Francisco, CA, February 2009.
- Muhammad H. Hasan, J. Pal and A. K. Roy "The Effects of Cyclic Loading, Temperature and Load Ratio on Plastic Deformation of Alloy 617" TMS 2009, San Francisco, CA, February 2009.
- Muhammad H. Hasan, J. Pal and A. K. Roy "Environmental Assist Degradation of Alloy 617 using Wedge Loaded Double-Cantilever-Beam Technique" MS&T 2009, Pittsburgh, PA, October 26th 2009.
- J. Pal, Muhammad H. Hasan and A. K. Roy, "Crack growth behavior of alloy 276 as functions of temperature and load ratio," TMS 2009, San Francisco, CA, February 2009.
- Sudin Chatterjee, A. K. Roy and Muhammad H. Hasan "An investigation into the high temperature creep properties of Alloy 230 for Very High Temperature Heat Exchanger Applications", TMS annual meeting and conference, Seattle, February 14-17, 2010 (accepted)

Dissertation Title: “Effects of mechanical and metallurgical variables on creep, fracture toughness and crack growth behavior of Alloy 617”

Dissertation Examination Committee:

Chairperson, Brendan O’Toole, Ph.D.
Co-chairperson, Ajit K. Roy, Ph.D.
Committee Member, WooSoon Yim, Ph.D.
Committee Member, Anthony E. Hechanova, Ph.D.
Committee Member, Daniel Cook, Ph. D.
Graduate Faculty Representative, Edward S. Neumann, Ph.D.